Philipps Universität Marburg

Organic-Inorganic Semiconductor Hybrid Systems: Structure, Morphology, and Electronic Properties

DISSERTATION

zur Erlangung des Doktorgrades
der Naturwissenschaften (Dr. rer. nat.)

dem
Fachbereich Physik
der Philipps-Universität Marburg

vorgelegt von

M.Sc. Mira El Helou

aus Tripoli, Libanon

Marburg(Lahn)
2012

Erstgutachter: Prof. Dr. Gregor Witte
Zweitgutachter: Prof. Dr. Wolfram Heimbrodt
Einreichdatum: 20.07.2012
Als Dissertation angenommen: 15.08.2012
Tag der mündlichen Prüfung: 22.08.2012
Hochschulkennziffer: 1180

Abstract

This dissertation addresses the preparation and characterization of hybrid semiconducting systems combining organic with inorganic materials. Characterization methods used included to determine the structure, morphology, and thermal stability comprised X-ray diffraction (XRD), atomic force microscopy (AFM), thermal desorption spectroscopy (TDS), and X-ray photoelectron spectroscopy (XPS). One organic-inorganic semiconducting system was pentacene ($C_{22}H_{14}$) and zinc oxide. This interface was investigated in detail for pentacene on an oxygen-terminated zinc oxide surface, i.e. ZnO$(000\overline{1})$. An extended study on the promising p-n junction was carried out for pentacene on ZnO with different orientations which exhibit different chemical and structural characteristics: ZnO$(000\overline{1})$, ZnO(0001), and ZnO$(10\overline{1}0)$. Moreover, the organic crystal structure of pentacene was selectively tuned by carefully choosing the substrate temperature. This defined interface with a physisorbed pentacene layer on ZnO was characterized by optical absorption which depends on the temperature of the measured system, the pentacene film thickness, and the molecular orientation and packing. The high quality of the pentacene films allowed in one case to characterize the Davydov splitting by linear polarized light focused on a single crystallite. Another subject in the field of organic-inorganic hybrid materials comprised conjugated dithiols used as self-assembled monolayers (SAMs) for immobilizing semiconducting CdS nanoparticles (NPs) on Au substrates. It was demonstrated that an appropriate selection and preparation of the conjugated SAMs is crucial for building up a light-addressable potentiometric sensor with a sufficient efficiency. An optimized electron transfer was achieved with SAMs of long range ordering, high stability, and adequate conductivity. This was examined for different linkers and was best for stilbenedithiol immobilized in solution at higher temperatures. Due to its high current yield and long term stability, the stilbenedithiol-based photosensor was used for peroxide detection incorporating modified CdS NPs with FePt. During this research, current sensing atomic force microscopy (CSAFM) was used to study the electronic behavior of a ZnO crystal. Optimized parameters for reproducible local current-voltage characteristics were determined using a high quality ZnO$(10\overline{1}0)$ surface as a specimen. It was shown that the desired reproducibility was achieved through the appropriate selection of the parameters such as potential range, sweep delay, and especially duration time of the individual $I - V$ curves. The role of the force load and temperature on electrical conduction was demonstrated for this semiconducting mixed-terminated ZnO surface.

Zusammenfassung

In dieser Arbeit stehen die Herstellung und Charakterisierung von Hybridsystemen im Vordergrund, die auf organisch-anorganischen Materialien basieren. Zur Aufklärung der Struktur, Morphologie und thermischen Stabilität der organischen Schichten wurden Methoden aus der Oberflächenphysik eingesetzt, wie Röntgenbeugung (XRD), Rasterkraftmikroskopie (AFM), thermische Desorptionsspektroskopie (TDS) und Röntgen-Photoelektronenspektroskopie (XPS). Als organisch-anorganische Heterostruktur wurde das System Pentacen-Zinkoxid untersucht, wobei das Pentacen ($C_{22}H_{14}$) auf dem sauerstoffterminierten Zinkoxid ZnO$(000\bar{1})$ ausführlich charakterisiert wurde. Eine erweiterte Studie von Pentacen auf ZnO verschiedener Terminierung wie ZnO$(000\bar{1})$, ZnO(0001) und ZnO$(10\bar{1}0)$ wurde durchgeführt. Diese Terminierung beschreibt den Einfluss der chemischen und strukturellen Aspekte des Substrats auf das Wachstum und die Eigenschaften der Pentacenschichten. Außerdem wurde die selektive Herstellung von einer bestimmten Kristallstruktur von Pentacen durch das Einstellen bestimmter Substrattemperaturen erzielt. Sowohl Pentacenschichten auf verschiedenen ZnO-Oberflächen als auch die verschiedenen Kristallphasen wurden mit der optischen Absorptionsspektroskopie in Abhängigkeit von der Temperatur, der Filmdicke und der molekularen Orientierung bzw. dem Packungsmotiv untersucht. Die hohe Qualität und Kristallinität der Proben erlaubten bei einer Kristallphase die Charakterisierung der Davydov-Aufspaltung durch linear polarisiertes Licht, das auf einen Einzelkristallit fokussiert wurde. Ein weiteres System im Rahmen der organisch-anorganischen Hybridmaterialien stellte die Verankerung von anorganischen CdS Nanopartikeln (NP) auf einem Goldsubstrat mittels eines bifunktionalen Linkers, der zu der Klasse der selbst-assemblierenden Monolagen (SAMs) gehört, dar. Die sogenannte Immobilisierung der NP wurde mittels eines konjugierten Dithiols realisiert, das über ausreichende Leitfähigkeit zum Einsatz im lichtadressierbaren potentiometrischen Sensor verfügt. Diese wurde optimiert durch geeignete Präparation langreichweitig geordneter, stabiler SAMs. Verschiedene Dithiole wurden zum Einsatz gebracht, wobei die mit Stilbendithiol bei höherer Temperatur modifizierte Goldelektrode genügend Effizienz und stabile Photoströme mit CdS NP erzielte. Dieser stilbendithiolbasierte Photosensor wurde exemplarisch mit FePt modifizierten CdS NP zum Nachweis von Wasserstoffperoxid verwendet. Im Rahmen dieser Doktorarbeit wurde eine Rasterkraftmikroskopie-Variante zur Leitfähigkeitsmessung an Oberflächen (current sensing AFM, kurz: CSAFM) am Beispiel von der gemischt-terminierten ZnO$(10\bar{1}0)$ Oberfläche eingeführt. Durch die geeignete Wahl von Eingabeparametern wie z.B. Spannungsbereich, Verzögerungszeit und Laufzeit der individuellen $I-V$-Kurven wurde die Reproduzierbarkeit der lokalen Leitfähigkeitsmessung optimiert. Zusätzlich wurde der Einfluss der Auflagekraft der Spitze und der Substrattemperatur auf die Leitfähigkeit der gemischt-terminierten ZnO-Oberfläche erforscht.

Contents

Chapter 1

Introduction and Objectives

Hybrid systems based on organic material known as soft matter are gaining increasing interest in investigating new material properties. An attractive aspect for incorporating organic compounds is the low-temperature processing and their wide scope of applications. For example, organic materials are used in transistors as a work function modifier of electrodes [1], as organic semiconductors combined with inorganic semiconductors in hybrid diodes [2] or as linker between planar electrodes and nanoparticles in light-addressable sensors [3]. In fact, organic molecules are considered flexible components due to van der Waals intermolecular forces and offer a wide range of optoelectrical properties. Combining such organic semiconductors with transparent inorganic material of wide optical bandgap is promising for optoelectronic applications in OLEDs (organic light-emitting diodes) [2]. Such transparent inorganic substrates are for example n-type metal oxides (TiO_2, ZnO, ITO) which are commercially available in highly crystalline form. Earlier experimental and theoretical studies of ZnO are considered in this work and allow to understand chemical and structural surface properties on an atomic scale for an increasing number of cases [4]. The conjugated aromatic semiconductor pentacene is the popular among aromatic acenes because its films possess high structural quality with remarkable p-type charge carrier mobility. Pentacene films grown on SiO_2 have been studied extensively and a dependence of structural properties on growth parameters was shown [5]. Hybrid pentacene-zinc oxide systems have been investigated in p-n junction diode [2], for instance (s. Fig. 1.1d), where its device characteristics were shown to be higher than previously reported for other organic vertical diodes. Unfortunately, little is known about the intrinsic interaction at the interface since optical absorption of organic molecules is anisotropic and may be influenced by several factors. This aspect must be explored in order to achieve fundamental understanding of optoelectronic processes and to control them. Optical properties of pentacene (PEN) are the main focus of this study. The optical transitions in pentacene deposited on ZnO$(000\bar{1})$ are studied by varying the organic film thickness and investigating the impact of temperature and surface termination of the ZnO on such transitions.

Another field of interest in organic-inorganic heterostructures is the modification of metallic or inorganic nanoparticles (NPs) with self-assembled monolayers (SAMs) used

as surfactant for stabilizing and controlling their size leading to new functionality. An example is illustrated in Fig. 1.1a and the wide scope of applications of SAMs is demonstrated in the review of Love *et al.* [6] for the model system thiol-based SAMs. In general, semiconducting nanoparticles (NPs) stand out due to the physical background concealed behind such quantum dots (QDs), the so-called quantum confinement effect. The quantum confinement depends on the material class, chemical composition, size and shape which in turn leads to novel electronic properties unexplored for bulk characteristics. Semiconducting SAMs have been used as bifunctional linkers to exploit the quantum effect of NPs on the macroscale by immobilizing them on substrates or anchoring them to polymers. Assembling NPs to larger structures on the macroscale is of great interest to use their unique properties for a wide range of applications. Such structures aim, for instance, at achieving linear structures [7, 8] of NPs on the microscale to align on surfaces or arrange them in a two-dimensional way for building up devices such as photosensor [3] (Fig. 1.1b and 1.1c). The effect of linking semiconducting inorganic NPs such as CdS using conjugated SAMs is studied for optimizing a light-controlled sensor by providing high quality SAMs given by their electronic and structural characteristics.

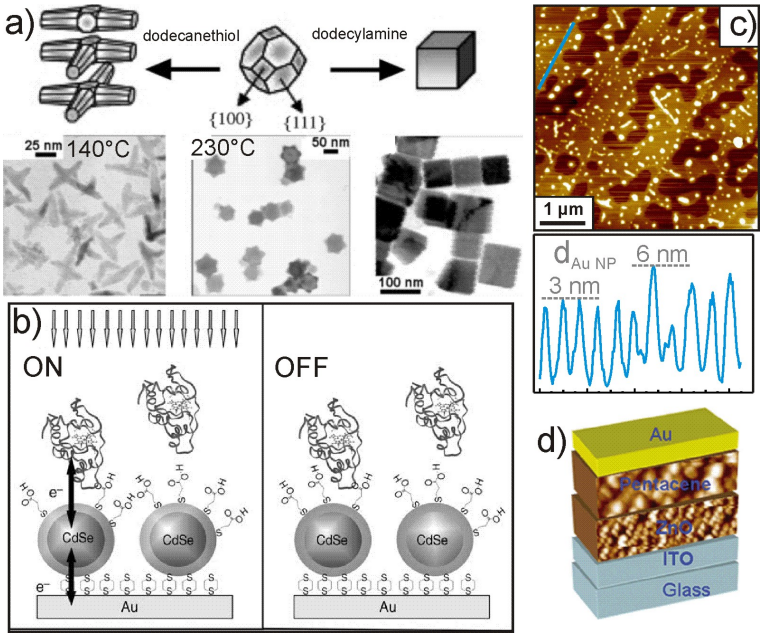

Figure 1.1: Role of organics in hybrid systems: a) growth modes of PbS nanocrystals in presence of different surfactants and the corresponding TEM images [6], b) photoswitchable electron transfer from an electrode via quantum dots toward the redox protein [3], c) AFM image of copolymerized Au NPs in PMMA deposited on HOPG to demonstrate the state of NP architecture in solution [8], and d) device structure of pentacene-zinc oxide vertical diode [2].

The anisotropic structure of a single organic molecule is crucial for its large structural, electronic, and optical variability which depend on the packing motif and the morphology at the organic-substrate interface. Such flexibility of an organic framework is traced

back to the van der Waals intermolecular forces which can be influenced by several factors. Depending on (i) substrate nature different polymorphs can be formed as vacuum-deposited pentacene films on gold [9] adopt the Siegrist phase [10] for example, while the Campbell configuration [11] and its primary growth stage as a substrate-induced packing motif (*thin-film* phase [12]) is formed on metal oxides (SiO_2, sapphire) [13, 5, 14]. Moreover, this molecule adopts different film structures if the substrate quality is reduced and becomes defective as demonstrated for pentacene grown on ultra smooth vs. rough HOPG [15]. The (ii) growth parameters on structure and morphology also affects film quality of long range order which is important for stable functionality through both organic semiconductors and self-assembled monolayers, where the substrate temperature comprises the main tuning factor and will be addressed in this thesis.

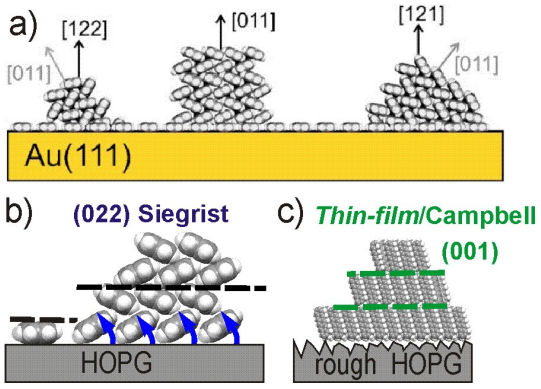

Figure 1.2: Pentacene growth on a) crystalline Au(111) [9] and b) lying on well-defined HOPG while c) upright orientation adopted on highly defective HOPG [15].

The molecular arrangement was analyzed by imaging molecular-scale objects by scanning probe microscopy (SPM). This method has also been a significant factor in the emergence of nanoscience and nanotechnology. Using atomic force microscopy (AFM), the morphology of a wide range of material classes and composite materials can be gently explored and considered minimally invasive as opposed to some electron microscopy methods. Hereby, film quality regarding grain size and high crystallinity which is reflected by molecularly flat terraces separated by monomolecular steps are explored revealing that the orientation (lying or standing molecules) is correlated to the optical and electronic characteristics. This indispensable method for unraveling structure and morphology has its limitation since the accuracy of height information lies within ± 0.5 Å. For upright standing molecular configurations, the height difference between the various crystal structures (ca. 1 Å) can be hardly distinguished. Therefore, AFM measurements were accompanied in this thesis by X-ray diffraction for a complete structural assessment. In addition, a technique of atomic force microscopy was used to study electrical properties made possible by metalization of the probe. This extended mode of AFM is denoted as conductive probe AFM or referred as current sensing AFM (CSAFM) to in this work. The conductivity and morphology are thus recorded simultaneously in

contact mode avoiding any damage or tip penetration through the sample. As a matter of fact, the attractive part of CSAFM is its ability to image sample morphology before, during, and even after local electrical measurement. The greatest advantage is the wide scope of substrates that can be investigated including insulators, semiconductors and metals. The tip-sample distance is decoupled from the current signal since it is controlled by the force load. The only restriction would be regarding the geometry of the sample which should be planar for mounting and scanning procedure since the z-range of an AFM scanner is approx. 1000 nm, as it is generally the case for most scanning probe microscopic (SPM) methods.

This study is divided into two parts. The first part comprises operating and testing parameters of current sensing AFM (CSAFM) and the other part is the cumulative one. CSAFM is described in the first chapter which mainly discusses the experimental setup and electrical characterization of ZnO($10\bar{1}0$). The cumulative work is an interfacial study of organic-inorganic hybrid systems. The first includes tuning pentacene aggregation of different thicknesses on well-prepared ZnO by varying surface orientation and substrate temperature, where the optical properties of this hybrid semiconductor is studied in a sufficiently wide temperature range (10-300 K). The second covers essentially the immobilization of semiconducting CdS quantum dots on Au substrate using SAMs for building up a photosensor resulting in an enhancement of its stability and yield by appropriate selection of nature and processing of the organic self-assembled layer.

These results are based on the following publications:

- J. Helzel, S. Jankowski, M. El Helou, G. Witte, and W. Heimbrodt, Temperature dependent optical properties of pentacene films on zinc oxide, *Applied Physics Letters* **99**, 211102 (2011).
- M. El Helou, E. Lietke, J. Helzel, W. Heimbrodt, and G. Witte, Structural and optical properties of pentacene films grown on differently oriented ZnO surfaces, *Journal of Physics: Condensed Matter* (2012), submitted.
- W. Khalid, M. El Helou, T. Murböck, Z. Yue, J.-M. Montenegro, K. Schubert, G. Göbel, F. Lisdat, G. Witte, and W. J. Parak, Immobilization of Quantum Dots *via* Conjugated Self-Assembled Monolayers and Their Application as a Light-Controlled Sensor for the Detection of Hydrogen Peroxide, *ACS NANO*, **5**, 9870 (2011).

Further publications generated during my doctoral research which are not part of the cumulative part:

- M. El Helou, O. Medenbach, and G. Witte, Rubrene Microcrystals: A Route to Investigate Surface Morphology and Bulk Anisotropies of Organic Semiconductors, *Crystal Growth and Design* **10**, 3496 (2010).
- K. Gries, M. El Helou, G. Witte, S. Agarwal, A. Greiner, Vinyl-functionalized gold nanoparticles as artificial monomers for the free radical copolymerization with methyl methacrylate, *Polymer* **53**, 1632 (2012).

Part I

Current Sensing Atomic Force Microscopy

Chapter 2

Current Sensing AFM on ZnO($10\bar{1}0$)

2.1 Preface

Current sensing atomic force microscopy (CSAFM) is gaining increasing interest in the field of nanoscience. It proved to be a powerful tool to study the electrical properties of individual nanostructures in form of wires, thin layers, or crystallites where the material class ranges from conductors to insulators [16, 17]. Common surface-sensitive experimental methods for characterizing electronic properties are mostly ultraviolet photoelectron spectroscopy (UPS) or scanning tunneling microscopy (STM) for average or local analysis, respectively. However, analyzing semiconducting or insulating materials with UPS or XPS poses a significant challenge and gives rise to limitations caused by the nonconducting nature which suffers disruptive charging effects. For instance, any attempt to image an organic semiconducting film thicker than 10 nm with STM, as the case for aromatic perylene films on copper, has failed [18] and can result in the damage of the organic layer as demonstrated in Fig. 2.1 for 100 nm thickness.

In principle, the current that flows after applying a voltage between the conducting tip or probe and an electrode is measured, where the first electrode, the probe, acts as a microcontact and the other electrode, a wire, is attached to the sample. Two configurations for attaching the wire can be realized which results in electrical properties for the bulk or the surface. The setup geometries will be commented in the following section. A current map is thus recorded at a given applied voltage. Locating the tip at a specific position enables to examine the flow of current locally in the nano regime by sweeping the tip or sample bias achieving $I - V$ characteristics. The setup can be operating in ambient or under controlled conditions without the necessity of UHV. With such setup, the tip electrode can be precisely positioned on the sample surface at the microscale in the first place and, secondly, the deflection of the cantilever can be used in order to control the contact pressure on the surface, i.e. controlling mechanical contact. The latter aspect possesses the advantage that current-voltage ($I - V$) relationship is decoupled from the sample position feedback mechanism for topographical imaging in

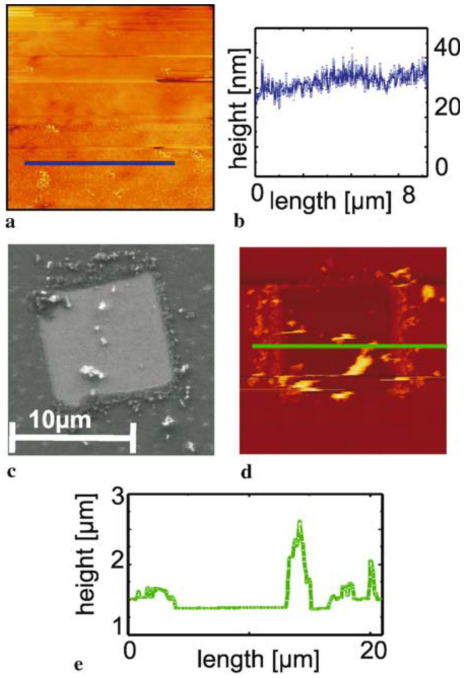

Figure 2.1: a) STM image ($10\,\mu$m $\times$ $10\,\mu$m, $V = -2$ V $I = 50$ pA) with b) a corresponding line scan and c) subsequently recorded SEM micrograph and d,e) AFM micrograph (tapping mode) of the same region. These data are published by Witte *et al.* in [18].

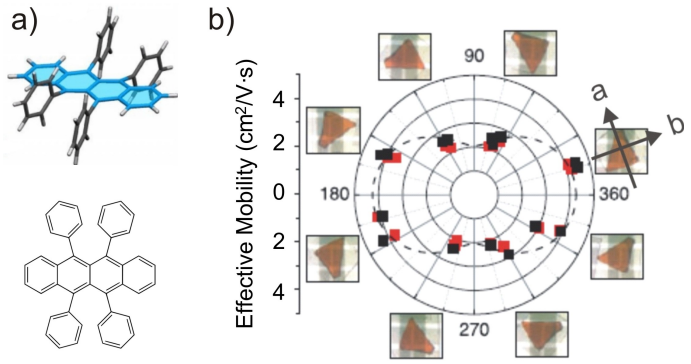

Figure 2.2: a) Molecular structure of rubrene. b) Polar plot of effective charge carrier mobility showing the anisotropic behavior along the $\vec{a}$ (90° and 270°) and $\vec{b}$ (180° and 360°) crystallographic direction of a rubrene orthorhombic crystal from [19], where the mobilities are shown to differ at least by a factor of two.

contrast to STM. Thus, the nondestructive nature of the mode opens new pathways for electrical studies on soft and fragile surface structures in all fields of nanoscience.

Semiconducting soft matter composed of highly asymmetric molecules exhibit gen-

erally anisotropic electrical properties. Such phenomena were for instance demonstrated for the higher membered acene, rubrene $C_{42}H_{28}$ (cf. Fig. 2.2a), where the charge carrier mobility was plotted for a single crystal within the (001) plane [19] and a discrete anisotropic behavior was recorded as depicted in Fig. 2.2b. Besides charge carrier anisotropy, charge transport phenomena are shown to be influenced by molecular configuration, packing motif, crystal orientation, degree of crystallinity, and purity of such material. The first step toward understanding charge transport in organic semiconductors is to investigate their intrinsic properties offered by crystalline material. Nevertheless, extrinsic characteristics play a major role as well, such as contact resistance and measuring conditions (atmospheric gas, temperature, humidity).

In the field of organic materials, CSAFM was applied for example to the following classes: sexithiophene films [20] and carbon nanotubes [16]. In both cases, the electrode wire on the surface has been processed by lithographic methods, whereas a spring-loaded electrode attached manually to the sample was involved in this work. This situation generates a restriction regarding sample lateral size for electrode positioning and, moreover, thickness of the fragile organic component ranging few microns to the most causes a problem in pressing or fixing the wire. The primary goal was to study intrinsic charge transport using CSAFM on high quality rubrene single crystals provided by a hot-wall evaporation [21]. These crystals possess lateral dimensions of ca. 150 μm which was a challenging problem in manual clamping of the wire for surface transport properties. A vertical setup geometry was also not possible since these crystals were grown on SiO_2 and not on conducting surface. These two aspects impart the reason for an alternative sample, however, they could be overcome in case rubrene crystals were grown in the millimeter range and the fixing mechanism is reconstructed for a suitable (manual) positioning and clamping. In this study, CSAFM is used to examine the morphology and surface conductivity of a crystalline semiconducting system in form of single crystal, which should therefore possess dimensions ≥ 3 mm for mounting purposes on the one hand and should exhibit a minimal altering in air and under ambient conditions on the other. Organic semiconductor crystals of acenes, like rubrene or pentacene, were not grown at that time in the scale needed for implementation. Therefore, the class of inorganic semiconducting materials was chosen since they are commercially available, such as ZnO mixed-terminated surface denoted as ZnO($10\bar{1}0$). It is used in this work for a CSAFM study and offers sophisticated surface quality after crystal preparation following a recipe developed by our group [22]. ZnO($10\bar{1}0$) reveals no noticeable aging of the surface structure within 24h which, by contrast, was the case for the polar *c*-plane of ZnO crystals [22] within 2h, also known as the zinc-terminated (0001) and oxygen-terminated ($000\bar{1}$) surface. In fact, first CSAFM data were accomplished for (0001) and ($000\bar{1}$) polar planes of a ZnO crystal [23], i.e. the *c*-plane. A certain dependency on the maximum applied voltage and the presence of H_2O showed influence on the conduction of ZnO(0001) vs. ZnO($000\bar{1}$) in a further CSAFM study by Moore *et al.* [24]. This finding emphasizes the different chemical affinities of Zn- and O-terminated ZnO crystal surfaces resulting in different $I-V$ characteristics recorded in air at RT. In this chapter, the implementation of CSAFM and examination of the ZnO($10\bar{1}0$) are introduced and

discussed against multiple parameters and measurement conditions.

2.2 Experimental Setup and Preparing for Measurements

CSAFM is an extended application mode of the contact mode provided by our Agilent SPM5500 model. A conducting AFM tip is mounted to the scanner which contains a blue-coded preamp for 1 nA/V sensitivity allowing current detection up to 10 nA. The setup for current sensing is illustrated schematically in Fig. 2.3b.

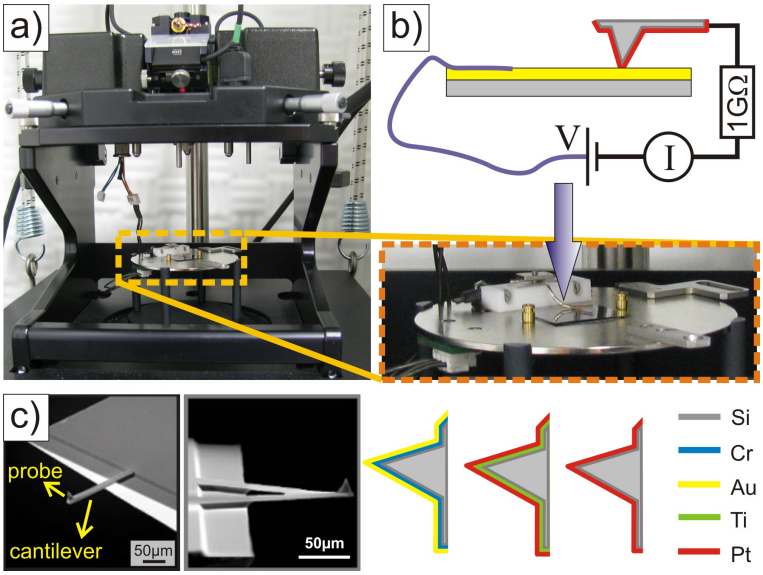

Figure 2.3: a) AFM stage including the scanner (upper part) and the sample plate. The latter is again zoomed-in with a red frame. b) Schematic illustration of the CSAFM setup where the current I is measured after applying a voltage V between the conducting probe or tip and the electrode attached to the sample surface. c) SEM image of rectangular and triangular cantilever of NSC18/Ti-Pt and CSC11/Pt, respectively, from μmash [25] used in this work for CSAFM measurements and the illustration of coated tips.

A voltage or bias is applied between the tip and the sample which is connected to a wire electrode and is defined in this work as V corresponding to sample bias. The tip is then approached to the surface till a defined repulsive force is reached (the setpoint). This setpoint is given by the deflection of the cantilever (Δx) detected as the displacement of the laser spot position on the photodiode in volts. According to this relation, the precise deflection Δx can be extracted from the "force-distance" curve for approach and withdraw tip motion using force spectroscopy. The slope in the linear repulsive regime of the approach curve determines the cantilever sensitivity S in nm/V which at a given setpoint conveys the deflection Δx in nm. Therefore, $\Delta x = sensitivity \times setpoint$, whereas the contact force can be calculated using Hooke's law ($F = k \cdot \Delta x$). The force constant is given by the manufacturer as a minimum (k_{min}) and maximum (k_{min}) value.

Therefore, the average load can be determined from an average force constant $\overline{k}$. Since the deflection Δx can be determined more accurately, the force load is thus expressed in terms of cantilever deflection in volts or nanometers. An example is illustrated in Fig. 2.4. When probing electrical properties as a function of force load as described later in the results, the deflection Δx of the cantilever is given instead of force units.

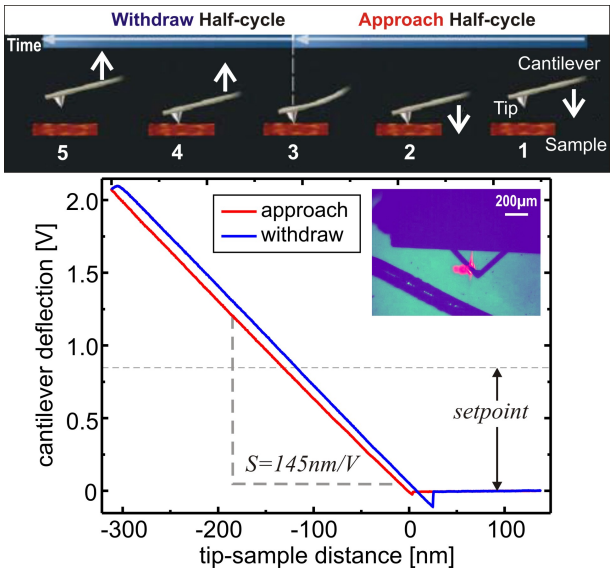

Figure 2.4: Schematic overview (*upper panel*) of force spectroscopy. Force distance curve (*lower panel*) acquired using the triangular conducting cantilever at a given position on the ZnO($10\overline{1}0$) surface shown in the image as inset. A gold wire of 0.2 mm cross section was used in this case. The cantilever deflection recorded from the laser spot position on the photodetector is plotted against the tip-sample distance. The slope of the approach curve determines the sensitivity S.

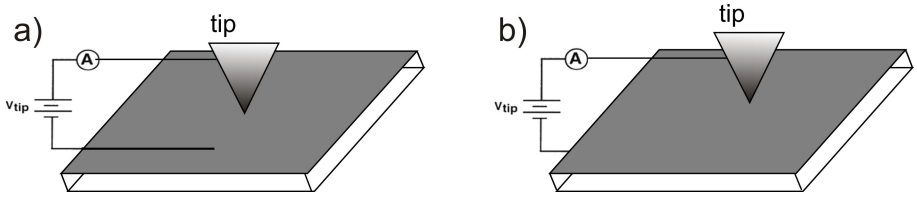

Figure 2.5: Measurement configurations for a) horizontal (surface properties) and b) vertical conductance (bulk properties) within CSAFM.

Commercial rectangular Si cantilevers with a Ti-Pt coated tip (10 nm Pt on 20 nm Ti adhesion layer) resulting in a 40 nm radius tip were used for the temperature dependence experiments and the rest was executed with a triangular Si cantilever coated with 15 nm Pt (25 nm tip radius). These cantilevers were acquired from μmash and denoted as NSC18/Ti-Pt with a spring constant ranging between $k_{min} = 2.0\,\mathrm{N/m}$ and $k_{max} =$

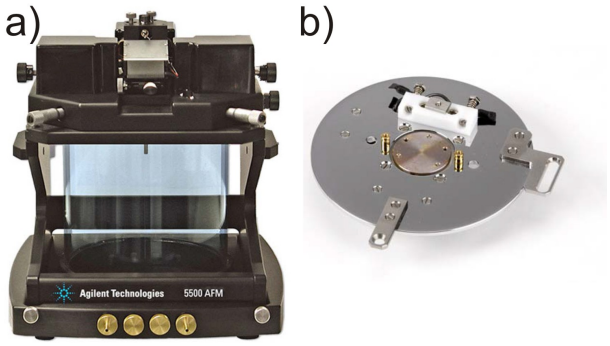

Figure 2.6: a)Environmental chamber mounted on microscope. b) Hot sample plate provides temperature range from ambient to 250 °C. Pictures originate from [26]

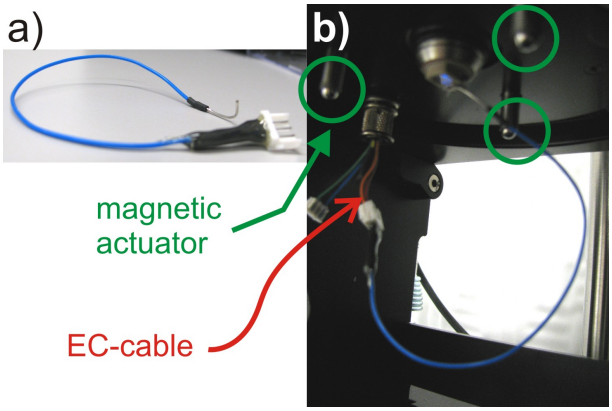

Figure 2.7: a) A test resistance of 1 GΩ. b) CSAFM setup for electronic check of the control experiment using the test resistance shown in a) without mounting a sample plate and thus keeping the circuit open (ungrounded).

5.5 N/m, where an average spring constant $\overline{k}$ is given as 3.5 N/m for the rectangular shaped and as CSC11/Ti with $k_{min} = 0.1$ N/m and $k_{max} = 0.9$ N/m, where $\overline{k} = 0.35$ N/m for the triangular ones [25]. Note that Pt is considered as a better wear-resistant coating than Au. This setup provided by Agilent allows two geometries for $I-V$ measurements (s. Fig. 2.5): (a) horizontal (surface) charge transport for electrode connected onto the sample surface or (b) vertical (bulk) geometry for connecting beneath the sample are inquired. For the essential part in this chapter, surface transport phenomena are studied and are of main interest, thus following horizontal (axial) geometry illustrated in Fig. 2.5a. Temperature-dependent $I-V$ characteristics have been executed in argon atmosphere using the environmental chamber mounted on microscope, while the sample is placed on the sample holder with an integrated temperature-programmed heating unit as depicted in Fig. 2.6a and 2.6b, respectively.

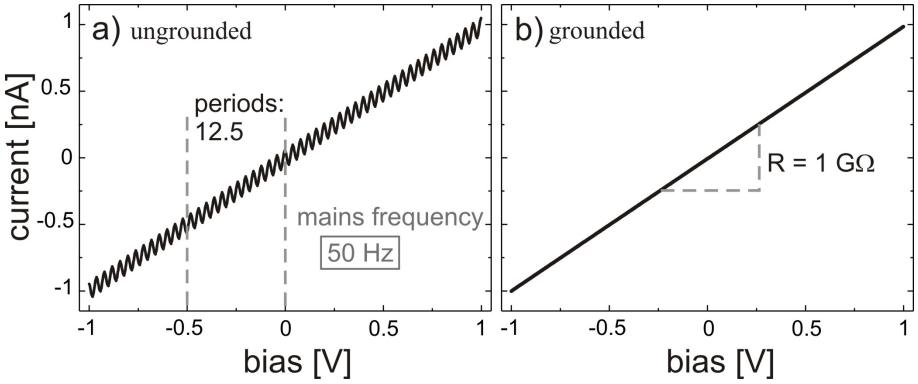

Figure 2.8: $I-V$ spectra recorded for the 1 GΩ test resistance in the voltage range [-1V,+1V] in **1 s**. a) Vibrations expected when CSAFM system not grounded corresponding to mains frequency of 50 Hz. b) Grounded system with absence of any noise.

Since contact mode scanning or successive $I-V$ measurements may cause a degradation of the metallic coating material or loose contact may occur in the circuit, control measurement for the system has been executed under ambient conditions in two steps: (i) the first by connecting a test resistance of 1 GΩ (s. Fig. 2.7a) between the cantilever clip and the sample plate and (ii) the second by executing $I-V$ measurements with a metal coated tip on an noble metallic sample such as Au/mica. In both cases, an Ohmic trend must be observed giving in the first case the expected slope of 1 GΩ (s. Fig. 2.7b). In order to avoid mains frequency (50 Hz), one should make sure that the system is grounded. For example, going about point (i) requires no sample plate and while keeping the circuit open as shown in Fig. 2.7b, the $I-V$ spectrum reveals noise in the range of the mains frequency which leads to the result in Fig. 2.8a compared to a grounded system of the same setup with absence of any noise in Fig. 2.8b. Therefore, a sample plate should be mounted to the magnetic actuators and, furthermore, if the sample plate features a cooling or heating body, the cables must be plugged in the temperature controller to ensure grounding.

Prior to further investigations, characteristic curves of a freshly prepared Au/mica substrate flame-annealed in air by a propane gas flame was used for controlling the conductivity of the AFM tip under ambient conditions. In case the tip is fully functional, an Ohmic curve is obtained otherwise no current can be detected as shown in Fig. 2.9.

The specimen used in this study are single side polished ZnO($10\bar{1}0$) single crystals grown hydrothermally from CrysTec GmbH of size 10 mm × 10 mm and of 1 mm thickness. The crystals were prepared at first by argon-ion sputtering at 800 eV in a vacuum apparatus for 3h and subsequent heating in air at 1200 K for 1h using a furnace (Heraeus). This preparation step gives rise to highly ordered surface exhibiting sharp (1 × 1) low energy electron diffraction (LEED) patterns and monoatomic steps as well as atomically flat terraces extending over a few hundreds of nanometers as published in [22]. Such high quality freshly-prepared ZnO($10\bar{1}0$) surface was mounted onto the Agilent

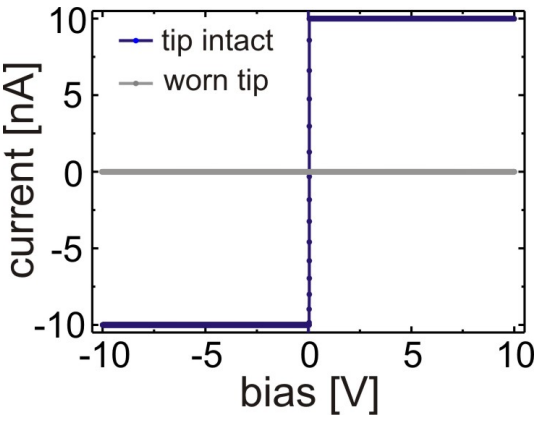

Figure 2.9: Testing the tip for conductance by $I-V$ spectroscopy on Au/mica under ambient conditions. The curves are measured in 4.8 s with 60000 data points by ramping the sample bias form -10 V to +10 V.

sample plate and set to electrical contact by a silver-coated copper wire, if not otherwise mentioned, for current-voltage studies by means of CSAFM. The $I-V$ curves presented are the result of averaging data points (DP) of ten successive measurements delayed by 2 s (named "delay") at the same point, where each individual curve was recorded by sweeping the sample bias in the range -10 V to +10 V in a duration of 5 s and a resolution of 2500 DP if not otherwise mentioned. For this sweeping, the **current-voltage** curves are coded in blue and called forward bias, whereas sweeping the bias from +10 V to -10 V, i.e. in the opposite direction, is denoted as reverse bias and is displayed as red colored spectrum. In order to clarify the location of the band edges in case of rectifying behavior, the logarithm of the conductance is additionally plotted against the sample bias, i.e. lg $\left(\frac{dI}{dV}\right)$ versus V. The color coding for the **conductance** of the forward and reverse bias are depicted in orange and green, respectively. The reverse curves are labeled with the extension "RE".The dependency of $I-V$ spectra on ZnO(10$\bar{1}$0) surface temperature has been executed under argon atmosphere within the environmental chamber. After mounting and contacting the sample, the chamber was backfilled with argon after purging with argon gas for 10 min. The sample plate was then programmed to reach the temperatures 34.5 °C, 60 °C, and 100 °C and the system was subsequently allowed in 2.5h to reach thermal equilibrium with the tip located in the immediate vicinity of the surface (10 μm vertical distance) before begin current-voltage data acquisition. The temperature-dependent CSAFM measurements were executed on a freshly prepared ZnO crystal within 24h, i.e. the time where minimum degradation takes place.

2.3 Results and Discussion

In this section, local $I-V$ spectra on ZnO(10$\bar{1}$0) are investigated in argon atmosphere in order to learn about the functionality and reliability of CSAFM. Ten consecutive

individual spectra are averaged for a defined load ($\Delta x = 95\,\text{nm}$, the setpoint, $F \approx 30\,\text{nN}$) and voltage ramp (duration 2 s for [-10 V,+10 V]) on the surface at room temperature (RT) to give an $I - V$ curve for the forward bias displayed in Fig. 2.10a (i). For negative sample bias, conductance occurs already within the detection range between 0 and -10 V. After withdrawing the tip 20 μm from the surface and approaching at an equivalent setpoint, the next averaged curve in Fig. 2.10a (ii) is maintained and the same applies to the third run in Fig. 2.10a (iii). This indicates a stable and reproducible measurement for the parameters mentioned above. In Fig. 2.10b, another example is presented when data is not reproducible at the same point. The duration was set to 1 s at a load of $\Delta x = 380\,\text{nm}$ ($F \approx 130\,\text{nN}$). The averaged curve recorded within two consecutive runs reveals no reproducibility (compare Fig. 2.10b (i) and 2.10b (ii)), whereas for slower voltage ramp, for instance 7.5 s, the curves reveal a stable manner. The reproducibility is thus confirmed in case the parameters such as duration ($\geq$2 s), start and end values of sample bias, and delay between individual spectra are retained. Note that, the conduction behavior changes if the duration of the voltage ramp is varied as can be taken from comparing Fig. 2.10b (ii) to Fig. 2.10b (iii) corresponding to durations of 1 s and 7.5 s, respectively. Current seems to flow at lower sample bias when the duration is larger, i.e. when applying slower rates. A previous work by Moore *et al.* [24] has reported a change in $I - V$ behavior as a function of maximum applied voltage for the polar ZnO surfaces, where information about duration time or ramping rate were unmentioned and remain unclear. After all, it is a fact that a correlation between the ramping rate and $I-V$ spectra does exist and is corroborated for the case of ZnO($10\bar{1}0$) as well. Note that in Fig. 2.10a (ii), a jump in the current is detected at about +8.5 V which is due to slew rate. This issue is observed as well in the upcoming data at other voltages and should not have any further impact on the results.

The following data of CSAFM on ZnO($10\bar{1}0$) was acquired using a rectangular-formed cantilever of larger spring constant (ten times stiffer than the triangular used before). At room temperature, measurements with a tip contact of $\Delta x = 85\,\text{nm}$ ($F \approx 300\,\text{nN}$)(s. Fig. 2.11a-*upper panel*) reveal in the forward bias (in blue) no current leakage up to sample bias +6 V, while conduction appears across the whole negative sample bias. The asymmetry in the positive (A) and negative (B) voltage range may be explained by the energy level alignment of the system shown in Fig. 2.11b. At the positive sample bias (A), electrons flow from tip to sample which must overcome a high barrier (˜[2]eV) than the reverse direction (B). In contrast, this rectifying behavior when ramping in the forward direction is not consistent when the bias ramp is reversed (curve in red). The reverse curve follows an Ohmic behavior instead since no gap in conductance (green curve) was observed. For both ramping directions, i.e. forward and reverse curves, a distinct difference in conduction mechanism is monitored in the negative voltage regime (B), where a more abrupt breakdown is observed for forward vs. reverse curves. Note that the designation "Ohmic" is referred to $I - V$ characteristics having no current gap as just described for the forward bias data. In fact, possible conduction mechanisms [27, 28] have been reported in literature, like Fowler-Nordheim tunneling or trap-assisted tunneling, which are not further considered in this work.

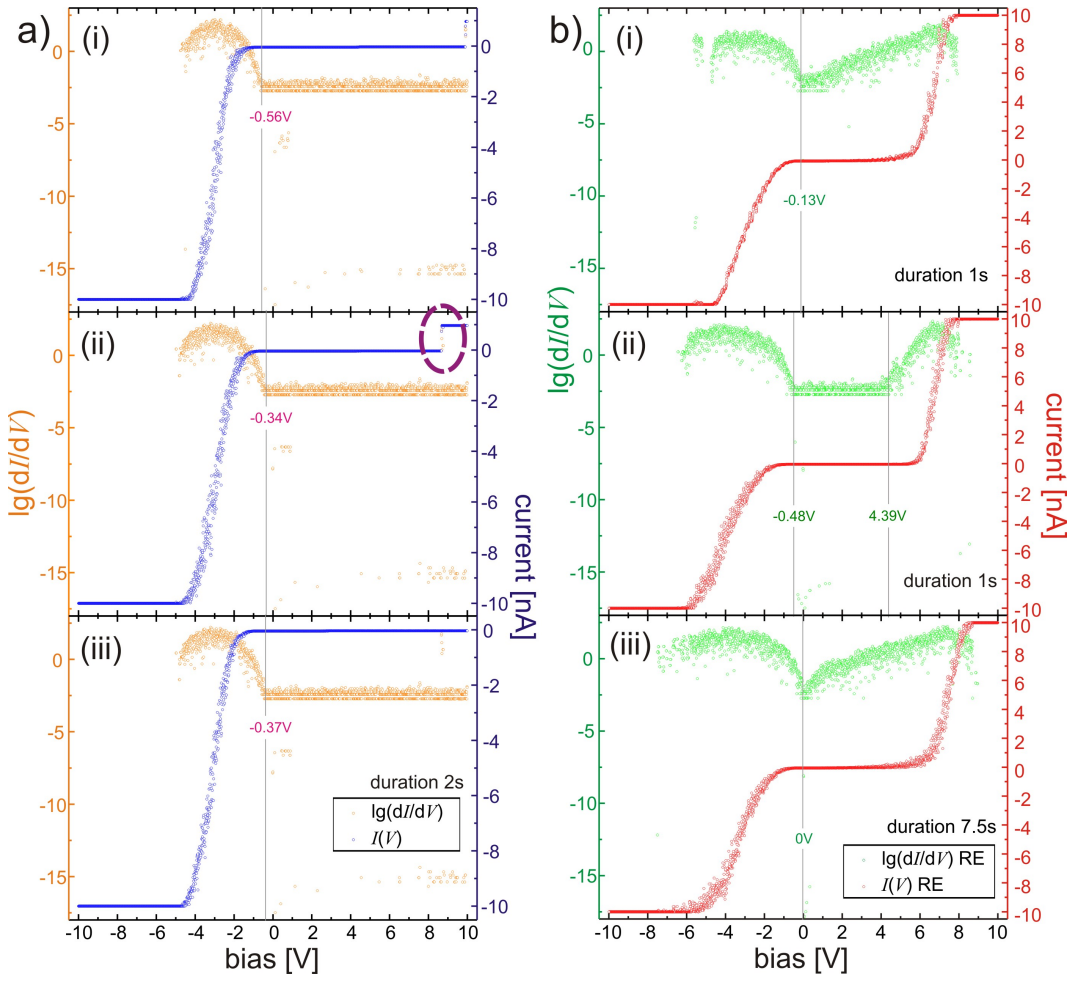

Figure 2.10: $I-V$ behavior on ZnO(10$\bar{1}$0) at RT measured by the triangular, Pt-coated tip of sensitivity $S = 95\,\mathrm{nm/V}$ for testing reproducibility. a) Three cycles (i-iii) of forward bias ramping in **2 s**. Each cycle is recorded by consecutively withdrawing the cantilever 20 μm and approaching with a setpoint (cantilever deflection) $\Delta x = 95\,\mathrm{nm}$. The circled area in (ii) is a dropout due to slew rate. b) Reverse spectra collected in **1 s** (i,ii) at $\Delta x = 380\,\mathrm{nm}$ being unreproducible and exemplifying that electric properties vary with duration times as compared to data recorded in 7.5 s (iii).

Enhancing the tip-sample contact by increasing the cantilever load to $4F$ resulted in the curves shown in Fig. 2.11a-*lower panels* acquired at RT (20.9 °C). An improved physical contact of the tip with sample surface lifted the rectifying behavior and the current flow at negative bias remains unchanged for both loads. On the other hand, no influence exists on the Ohmic behavior in the reverse bias ramp at higher tip loads as shown in *right panels* of Fig. 2.11a. Therefore, increasing tip load repeals the rectifying behavior even at RT, whereas the part with abrupt breakdown remains unaffected.

$I-V$ characteristics at elevated temperature behave differently and are summarized

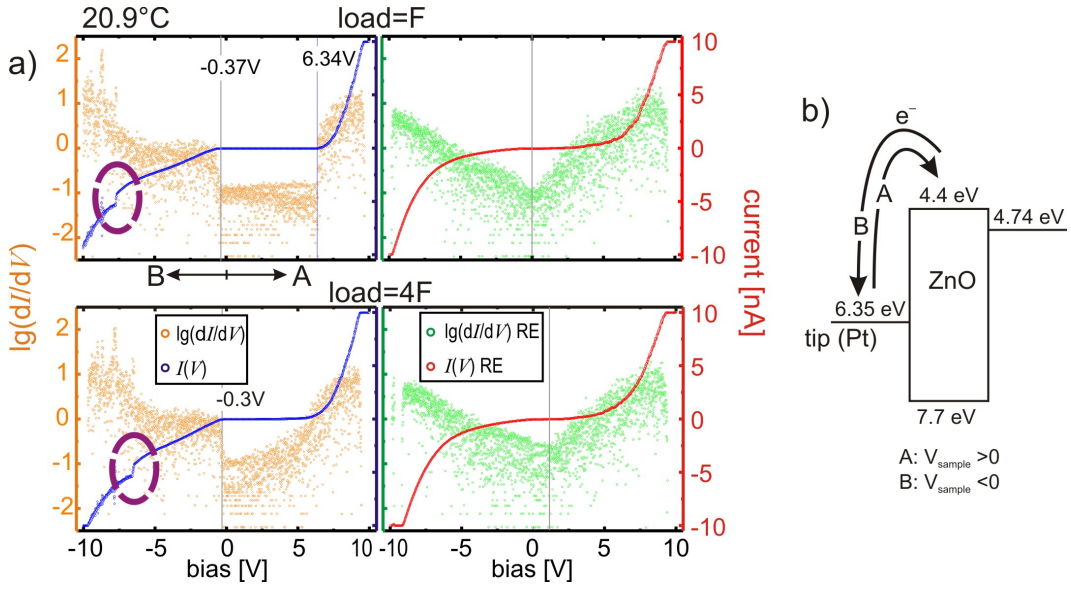

Figure 2.11: a) At room temperature 20.9 °C, the current-voltage characteristics of forward potential ramp (*left panels*) with a soft contact (load=F) on ZnO($10\bar{1}0$) reveal greater band gap than tip contact with high pressure (load=4F). In this case, the cantilever used possess a rectangular form coated with Ti-Pt. The load F corresponds to a cantilever deflection of $\Delta x = 85\,\text{nm}$. A and B resemble the positive and negative bias regime, respectively. The reverse curves (*right panels*) run in a different manner but show no significant dependence on load. b) Schematic energy band level alignment of the system with respect to vacuum level. The work functions were taken from the reference [29] and the HOMO-LUMO of ZnO from [2].

in Fig. 2.12. Still, a common feature comprises the rectifying behavior which is repealed for reverse sample bias and conserved for forward runs at low force load (s. Fig. 2.12a) being consistent with findings at RT. The more abrupt breakdown in the positive bias range for forward vs. reverse curves is not noticed at elevated temperatures for instance at 60 °C (Fig. 2.12a) and 100 °C (cf. Fig. 2.12b). However, for room temperature results, the discrepancy in conduction in the B range of the forward vs. reverse curves is not observed when the measurements were carried out at higher temperatures. This may be attributed to the absence of a desorption layer like water at higher temperatures bearing in mind that higher loads at RT seem insufficient to eliminate this layer at the contact point. A soft ($\Delta x = 40\,\text{nm}, F \approx 150\,\text{nN}$) or stiff ($\Delta x = 320\,\text{nm}, F \approx 1200\,\text{nN}$) contact between the tip and sample exerts significant influence on the $I - V$ characteristics depicted in Fig. 2.12a and 2.12c, respectively. Forward ramp with a high tip load demonstrates an Ohmic behavior with continuous, substantially increased current leakage extending over both positive and negative bias, thus compensating the rectifying behavior at low contact force. A distinct feature at high load is the fluctuations of the current which is progressive for the forward curve (s. Fig. 2.12c), while it diminishes in case measurements were executed in the reverse voltage manner. The same forward curve monitored at 100 °C reveals interestingly an unexpected feature. At a high force

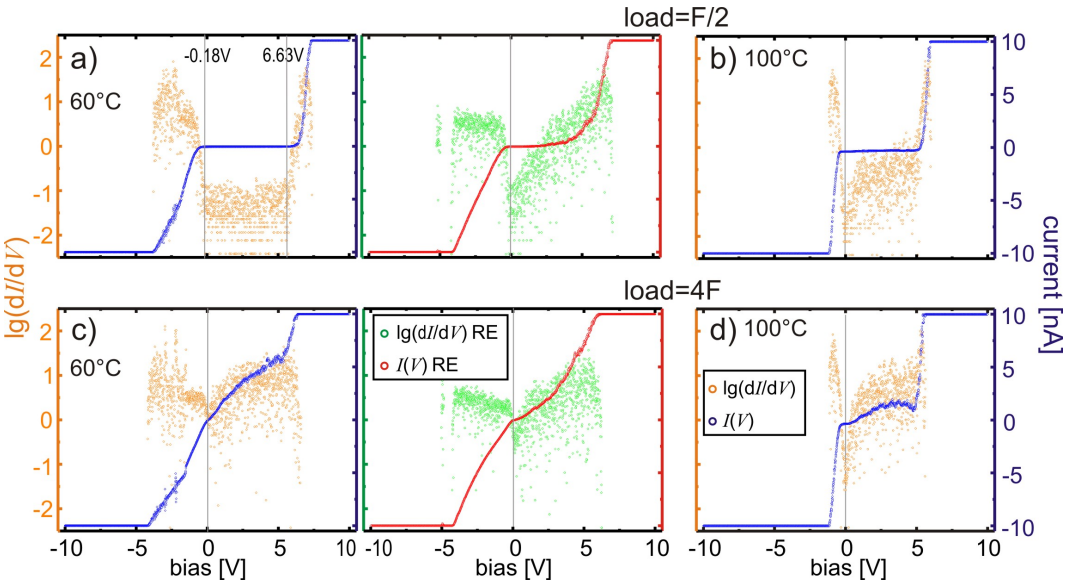

Figure 2.12: $I-V$ spectra on ZnO(10$\bar{1}$0) at (a,c) 60 °C for forward (blue) and reverse (red) potential ramp and (b,d) 100 °C for forward runs showing significant deviation when the tip contacts the surface with a load F/2 or 4F. The load F corresponds to a cantilever deflection of $\Delta x = 80$ nm.

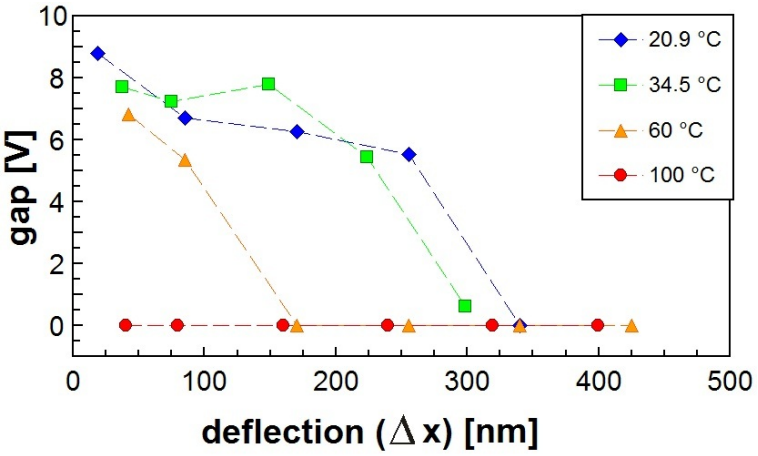

Figure 2.13: Summary of the temperature-dependent $I-V$ data on ZnO(10$\bar{1}$0) in argon atmosphere where the band gap is plotted as a function of load expressed as cantilever deflection Δx in nm for temperatures ranging from ambient to 100 °C.

load ($4F$), the conductance appears to be reduced compared to a force load of $F/2$ (compare Fig. 2.12b and 2.12d). The expected trend of higher conduction at 100 °C is not achieved which is most probably attributed to wearing of the Pt coating, since these measurements have been executed with the one and the same conducting tip. However,

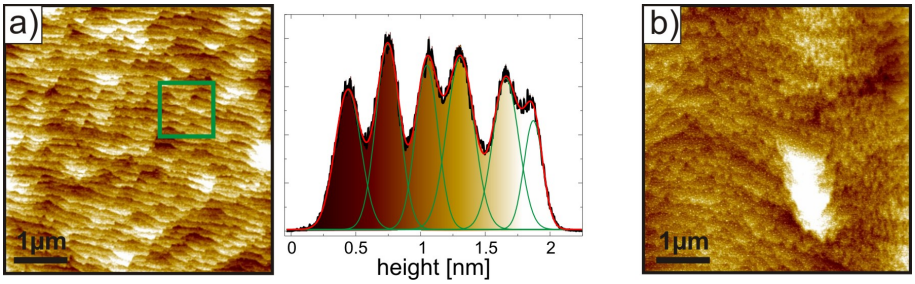

Figure 2.14: AFM images with 5 μm scan size of ZnO(10$\bar{1}$0) recorded in ambient a) directly after preparation and b) after 3 days. The histogram in a) reveals an average step height of (2.9±0.5) Å.

a remarkable aspect of conduction can be deduced. It proves to be temperature dependent and is best illustrated, for instance, in the B range of forward curves. It is striking that high current flow is observed at increasingly low bias voltages implying increased conduction as the substrate temperature rises being highest at 100 °C (s. Fig. 2.12b) compared to room temperature experiments. The increased conductivity or reduced resistivity of such semiconductor is expected to take place with increasing temperature and could be proven with CSAFM for the case of ZnO(10$\bar{1}$0).

Analysis of the data for band gap of ZnO(10$\bar{1}$0) as a function of load is summarized in the diagram shown in Fig. 2.13 for four different temperatures 20.9 °C, 34.5 °C, 60 °C, and 100 °C. Higher tip loads enhance the contact on the surface which implied a reduced contact resistance and therefore promote a better charge transport. The trend is consistent at different temperatures in case a gap is existent.

The surface degradation of ZnO has been observed in ambient in form of reconstructions for the O-terminated surface within 2h [22]. The stability of ZnO(10$\bar{1}$0) is noted in this work by imaging the surface directly after preparation and after 3 days using AFM in tapping mode. AFM micrographs are depicted in Fig. 2.14 and show atomically flat terraces separated by ca. 3 Å steps as recorded by a height histogram of an zoomed area in Fig. 2.14a. This quality is preserved after 24h in air. A degree of altering in form of adsorbates decorating the monoatomic steps is observed after exposing the crystal for 3 days to ambient (s. Fig. 2.14b).

2.4 Summary

During this experimental research, optimized parameters for a reproducible local current-voltage characteristics using high quality ZnO(10$\bar{1}$0) surface as a specimen have been explored. It was shown that the desired reproducibility is achieved through the appropriate selection of the parameters such as potential range, sweep delay (time between individual scanned curves), and especially duration time which were set to [-10 V,+10 V], 2 s, and 5 s, respectively. Such parameters have not been considered in literature so far except for the maximum applied voltage [24]. For this semiconducting surface, the role

of the load and temperature on electrical conduction is demonstrated. At a given load at RT, reproducible measurements reveal rectifying to Ohmic behavior depending on the duration time, on the one hand, and on direction of the bias ramp direction denoted as forward or reverse curves. The latter diminishes for negative voltages at high temperatures which could be attributed to the absence of water layer acting as an insulating layer at the tip-sample contact area. Moreover, increasing the load results in a change in electrical conductance due to reduced contact resistance, while a higher impact on $I-V$ spectra is observed at elevated temperatures which lead to higher current flow at a lower bias. The more abrupt breakdown in positive bias for the forward vs. reverse curves is a common feature among all experiments. In conclusion, CSAFM analysis can be utilized in temperature-dependent analysis of electrical conduction which would not constitute any difficulty for organic soft matter of higher conjugation (high sublimation enthalpy). The Ti-Pt coated tip is robust and stable for over 600 cycles at different loads and allows load dependent correlation of $I-V$ characteristics. However, applying CSAFM requires a minimum crystallite size of $\geq$3 mm and a stiff cantilever (k$\geq$0.35 N/m) hampers the analysis on fragile materials due to the disruptive force loads induced by the tip. For example, imaging topography and current simultaneously in contact mode using the rectangular cantilever of $\overline{k} = 3.5\,\mathrm{N/m}$ requires extremely low setpoint of about 0.02 V corresponding to cantilever deflection of 1.6 nm. At such a low deflection, instability or more likely lack of reproducibility of current-voltage curves must be taken into account.

Part II

Cumulative Part

Chapter 3

Pentacene-ZnO Semiconductor Hybrid System

3.1 Temperature-dependent optical absorption of pentacene as a function of thickness on ZnO$(000\bar{1})$

Title of publication:

"Temperature dependent optical properties of pentacene films on zinc oxide"

Published in:

J. Helzel, S. Jankowski, M. El Helou, G. Witte, and W. Heimbrodt, Applied Physics Letters **99**, 211102 (2011).

Summary:

In the case of pentacene films deposited on SiO_2, temperature-dependent excitonic transition has shown thickness dependence of pentacene films. The packing motif and molecular orientation of pentacene were reported to be crucial for optical absorption [30]. So far, two polymorphs in the bulk phase and one substrate-induced phase have been identified for pentacene which makes the thin film packing nontrivial. Previous studies showed that the molecular arrangement can be tuned by the substrate quality. A recent study demonstrated the effect of surface quality of graphite on subsequent growth of pentacene resulting in different crystal structures [15]. Well-defined graphite surface features atomically flat terraces extending over a few micrometers. On this micrometer ultra flat surface, pentacene molecules adsorb epitaxially with the long molecular axis parallel to the surface. Increasing the defect density of graphite by argon sputtering the surface, for instance, results in a rough texture and surprisingly in an upright orientation of the aromatic backbone [15]. Moreover, the polymorphic structure depends strongly on growth conditions [13, 5]. Deposition conditions such as substrate temperature play a major role. Higher substrate temperature during pentacene deposition on SiO_2 is

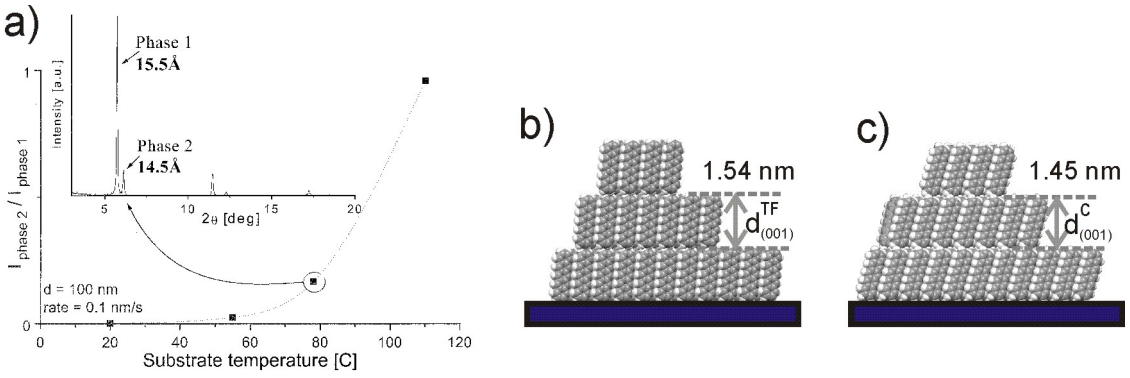

Figure 3.1: a) The ratio of $(001)_{\mathbf{TF}}$ to $(001)_{\mathbf{C}}$ as a function of substrate temperature ($T_{substr.}$). Inset: X-ray diffraction pattern of a pentacene film deposited at $T_{substr.} = 351\,\mathrm{K}$ on SiO_2 [13]. Schematic representation of the molecular packing motif of (001) plane of pentacene in b) **TF** phase and c) **C** phase on SiO_2.

found to modify the stacking of the molecules within the organic layer (Fig. 3.1) leading to a different crystal structure (Campbell phase, **C**) compared to room temperature deposition (*thin-film* phase, **TF**) [13].

Therefore, we first focussed on achieving highly-defined surface of ZnO. The inorganic single crystals were prepared carefully using a protocol developed by our group. The preparation comprises argon ion sputtering at 0.8 keV in an ultra high vacuum (UHV) apparatus. Subsequent annealing at 1200 K for 60 min in ambient atmosphere produced a highly-defined surface of a few hundred nanometer long terraces separated by a single atomic layer [22]. The zinc oxide surface used in this work relates to the oxygen-terminated *c*-plane of ZnO single crystal, $ZnO(000\bar{1})$, denoted as ZnO-O. Based on the high quality of the substrate surface, the organic layer was characterized and the effect of the film thickness on optical transitions in pentacene at different temperatures was studied and both set the objective of this paper.

Layers of 10 nm and 100 nm thickness were grown on ZnO-O under UHV conditions and the growth rate was held constant at 0.5 nm/min during pentacene deposition. Investigation of the film morphology was carried out by atomic force microscopy (AFM) in tapping mode. Figure 3.2a depicts the AFM micrograph of 10 nm PEN/ZnO-O. Dendritic islands were formed with diameters up to 3 μm. A thicker organic layer of 100 nm nominal thickness possessed similar features. The dendritic islands extended over more than 5 μm as shown in Fig. 3.2c. A line profile for each case reveals a height of 1.6 nm separating monomolecular flat layers (Fig. 3.2b and 3.2d). This interlayer distance corresponds to standing pentacene molecules, where the (001) plane is formed parallel to the substrate. Therefore, we conclude that pentacene growth on ZnO-O behaves in a similar way as previously reported in studies for pentacene growth on SiO_2 [5, 31].

The fine difference in the *c* unit length of the pentacene phases amounts to ca. 1 Å, which is beyond the resolution limit of the AFM and the structure is therefore revealed

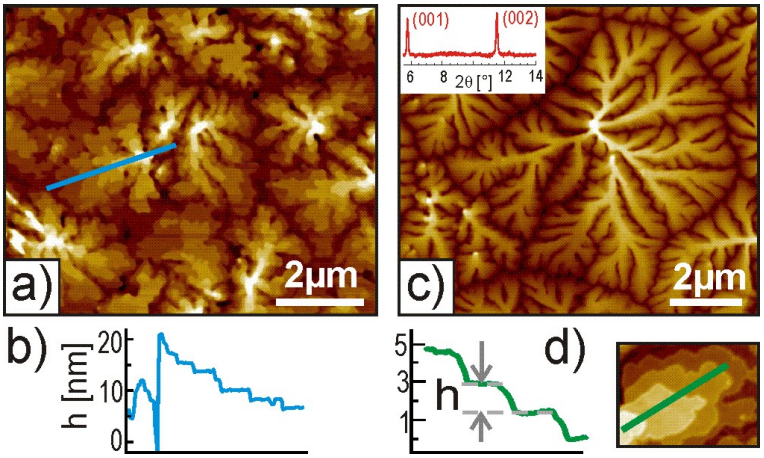

Figure 3.2: AFM micrographs of a) 10 nm and b) 100 nm of PEN/ZnO-O. The corresponding line scans are depicted in b) and d), respectively, showing intermolecular distance in line with upright orientation of pentacene molecules on ZnO-O. Inset in c) shows a typical X-ray diffractogram of the first and second order reflexes of the (00l) plane collected for the *thin-film* phase of $d_{PEN} = 100$ nm on ZnO-O.

by X-ray diffraction (XRD) measurements. A distinct diffraction pattern recorded using Cu K_α radiation at $\lambda = 1.54187$ Å is depicted in Fig. 3.2c (inset) for 100 nm PEN/ZnO-O. The peaks are assigned to (001) and (002) reflexes of the *thin-film* phase in line with findings of pentacene grown on SiO_2 [12, 32]. This indicates that the films are crystalline and the molecules are oriented with their (00l) plane parallel to the substrate surface. The resulting XRD diffractograms support the AFM data proving that pentacene aggregates in a well-defined crystalline structure, the *thin-film* phase, on our metal oxide ZnO-O as well.

For the (001) crystallographic orientation, optical absorption of the lowest transition of pentacene on SiO_2 has been recently reported [33], where a significant thickness dependence was observed. In Fig. 3.3, optical absorption spectra for pentacene on ZnO-O are given, measured at room temperature for the energy regime 1.75 eV - 2.6 eV of linear polarized light. For $d_{PEN} = 100$ nm, the Davydov-splitted excitonic transition (E_+ and E_-) as well as the HOMO-LUMO bandgap were identified (cf. Fig. 3.3a). The peak at higher absorption energies is attributed to vibronic replica of the bandgap as defined in the work of Hinderhofer *et al.* [34]. The intensity of the Davydov-splitted transition dipole moment was verified by recording absorption using linear polarized light. The absorption was recorded for a region with a single crystalline island using a 2 μm aperture as illustrated in Fig. 3.3d. The intensity of E_+ and E_- reveals a distinct dependence on angle of light incidence as shown in Fig. 3.3b. This can be understood when keeping in mind that the direction of the first transition dipole moment is located along the short molecule axis. Considering the packing motif of the unit cell (cf. Fig. 3.3c), this direction is almost aligned within the (001)-plane.

Thickness dependence of optical absorption of pentacene films on ZnO-O was investi-

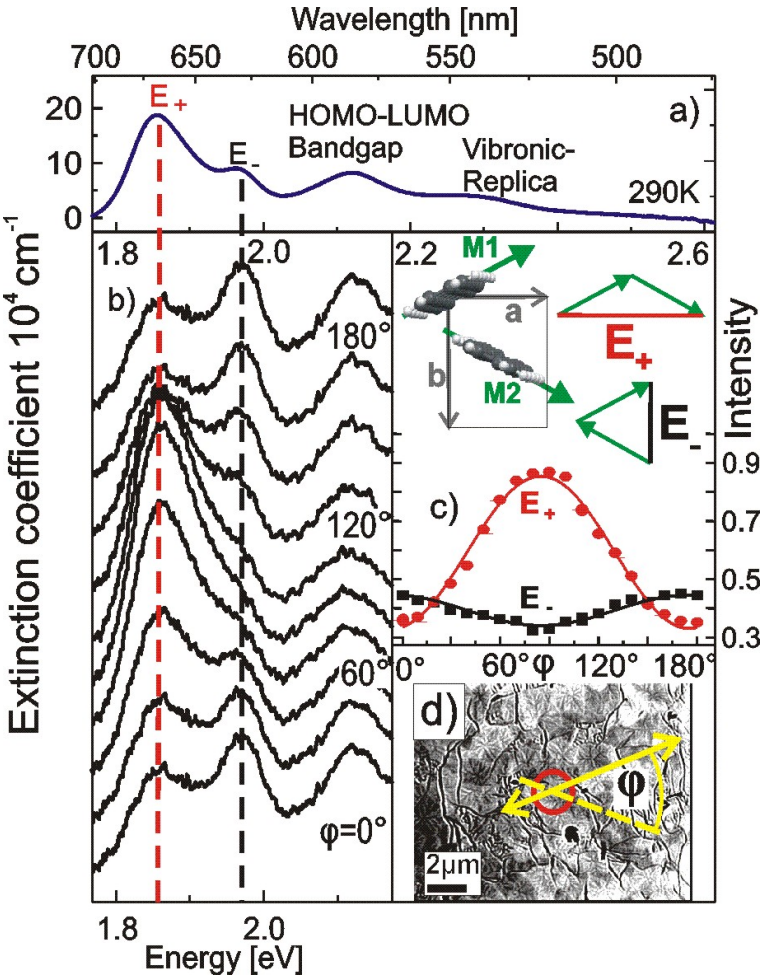

Figure 3.3: a) Optical absorption spectrum of 100 nm PEN/ZnO-O at room temperature. b) Absorption spectra for the same sample at room temperature collected for linear polarized light in 20 ° rotation steps around the surface normal. c) Lowest transition dipole moment in pentacene shown for its unit cell and the resulting intensity of the Davydov components in dependence on angle of polarization. d) Microscopic snap shot of the measured area.

gated at room temperature for 10 nm and 100 nm layers at the beginning. Corresponding optical spectra are shown in Fig. 3.4a and demonstrate the absence of any energy shift, in contrast to previous findings for PEN/SiO_2 [33]. Cooling the system down to 10 K resulted in a red shift of the excitonic transition of the 100 nm film which stands in agreement with earlier optical studies of pentacene on KCl [35] and SiO_2 [30]. Whereas for the 10 nm PEN/ZnO-O a blue shift was observed (Fig. 3.4b) which is found to be attributed to strain effects evoked by the large difference in thermal expansion of the organic and inorganic components. A comprehensive plotting of the energy positions of E_+ and E_- is summarized in Fig. 3.5 and proves again the red shift for both Davydov components as a function of temperature for $d_{PEN} = 100$ nm. On the other hand, both peaks show a blue shift for $d_{PEN} = 20$ nm and for $d_{PEN} = 10$ nm which increases with decreasing thickness of the organic layer. Other aspects are additionally discussed at this point. For instance, the hysteresis of energy shift is noticeable upon cooling and subsequent warming up and is more substantial for thicker layers. This phenomenon can be explained by the activation energy reached at temperature T while warming up which is dissipated for healing the rifts caused within the organic layer upon cooling.

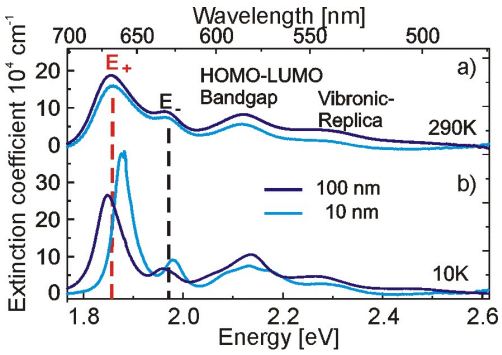

Figure 3.4: Optical absorption spectra of $d_{PEN} = 100$ nm and $d_{PEN} = 10$ nm a) at room temperature and b) at 10 K showing different shift direction at low temperatures depending on pentacene film thickness.

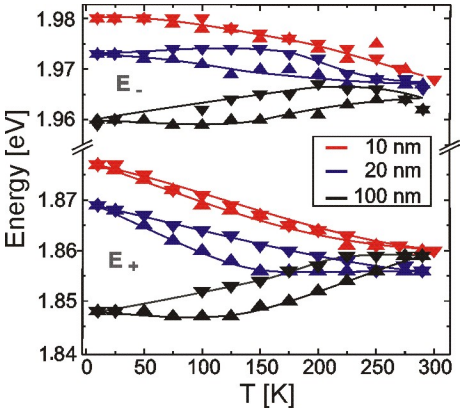

Figure 3.5: Absorption energy peaks of E_+ and E_- for 100 nm, 20 nm, and 10 nm pentacene layers upon cooling from room temperature down to 10 K ($\bigtriangledown$) and subsequent warming up ($\bigtriangleup$).

The strain effect discussed above for 10 nm pentacene film on ZnO-O is supported by further analyzing the temperature dependent E_+ energy position for thin pentacene films on other inert, transparent substrates. KCl and polyethyleneterephthalate (PET) were chosen since they possess larger thermal expansion coefficients (α) than zinc oxide. PET features the highest value among the substrates studied and the smallest difference to α_{PEN} as can be extracted from Tab. 3.1.

Both 10 nm and 100 nm pentacene films were grown on KCl and PET. The AFM micrographs revealed the expected dendritic growth of the organic semiconductor similar to the case on ZnO-O regarding crystal structure (not shown) and orientation. Optical absorption spectroscopy of all three cases for both film thicknesses is summed-up in Fig.

Table 3.1: Overview of the normalized thermal expansion coefficients α at room temperature.

	PEN	ZnO-O	KCl	PET
$\alpha \times 10^{-5}$ [K^{-1}]	11 along $\vec{a}$ 3 along $\vec{b}$	along $\vec{a}$ 0.5	4	7

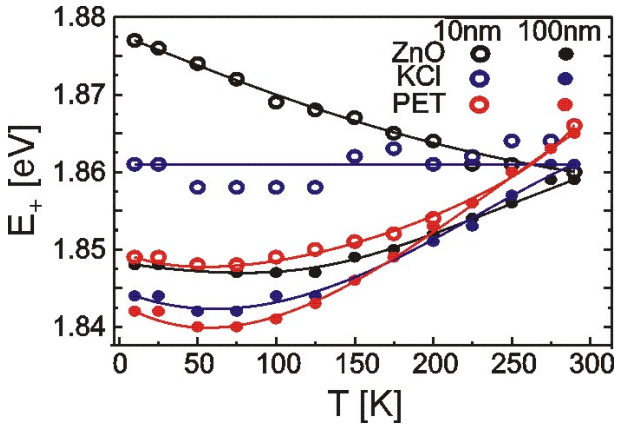

Figure 3.6: Temperature dependence of E_+ of 10 nm (○) and 100 nm (•) of pentacene deposited on materials with different α: case of ZnO-O, KCl, and PET upon warming up.

3.6 for the E_+ exciton state component. As a matter of fact, red shift of the thicker aromatic layer was observed for all substrates (Fig. 3.6 filled circles). Taking into account the difference in the energy shift between room temperature and 10 K measurements for $d_{PEN} = 10$ nm, a distinct behavior is noticed: surprisingly, pentacene films deposited on PET exhibit a red shift in both cases which is not the case for ZnO and KCl. PET is an organic material with a smaller difference in the thermal expansion coefficient with respect to α_{PEN}, therefore, the temperature-dependent shift behavior in case of KCl and above all ZnO can be explained by strain effects in thin pentacene films due to large difference in expansion at the interface.

Personal contribution:

My contribution covers the preparation of ZnO crystals and their characterization by AFM and LEED before mounting them in the UHV apparatus for organic layer deposition. Pentacene evaporation as well as characterization by AFM and XRD have been carried out by me. I also provided PET samples, while the KCl samples have been kindly provided by Tobias Breuer. Jonatan Helzel has carried out the optical measurements. I contributed to writing the manuscript for the experimental part and results for the samples used in this study as well as revising the manuscript. This paper has been kindly supervised and revised by Prof. Gregor Witte and Prof. Wolfram Heimbrodt.

3.2 Optical absorption spectroscopy of different crystalline pentacene thin films on ZnO$(000\overline{1})$

Published in:

M. El Helou, J. Helzel, W. Heimbrodt, and G. Witte (2012), in preparation.

Summary:

In section 3.1, the optical absorption of pentacene has been investigated in the temperature range between 10 K and 290 K while varying the film thickness. All samples used for that study were crystalline pentacene films adopting the *thin-film* phase (**TF**), which is one of three crystalline phases reported for this oligoacene. Previous studies showed that the packing motif of pentacene on SiO_2 could be tuned by controlling growth parameters such as the substrate nature, substrate temperature during deposition, and film thickness [31, 13, 5]. Indeed, optical absorption of such pentacene layers deposited on a substrate as SiO_2 or glass has mostly been investigated experimentally so far [30, 36]. Theoretical predictions were reported for pentacene single crystals in the Campbell (**C**) and Siegrist (**S**) polymorphs [37]. On the other hand, ellipsometric studies were carried out for films in the bulk phase coexisting with the *thin-film* phase in order to deliver the optical constants experimentally [30]. In this section, we aim to investigate the optical properties of pure bulk phase (Campbell phase) films on ZnO substrate and compare the optical transitions between (**TF**) and (**C**) to study the effect of polymorphs on optical absorption.

For this purpose, the variable substrate temperature was set during deposition and the resulting film morphology and crystal structure were determined by AFM and XRD, respectively. Pentacene was first deposited on ZnO-O which was carefully prepared following the procedure reported by Götzen *et al.* [22]. The substrates were subsequently transferred into a UHV ($p = 1 \times 10^{-8} mbar$) and the substrate temperature was stabilized at 136 K, 300 K, 349 K, and 350 K before pentacene deposition. An attempt to aggregate pentacene on ZnO-O held at 351 K resulted in poor sticking of the molecules. All four samples were brought to room temperature before transferring them to ambient conditions for *ex situ* film analysis. In Fig. 3.7, the morphological evolution of pentacene films on ZnO-O is shown as a function of growth temperature. Film morphology for deposition at 136 K witnesses high grain density with random topographical features (s. Fig. 3.7a). The grains grown were around 100 nm in height and 50 - 100 nm in lateral dimension. They can be referred to as crystallites at the nanometer scale as depicted in the line scan in Fig. 3.7a and are considered amorphous with respect to crystallites of 10 μm in size grown at room temperature (s. Fig. 3.7b). At elevated temperature (349 K), the dendritic features as well as bulky islands are formed as imaged by AFM in Fig. 3.7c. When growing pentacene at a slightly higher substrate temperature of only 1 K (350 K), a different crystalline morphology aggregates and pronounced dewetting takes place. The morphology of these crystallites exhibited rather compact islands with well-formed edges (s. Fig. 3.7d) which significantly differs from dendritic growth at room

temperature. The line scan along one crystal revealed molecular terraces separated by 1.6 nm which indicates upright standing molecules as well and hence, no significant height difference to step edges analyzed for room temperature deposition.

Since crystal structures of pentacene polymorphs differ only by a few tenths of an Angstrom, X-ray diffraction is used to clearly resolve the various crystalline phases. In Fig. 3.8, $\theta - 2\theta$ scans were collected in a Bragg-Brentano geometry at room temperature for all four layers using a Cu K_α anode (1.54187 Å). The diffractograms reveal a significant behavior of the diffraction patterns. For low temperature deposition, no diffraction reflexes could be detected which can be explained by the low order of layer crystallinity as almost amorphous films. Room temperature deposition results in the expected *thin-film* phase ($2\theta^{(001)} = 5.73°$), whereas two diffraction signals were detected for growth at 349 K (s. Fig. 3.8) and prove the coexistence of two crystalline phases. The peak at higher $2\theta^{(001)}$ value (6.15°) is consistent with the Campbell phase which is not formed at room temperature. Moreover, increasing surface temperature to 350 K during molecular beam deposition (MBD) resulted in a single crystal structure related to the Campbell phase as reflected by the XRD data in Fig. 3.8 and ensured the absence of any other crystalline phase. The (001) peak at $2\theta_{\mathbf{TF}} = 6.15°$ supports the conclusion of upright oriented molecules, these being packed along the $\vec{c}$-direction with respect to the surface normal, i.e. an *ab*-plane is formed in the surface plane. Any further attempt for deposition at higher substrate temperatures failed due to the significantly reduced sticking properties of the pentacene molecules and the simultaneous high desorption rates (low sticking). All in all, two distinct polymorphs of pentacene have been successfully prepared on ZnO-O by MBD and characterized by AFM and XRD. While dendritic islands extending over a few microns were the finger prints for **TF** phase, the **C** phase stood out due to its bulky and well-defined grain boundaries of around 1 μm in size with a certain degree of dewetting on ZnO-O.

Table 3.2: Lattice constants for pentacene unit cell adopting the *thin-film* phase (**TF**) [12] and Campbell phase (**C**) [11].

	a [Å]	b [Å]	c [Å]	α [°]	β [°]	γ [°]	ΔD [°]
TF	5.96	7.60	15.61	81.25	86.56	89.80	54.1
C	6.06	7.90	16.01	67.4	78.1	85.8	50.9

For these two packing motifs, optical absorption at room temperature was been carried out and compared to the amorphous pentacene layer as summarized in Fig. 3.9a. Here, we are interested in resolving optical characteristics for the different crystalline phases of the same molecule, pentacene. After the morphological and structural analysis mentioned above, the samples were passed on to further optical absorption spectroscopy. The comparison of the crystal structure data for the two phases is listed in Tab. 3.2. The *ab*-plane possesses unequal cell lengths and the herringbone angle is different as well. The Davydov energies ensure a significantly larger splitting of the **C** phase than of the **TF** phase taking into account the different herringbone angles within the unit cells of the two crystalline phases shown in Fig. 3.9b ($\sigma_{\mathbf{C}} = 50.9°$) and Fig. 3.9c ($\sigma_{\mathbf{TF}} = 54.1°$)

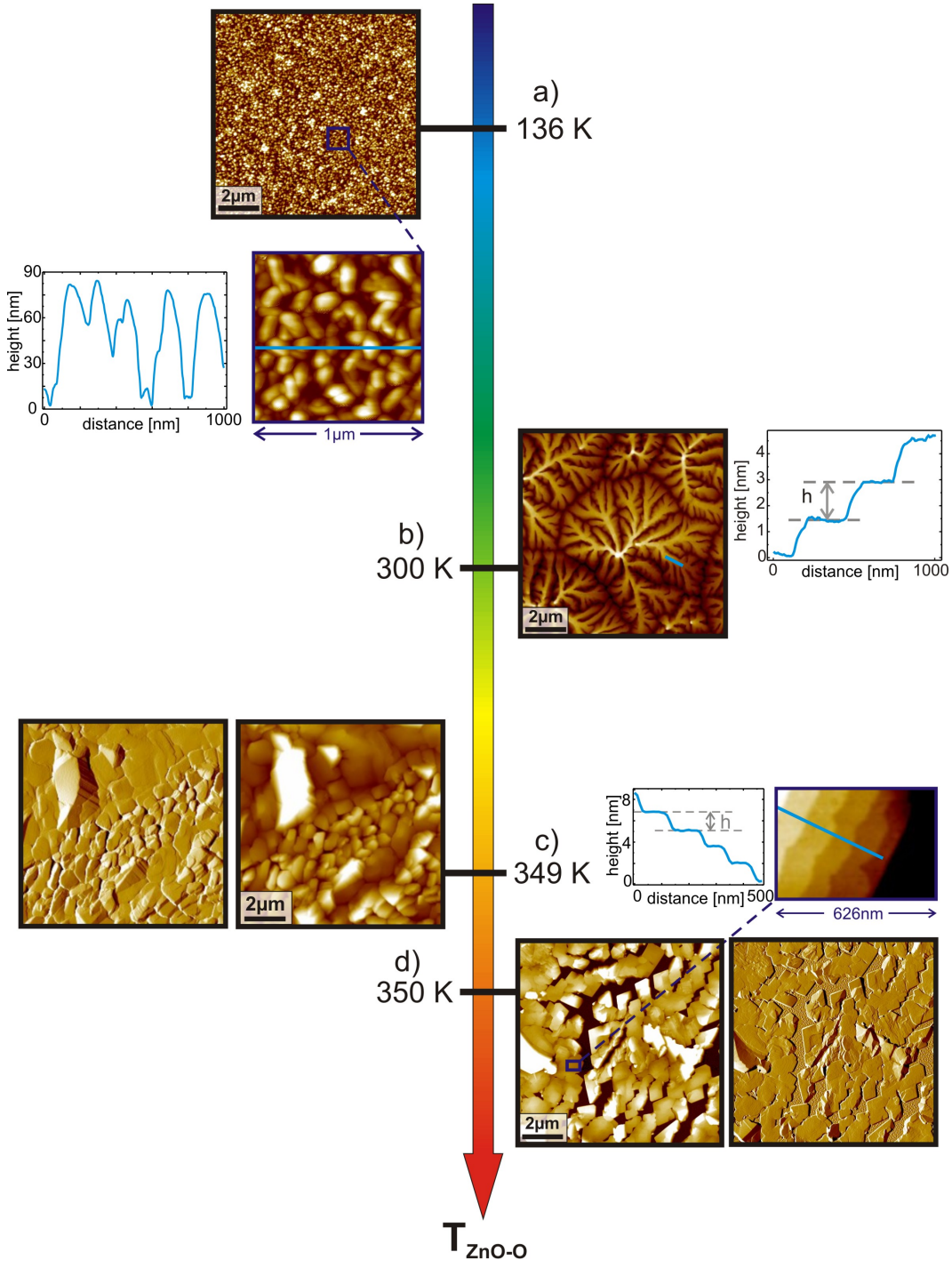

Figure 3.7: AFM micrographs scanned *ex situ* at room temperature of a) 50 nm, b) 100 nm c) 100 nm, and d) 50 nm PEN/ZnO-O, where ZnO-O was held at 136 K, 300 K, 349 K, and 350 K substrate temperature, respectively, during molecular growth in UHV. The height range amounts to a) 130 nm, b) 100 nm, c) 750 nm, and d) 350 nm. Intermolecular distance, in case possible, shows for different morphological features a consistent value of 1.6 nm being in line with upright orientation of the molecules.

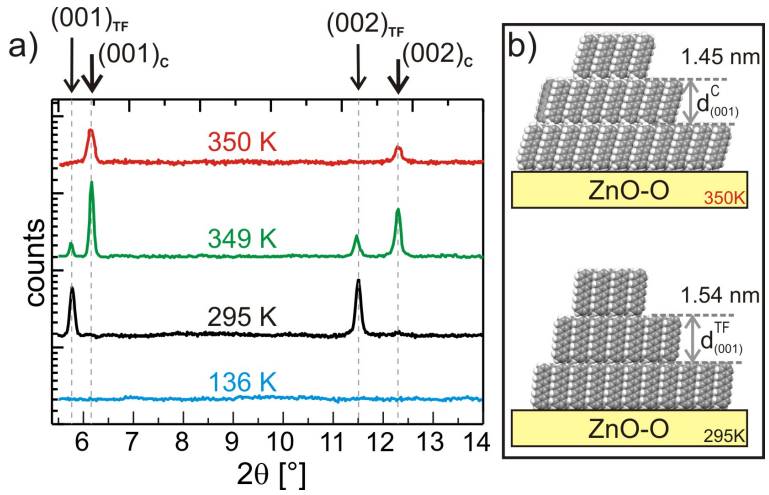

Figure 3.8: a) XRD data of PEN/ZnO-O deposited at different substrate temperatures showing first and second order reflexes of the (00l) plane and absence of any diffraction for low temperature deposition. Data was collected using Cu K_α radiation at 1.54187 Å. b) Side-view of the resulting **C** and **TF** phases on ZnO-O.

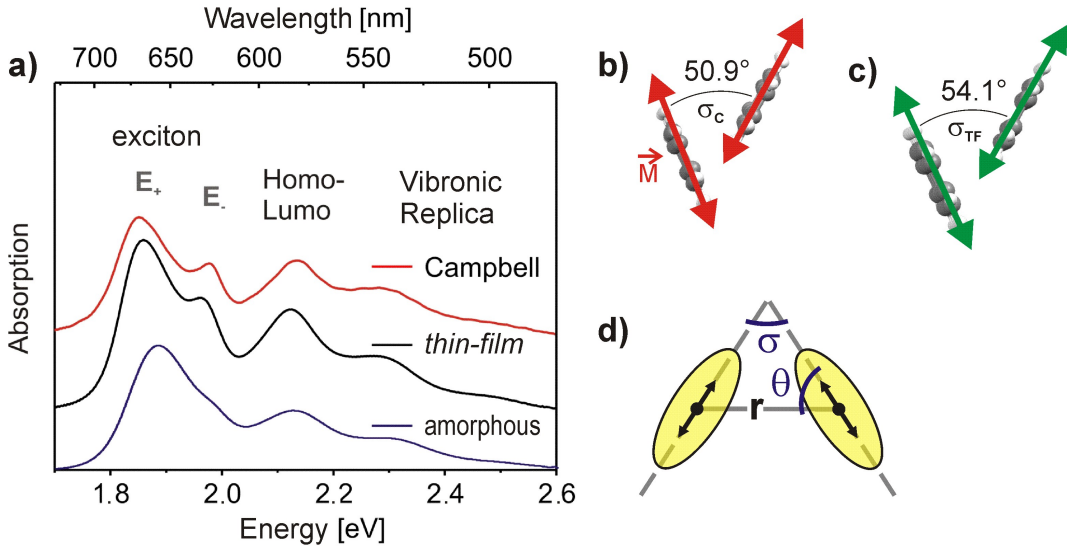

Figure 3.9: a) Absorption spectra of pentacene films on ZnO-O characterized earlier by means of AFM and XRD. The spectra were recorded at room temperature and reveal individual energies for excitonic states for different packing structures of pentacene, i.e., Campbell, *thin-film*, and amorphous phase. Top-view on herringbone angle σ in the *ab*-plane of pentacene resulting from the unit cell at room temperature for b) **C** and c) **TF** phase. d) *Oblique* transition dipoles in a molecular dimer.

extracted from crystal structure data at room temperature. Furthermore, the absolute positions of E_+ and E_- are shifted as well. The data is summed up in Tab. 3.3. The

direct relation of certain molecular configurations in a given periodic pentacene lattice to the Davydov splitting has been described by Hesse *et al.* [36]. Davydov splitting is a result of a crystal effect due to a lattice periodicity. The splitting energy can be thus subject to the herringbone angle in the crystalline phase which is summarized in Fig. 3.10. In a parallel configuration ($\sigma = 0°$), only one discrete optical transition exhibiting parallel transition moments is allowed.

Table 3.3: Peak positions of the Davydov components E_+ and E_- as well as the Davydov splitting ΔD at RT extracted from Fig. 3.9 for pentacene films adopting the *thin-film* phase (**TF**) and Campbell phase (**C**).

	E_+	E_-	ΔD
TF	1.860 eV	1.960 eV	100 meV
C	1.845 eV	1.975 eV	130 meV

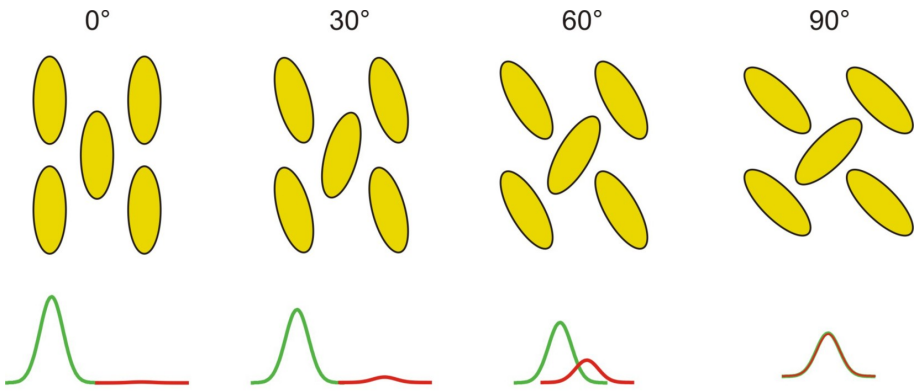

Figure 3.10: The Davydov splitting in a periodic lattice depends on the molecular configuration. No doublets for transition states is allowed for parallel transition moments as showed in the first illustration. Image kindly provided by J. Helzel

Thus, the larger the angle σ between the transition dipole moments for the component absorbing units is the smaller the exciton band splitting. Different intermolecular distances and herringbone angles were determined to be the crucial factors for the Davydov splitting as reported earlier by A. S. Davydov [38]. According to an extended work by Kasha *et al.* [39], the exciton splitting energy is given by:

$$\Delta D = \frac{2\,|M|^2}{r_{uv}^3}\left(\cos\sigma + 3\cos^2\theta\right) \tag{3.1}$$

M is the lowest transition dipole moment positioned along the short molecular axis, r is the center-to-center distance between molecules u and v, σ is the angle between polarization axes for the component absorbing units and θ is the angle made by the polarization axes of the molecule in the unit cell with the line of molecular centers (cf.

Fig. 3.9d). We conclude that the enhanced transfer integrals in the **C** phase with a smaller herringbone angle result in somewhat larger energy separation than in the **TF** phase. The amorphous phase revealed a degree of crystallinity since broad but detectable Davydov peaks were measured. This is most probably contributed to the warming up of the sample to room temperature acting as an annealing step and therefore resulting in nanocrystallite formation or short-range order. Davydov splitting vanishes completely in solution or in a random system. The optical absorption at room temperature can indeed resolve the crystalline phase for highly ordered pentacene films deposited on ZnO-O.

Personal contribution:

My contribution covers the preparation of ZnO crystals and their characterization by means of AFM and LEED before mounting them in vacuum for organic layer deposition. Pentacene evaporation as well as characterization by AFM and XRD have also been carried out by me and the data analysis. Jonatan Helzel has carried out the optical measurements and provided his results. The manuscript is still in preparation.

3.3 Structure & optical absorption of PEN on low-indexed ZnO

Title of publication:

"Structural and optical properties of pentacene films grown on differently oriented ZnO surfaces"

Published in:

M. El Helou, E. Lietke, J. Helzel, W. Heimbrodt, and G. Witte, Journal of Physics: Condensed Matter (2012), submitted.

Summary:

Understanding optical processes is crucial for optimizing and controlling the function in p-n junctions constituting of hybrid semiconducting material as recently highlighted in solar cells or diodes. Such materials are based on organic-inorganic interfaces offering a new field in the semiconductor industry. In case of zinc oxide, applications in opto-electronic devices as an optical transparent oxide are becoming inconceivable due to the prominent advantages of ZnO crystals such as high crystalline order. Yet, the different chemical reactivity witnessed in the field of heterogeneous catalysis of such metal oxides has proven to be nontrivial against adsorption of organic matter. For instance, molecular orientation of p-sexiphenyl (6P) films formed on ZnO depends inevitably on the target plane of the inorganic single crystal as published by Blumenstengel *et al.* [40].

Figure 3.11 depicts AFM images of 6P submonolayers grown on *c*- and *a*-plane of ZnO single crystal. Apart from different morphological growth, upright standing orientation is adopted on the (0001) plane (Fig. 3.11a), while the molecules on ZnO$(10\bar{1}0)$ are ordered in such a manner that the long molecule axis is parallel to the surface (Fig. 3.11b) resulting in a different morphology as well. Flat lying organic molecules were not only observed in the case of 6P on the mixed-terminated ZnO but for pentacene on rutile $TiO_2(110)$ as well. Depending on orientation, molecular packing motif, purity, and degree of crystallinity, diversity in optical properties can emerge from the same molecule. This motivates a fundamental research field concerning high quality thin film preparation which is not well understood yet. Therefore, in this section, the morphological and structural aspects of pentacene, the organic p-type semiconductor, are presented on ZnO, the inorganic n-type semiconductor, crystal of various orientations comprising (0001), $(000\bar{1})$, and $(10\bar{1}0)$. These surfaces can be classified as follows: (i) polar plane corresponding to the *c*-plane which can be zinc- or oxygen-terminated, i.e., (0001) or $(000\bar{1})$, respectively and (ii) non-polar surface also denoted as the *a*-plane which features Zn-O dimers and thus called mixed-terminated (s. Fig. 3.12). Their chemical properties were discussed and reported to be highly sensitive to hydrogen and water adsorbates which is eliminated by heating the crystals up to 650 K [4].

The film morphology of pentacene is investigated for 10 nm films grown on polar and

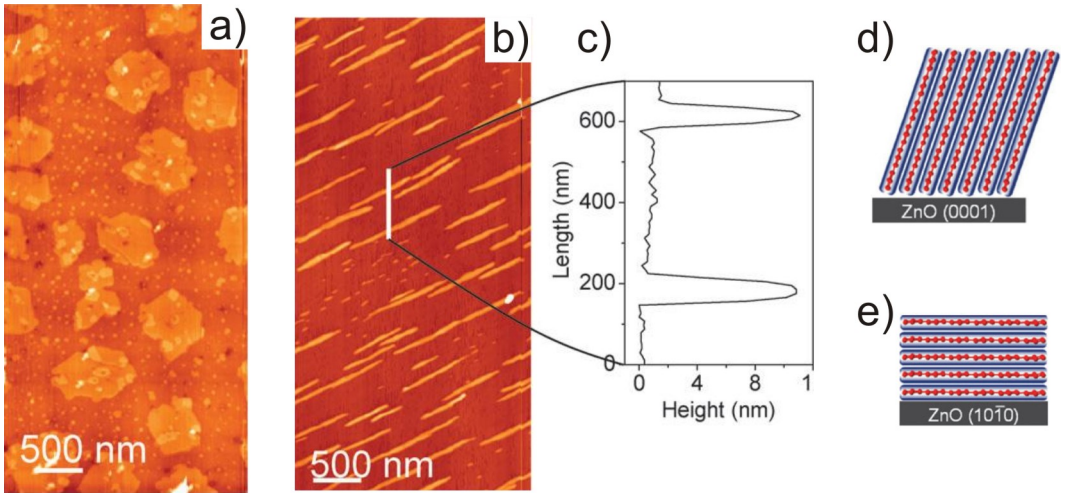

Figure 3.11: AFM images of 1 nm 6p on a) ZnO(0001) at 373 K showing islands of single molecular height conforming almost to molecular length and b) ZnO(10$\bar{1}$0) at 373 K revealing a needle-like morphology corresponding to lying molecules as determined by XRD and the corresponding line profile in c). d) Upright standing and e) lying molecular orientation of 6P on ZnO. These data are published by Blumenstengel *et al.* in [40].

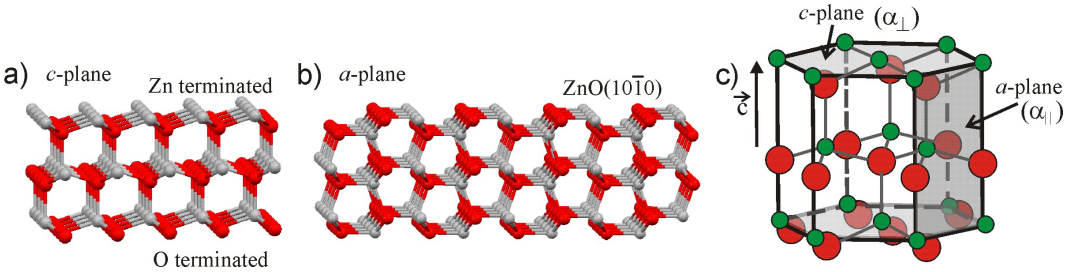

Figure 3.12: Side-view of atomic structure of zinc oxide crystal surfaces. a) Polar *c*-plane with both terminations ZnO(0001) as zinc-terminated (ZnO-Zn) and ZnO(000$\bar{1}$) as oxygen-terminated (ZnO-O) and b) *a*-plane or ZnO(10$\bar{1}$0) as mixed-terminated non-polar crystal surface. Zinc atoms are denoted as gray and oxygen as red balls. c) Crystal structure of wurtzite ZnO (from [22]) showing the (0001) *c*-plane and the (10$\bar{1}$0) *a*-plane where α indicates the thermal expansion coefficient for the cases parallel to $\vec{c}$ ($\alpha_\parallel$) and perpendicular to $\vec{c}$ ($\alpha_\perp$).

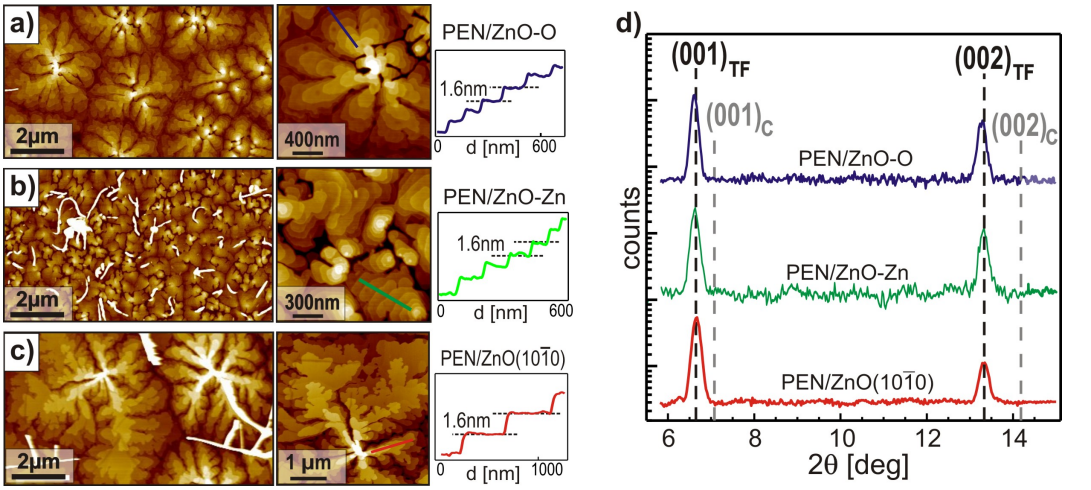

Figure 3.13: AFM images and a zoomed-in area of 10 nm PEN films grown onto a) ZnO-O, b) ZnO-Zn, and c) ZnO(10$\bar{1}$0). The line profiles taken from the magnified micrographs yield a step height indicating an upright orientation of the molecules on all ZnO surfaces. d) $\theta - 2\theta$ scans of 35 nm PEN films grown on the differently oriented ZnO surfaces recorded at $\lambda_{CoK\alpha}$=1.7903 Å. The dashed lines give the expected peak positions calculated from the powder spectra of the *thin-film* phase (**TF**) and Campbell phase (**C**) of PEN.

non-polar ZnO crystal planes and the results are depicted in Figure 3.13a-c. A consistent growth mode is found comprising dendritic islands characterized by monomolecular steps of 1.6 nm upright oriented pentacene with exception for the grain size varying from 2-3 μm on ZnO-O to less than 0.5 μm on ZnO-Zn. The crystal structure was determined by means of XRD with Co K_α radiation (λ=1.7903 Å) and given in Fig. 3.12d. The corresponding θ-2θ scans reveal two distinct peaks at 6.7 ° and 13.4 ° for all samples. These patterns are compared to the expected peak positions calculated from the powder diffractograms of the **TF** and **C** phase of pentacene marked as black and gray dashed lines in Fig. 3.12d, respectively. The observed peaks are clearly assigned to (001) and (002) reflexes of the **TF** phase. Note that no further pentacene diffraction reflexes were observed at larger scattering angles. Therefore, any coexisting phases with smaller interlayer spacing, i.e., recumbent molecular orientation can be excluded.

In some cases, the molecular configuration within the wetting layer differs form that of the subsequent layers as the case for pentacene on Cu(110) which brought us to study the growth mode of pentacene submonolayers on ZnO. The AFM micrograph in Fig. 3.14a of 3 Å PEN/ZnO(10$\bar{1}$0) clearly demonstrates that molecules grow in an upright orientation already in the very first layer on this surface as on SiO_2 [5] and implicates a weak adsorption of the aromatic material in the very early stage of growth. The strength of the molecule-substrate interaction are derived from thermal desorption (TD) data that were collected for PEN submonolayers grown on the various ZnO surfaces. The intensity of desorption peaks increases with film thickness, while their onset stays constant for all cases indicating a zero-order kinetics for desorption and no interface

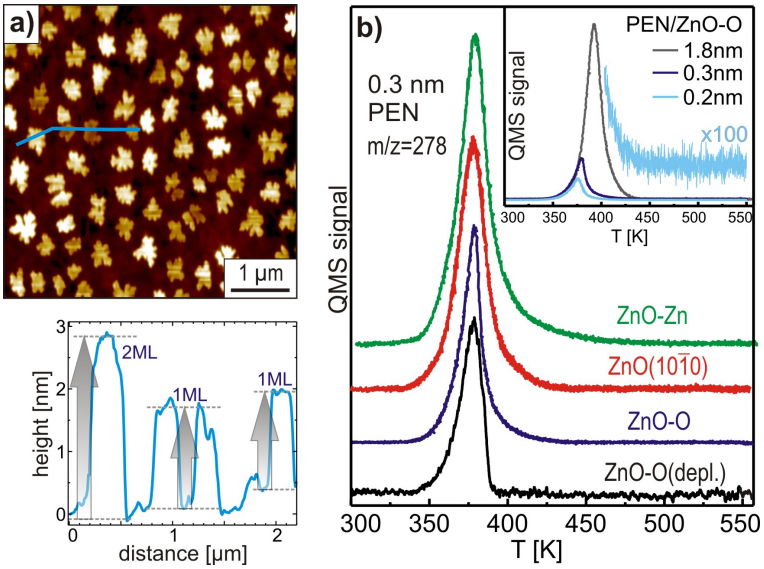

Figure 3.14: a) AFM of 0.3 nm PEN/ZnO(10$\bar{1}$0) at initial film growth with upright molecular orientation from the first layer on. Height of about 1.6 nm and a few h=3.2 nm. b) Series of TDS obtained for 0.3 nm PEN films grown on various ZnO crystal planes. The inset shows desorption signal with the film thickness which can be identified as multilayer desorption. As demonstrated by the magnified spectrum, no evidence for any firmly bound monolayer is found.

stabilized monolayer at higher desorption temperatures is recorded (s. Fig. 3.14b). In the present case, the absence of any additional desorption peak as well as an appearance of multilayer desorption even at submonolayer coverages demonstrate that PEN-ZnO interaction is actually weaker than the mutual interaction which stabilizes the van der Waals bound organic multilayers. Another aspect that influence the chemical properties of the metal oxide is the extensive heating in vacuum, in many cases even considered as a cleaning step. We point out that vacuum heating may cause a partial oxygen depletion leading to gradual metalization of the surfaces as for rutile TiO_2(110) [41]. An oxygen depletion and its influence on related surface roughness have been also examined. The morphology of a heated ZnO-O crystal up to 1350 K in UHV for 30 min before film deposition, denoted as ZnO-O(depl.), is depicted in Fig. 3.15b in comparison to well-prepared surface shown in Fig. 3.15a. In fact, the surface of the vacuum annealed sample exhibits a high density of depressions with diameters of about 20-30 nm and a depth corresponding to multiple interlayer distances as given by line scan II in Fig. 3.15c from Fig. 3.15b. After molecular deposition, the morphological aspect of pentacene on ZnO-O(depl.) is summarized in Fig. 3.15d. It can be deduced that defective surface created by extensive heating in vacuum do not affect the resulting organic film structure and only slightly reduce the crystallite size.

Optical absorption spectroscopy was employed as well in order to characterize the optical properties of the various films and their temperature dependence. They extend

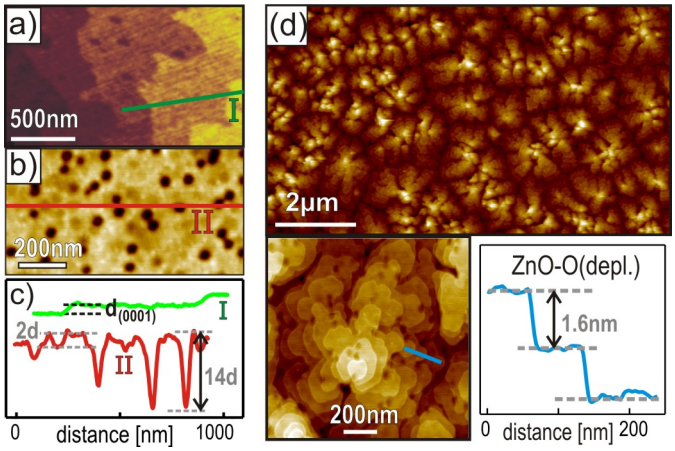

Figure 3.15: AFM data of PEN/ZnO-O(depl.). Comparison of a) an ideally prepared ZnO-O surface with b) an extensive vacuum heated surface and c) corresponding line profiles showing the formation of characteristic depressions. d) Deposition of PEN films (thickness 10 nm) on ZnO-O(depl.) again yields dendritic islands consisting of upright oriented molecule layers.

indeed our previous work carried out for PEN films grown on the ZnO-O surface [43]. The measured spectra are piled up in Fig. 3.16a and reveal distinct peaks at about 1.85 eV, 1.97 eV, and 2.12 eV as well as a broader feature at 2.28 eV in each case. The first two absorption peaks have been clearly identified as the two Davydov components of the exciton state in crystalline pentacene films (denoted as E_+ and E_-), while the peaks at higher energies correspond to HOMO-LUMO bandgap transition and vibronic replica of this excitation. Thus, the almost identical spectral signature of the various pentacene layers clearly corroborates the afore mentioned result that the molecules adopt a uniform molecular orientation on the various ZnO surfaces. Fig. 3.16b depicts the peak positions of the E_+ component as a function of temperature for PEN films grown on the ZnO-O and ZnO($10\bar{1}0$) surfaces during the first cooling down cycle (denoted as "initial curve") which results in a small but distinct red shift for both surfaces. The reduced exciton energy at lower temperatures can be related to the reduced intermolecular distances caused by the large thermal expansion coefficient of PEN which in turn enhances the molecular transfer integrals and consequently the bandwidths, eventually resulting in a reduced bandgap [44, 45]. By contrast to the initial curve, closed hysteresis loops were observed for the E_+ peak position upon subsequent cooling down and warming up cycles as depicted in Fig. 3.16c for PEN films grown on *c*- and *a*-plane of ZnO single crystal. For all following measurements, the results are found to be reproducible to the subsequent curves. The hysteretic behavior is also observed in all cases for 35 nm pentacene films. When increasing the temperature, the exciton shifts appear delayed and indicate the requirement of an activation energy for healing of rifts developed from cooling down and other crystallographic defects. Moreover, ZnO has rather anisotropic thermal expansion coefficients with $\alpha_\perp$ (perpendicular to *c*-axis) being almost twice as large as $\alpha_\parallel$

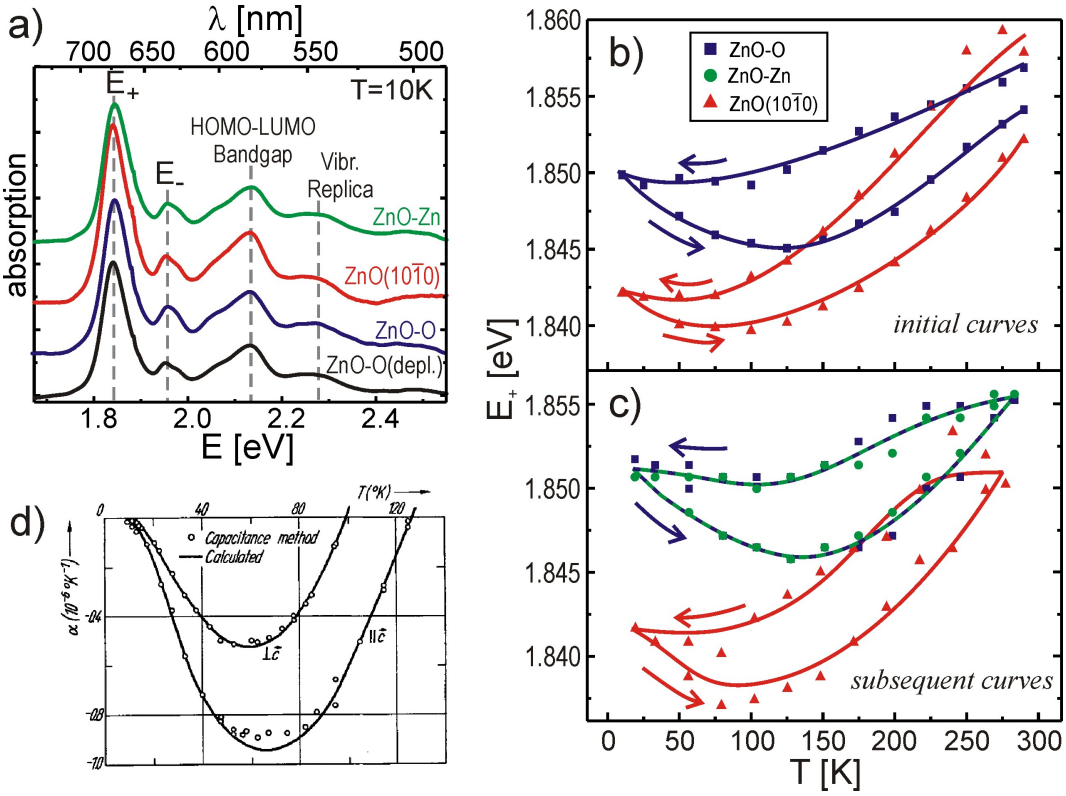

Figure 3.16: a) Comparison of optical absorption spectra of 35 nm pentacene films grown on differently terminated ZnO crystal surfaces at 10 K. Energy of excitonic E_+ for PEN on different ZnO surfaces upon cooling down and warming up between RT and 10 K for b) initial curves and c) subsequent measurements to the initial curves. d) Negative thermal expansion coefficient part of ZnO as a function of temperature from [42].

(parallel to *c*-axis) [42] (s. Fig. 3.12c). Therefore, the difference in thermal expansion between PEN and ZnO is expected to be largest for the mixed-terminated ZnO surface (i.e. *a*-plane) which describes the different behavior between both planes. Interestingly, the thermal expansion coefficients of ZnO around 80-120 K exhibit a change in sign (cf. Fig. 3.16c) yielding the largest density around 100 K which is likely to cause the minimum in the temperature dependent exciton curves. In summary, only a slightly different relaxation behavior upon cooling was observed for pentacene films on polar ZnO surfaces compared to pentacene on the mixed-terminated ZnO($10\bar{1}0$). The growth mode of pentacene which results from a weak substrate interaction appears to be rather robust which is advantageous for the fabrication of organic-inorganic semiconductor hybrid systems based on polycrystalline ZnO substrates [2].

Personal contribution:

My contribution covers the preparation of ZnO crystals and their characterization by means of AFM and LEED before mounting them for organic layer deposition. The defective ZnO-O(depl.) was kindly prepared by Eugen Lietke and characterized with AFM. Pentacene evaporation on all four kinds of surfaces as well as characterization by AFM and XRD have been carried out by me including the thermal desorption measurements and the interpretation of the data and their processing. Optical absorption data including temperature dependency and the data processing have been executed by Jonatan Helzel. Prof. Wolfram Heimbrodt supported the interpretation of Helzel's data. I received a significant support from my supervisor Prof. Gregor Witte from first draft till submission. This paper has been kindly supervised and revised by Prof. Gregor Witte and Prof. Wolfram Heimbrodt.

Chapter 4

Self-Assembled Monolayers in Photosensors

Title of publication:

"Immobilization of Quantum Dots *via* Conjugated Self-Assembled Monolayers and Their Application as a Light-Controlled Sensor for the Detection of Hydrogen Peroxide"

Published in:

W. Khalid, M. El Helou, T. Murböck, Z. Yue, J.-M. Montenegro, K. Schubert, G. Göbel, F. Lisdat, G. Witte, and W. J. Parak, ACS NANO, **5**, 9870 (2011).

Summary:

Hybrid materials have drawn a tremendous interest in widespread applications particularly in the field of organic/inorganic systems. They represent a new research field and are gaining increasing prominence in exploring and developing new features arising from such interfaces. In this chapter, the main focus lies on light-addressing of nanosized types of inorganic particles with semiconducting properties immobilized on an organic layer of self-assembling molecules. The absorbed photons induce an exciton which emits energy as visible light as fluorescence after recombination of the electron-hole pair in cadmium sulfide (CdS) which is the NP substance covered in this study. QDs of CdS exhibit sizes ranging between 3 nm and 5 nm. Thus, an energy of 355 nm is absorbed and fluorescence emission is characterized to be around 500 nm, i.e. red light. Therefore, this photo-induced exciton in such semiconducting NPs offers a fundamental advantage in photoelectrical systems where the NP can act as an e^- donor/acceptor by exposure to light. In this paper, the photocurrents generated by CdS NPs in presence of phosphate buffer is studied to enhance and optimize efficiency on the one hand and to stabilize the yield over time on the other hand.

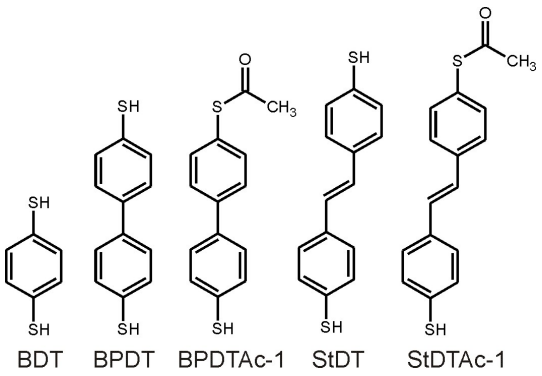

Figure 4.1: Overview of structure and notation of dithiols used in the present work. 1,4-benzenedithiol (BDT), 4-4'-biphenyldithiol (BPDT), monoacetylated BPDT (BPDTAc-1), *trans*-4,4'-stilbenedithiol (StDT), and monoacetylated StDT (StDTAc-1).

Immobilizing such QDs on a metal electrode, for example gold, results in a current leakage due to the nature of the Schottky-contact formed between the semiconducting particles and the metal substrate. Therefore, a spacer is required and is realized by implementing an organic chain as bridging layer inbetween, where in this case, this so-called organic linker is chosen to be a dithiol. The first thiol group (SH) should anchor to CdS and the other to Au forming a dithiolate. This selective binding of thiols to gold guarantees self-assembly for these molecules. They tend to form two-dimensional organic crystals of thicknesses equaling a single molecule length known as self-assembled monolayers (SAMs) as first reported by Nuzzo and Allara [46]. The branch of SAMs based on thiols on metals has been reviewed thoroughly by Ulman [47] and Whitesides [6]. Indeed, thiols of alkanes were classified as model systems for self-assembly which aliphatic hydrocarbons possess a wide band gap. With benzene as a backbone, an improved conductivity is preserved due to the aromaticity of the ring which is not the case for the alkanethiols. Note that benzenedithiol (BDT) has been commonly used in previous works based on light-controlled sensors. Due to its large band gap and poorly ordered layers, other dithiols were investigated in this study in order to tune one or both parameters. These molecules are shown in Fig. 4.1 as an overview. All photocurrents shown in this chapter were collected at U=+200 mV in 0.1 M phosphate buffer with a pH of 7.5 at room temperature using 23 mW light power illuminating a 7 mm^2 electrode area.

Photocurrents of a sensor incorporating the CdS-BDT-Au junction are shown in Fig. 4.2. The resulting photocurrent is weak, not stable over time needs improvement. The drift, low signal-to-noise ratio and loss of intensity due to rinsing steps frame the instability of such a junction and present the main challenges for sustainable and reproducible yields of light-addressable sensors and higher current intensities. The drift is reflected by the decrease of the current I_0 within time while switching the light on and off, i.e. the signal measured in the first part of a single cycle. A second cycle involves replacing the existing buffer by new buffer solution which is referred to as a rinsing step resulting

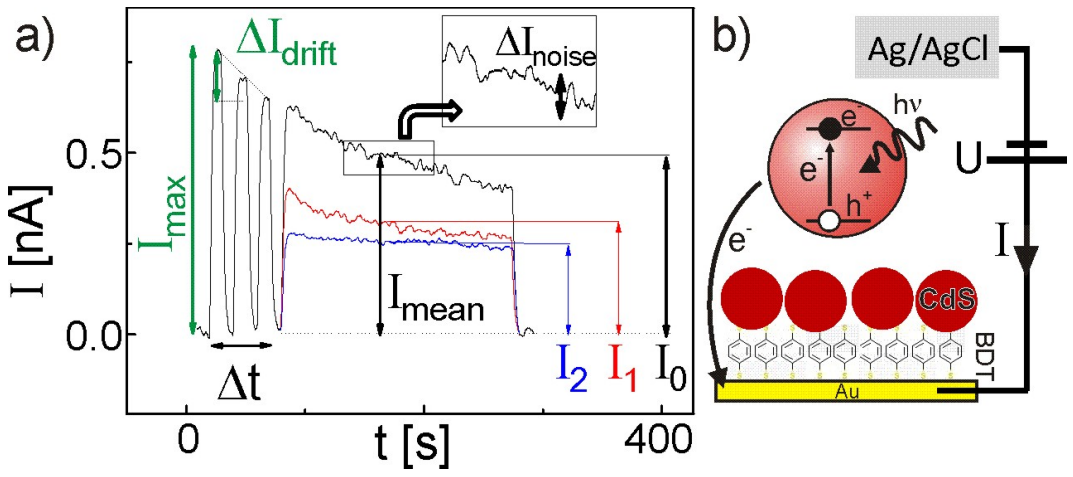

Figure 4.2: a) Photocurrent of BDT as linker between gold and CdS NPs detected over time including measured parameters. b) Setup used as photoelectrical system and photocurrent generation are shown schematically.

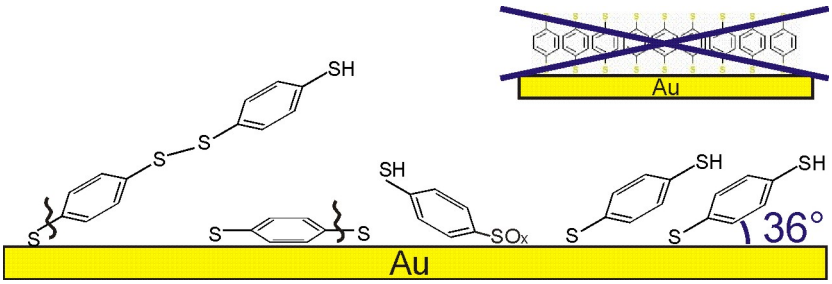

Figure 4.3: Proposed structures of adsorbates of BDT on gold surface. Inset: Ideal structure of BDT assumed when assembled onto Au.

in photocurrent I_1. After a second rinsing cycle, I_2 reveals a huge loss of about 50% compare to I_0. The resulting yield is too low (ca. 0.7 nA) as photocurrents are expected to be at least of an order of magnitude higher.

At this point, the concept of well-ordered assembled monomolecular films of BDT on Au should be addressed. In literature, the true structure is described as rather poor molecular ordering and lack of stability of the molecular film which have been reported for BDT on gold [48]. Beside the single-anchored molecule (Au-S-R-SH), BDT can bond with both thiol species forming a dithiolate or intermolecular disulfide bonds (Fig. 4.3). In fact, it is well documented for benzenethiol (BT) compounds that self-assembly results in a recumbent orientation when formed on Au(111) single crystal surface [49]. Such poorly ordered film structure is result of oxidation of the exposed thiolate species, the thiolate (R-S–Au), to sulfonate (SO_x) in presence of oxygen and ultraviolet light. The oxidized sulfur groups are only physisorbed on the metal surface and can to a certain

extend be pumped away in vacuum. We conclude that densely-packed monolayers are certainly not the case for BDT when exposed to ambient conditions as depicted in Fig. 4.3 (inset).

Note that clean substrates and low defect density are crucial for SAM formation which is not the case for commercially available polycrystalline Au/glass substrates used in the current work. These consist of Au films evaporated on glass with titanium as adhesion layer (100 nm Au/20 nm Ti/glass), but yet denoted as Au/glass. For Au/glass, the morphology of gold has been characterized by atomic force microscopy (AFM) and is illustrated in Fig. 4.4a. Firstly, the scratches demonstrate a high defect density. Secondly, the gold layer is protected by a photoresist which requires chemical steps for elimination leading to contamination that may occupy anchoring sites and hamper chemisorption of the thiol head group. Au/mica produced in a home-made setup, on the other hand, offer a high-quality Au(111) surface with atomically flat regions extending over several hundred nanometers of high purity. In spite of the excellent quality of such Au(111) as shown in Fig. 4.4c, CdS/BDT on Au/mica unfortunately reveals intensities inferior to those of CdS/BDT on Au/glass. Au/mica substrates didn't resist the mechanical stress of the self-made electrochemical cell and were unstable when implemented within the setup in particular upon deprotecting step. Instead, gold was deposited on silicon substrates with native oxide (referred to as SiO_2) by sputter-coating and were self-prepared as well. Keeping in mind that noble metals adhere poorly to oxidized silicon, thin films of 14 nm prove to bear up the electrochemical operations and chemical solutions. Such polycrystalline Au/SiO_2 electrodes resulted in a better current yield and the drift was repealed substantially (Fig. 4.4b). The signal-to-noise ratio was drastically increased for Au/SiO_2 electrodes. The gold substrates were cleaner and showed a smoother corrugation as indicated by the rms (root mean square) roughness values determined from AFM data. Hence, sensors based on Au/SiO_2 are in fact sustainable, since current loss due to a second rinsing step has been alleviated as well. Indeed, best results could be obtained for Au/SiO_2 electrodes, most probably due to incubation in SAM solution immediately after gold film preparation and low surface roughness.

In spite of such notable improvement, the yield of detected current is yet low. The BDT SAMs were then characterized on Au/SiO_2 electrodes using surface sensitive spectroscopic methods. By high-resolution X-ray photoelectron spectroscopy (XPS), the expected poor quality of BDT films on Au/SiO_2 (cf. Fig. 4.5) can be proved. The sulfur signals for the different chemical bondings could not be resolved and oxidized sulfur species were detected with high intensity at higher binding energy. Improved molecular ordering can be achieved for longer SAM backbones due to higher intermolecular interactions.

A rigid backbone with longer chain than benzene is, for instance, biphenyl. Results of photocurrents showed no enhancement ($I < 1\,\mathrm{nA}$) for Au-BPDT-CdS as depicted in Fig. 4.6a (*upper panel*). This is not surprising since earlier studies on structures of biphenyldithiol (BPDT) on Au revealed poor ordering where an intermolecular disulfide bonding and flat lying molecules with both thiols anchored to gold have been observed, as in the case for BDT. Here, chemical modification of the thiol functional group was

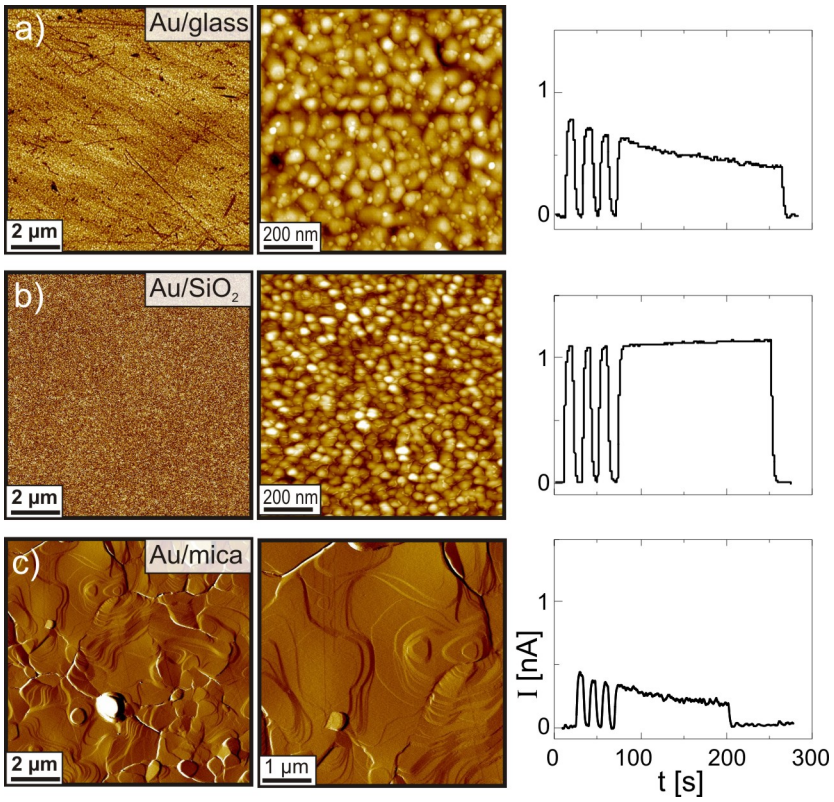

Figure 4.4: AFM micrographs of different Au electrodes $10\,\mu m \times 10\,\mu m$ in size and a zoomed-in area for a) commercial Au on glass after polishing (rms: 3.5), b) Au sputtered on SiO_2 (rms: 1.8), and c) Au evaporated on mica (rms: 0.7) including corresponding photocurrents for BDT-CdS junction. Values of rms roughness values are obtained from $1\,\mu m$ in each case.

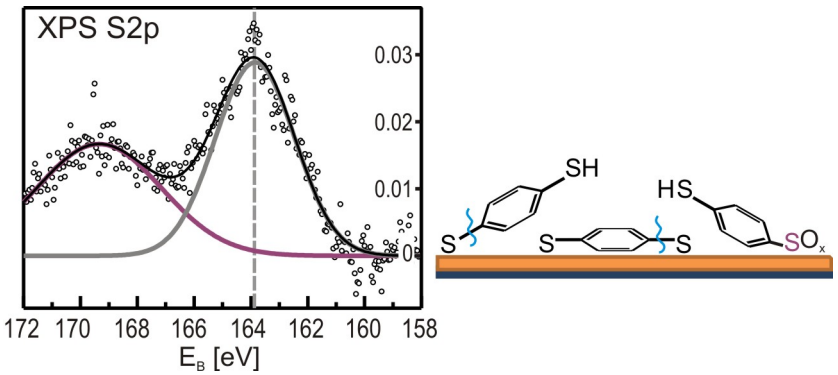

Figure 4.5: XPS of S2p regime detected for BDT on SiO_2 (*left panel*) and a scheme of the possible structure (*right panel*).

suggested [50]. A biphenylthiol forms well-defined monolayers on Au only when protecting one thiol group by an acetate prior to anchoring onto Au, i.e., monoacetylation. This protective group, thioacetate, aims at obtaining chemoselectivity of the thiol anchoring mechanism since thiols possess a substantially stronger affinity to gold than thioacetates. The linker with one thiol capped called BPDTAc-1 was immobilized on gold followed by decapping the acetate before attachment of CdS QDs. After self-assembly, decapping is executed where the thioacetate has been reduced to thiol. Monolayers of well-aligned molecules offering sufficient thiol anchoring sites is expected. Sensor performance mirrors a slight enhancement ($I > 1\,\mathrm{nA}$) as shown in Fig. 4.6a (*lowest panel*). Structural and chemical analysis was carried out for the linker by XPS as well (Fig. 4.6b). Three binding energies of S2p doublets were detected and identified as sulfide (in blue), thiolate (in green), and thiol (in red). At higher binding energies a broad peak was detected (marked in purple). This peak corresponds to oxidized sulfur species, i.e. sulfonates. In summary, the data supports the conclusive picture of well-ordered BPDT SAMs after decapping compared to the disordered BPDT SAMs immobilized directly on gold. For the latter procedure, the intensity of the thiolate signal in XPS dominated that of thiol and, on the other hand, sulfide and sulfonate species were observed as well (cf. Fig. 4.6b (*upper panel*)). Sulfides and sulfonates are undesirable in the first place and underline the bad quality of these SAMs. XPS data for the capping step, i.e. BPDTAc-1 and for its subsequent decapping to a thiol as a free anchoring site for QDs is shown in Fig. 4.6 (*middle* & *lowest panel*). In this case, decapped BPDT formed a more homogeneous layer with upright orientation and significant loss of sulfides and sulfonates indicating more stable films as shown schematically in Fig. 4.6c.

The most prominent reason for such modest enhancement in photocurrent, in spite of the clearly improved ordering of decapped BPDT, is its conductivity. The conductivity of the linker plays an important role for an efficient charge transport between QDs and gold. The HOMO-LUMO band gap (E_g) of BDT amounts to 5.33 eV whereas BPDT has a HOMO-LUMO band gap of 4.64 eV [51]. Longer oligophenylene chains are not expected to lower the gap as reported by Bashir *et al.* [51]. Acenes, however, as fully conjugated system possess an adequate conductivity since the HOMO-LUMO band gaps range between 2 eV and 4 eV for acene rings between 2 (naphthalene) and 5 (pentacene) [51]. Yet, the bad solubility hampered SAM formation in our case as SAMs were prepared by incubation of gold substrates into a dithiol solution. Another material class had been brought into discussion. It consists of fully conjugated backbone and has better solubility than acenes, for instance, stilbenes (1,2-diphenylethene). The low HOMO-LUMO bandgap of *trans*-stilbene of 2.14 eV promises high device performance. The measured photocurrents were summed up in Fig. 4.7 and represent a general overview for the compared systems of StDT. Unfortunately, SAMs based on *trans*-stilbenedithiol (StDT) are not the most adequate system for a good charge transport as reflected in the low currents (Fig. 4.7a). The curve shows no enhancement compared to a BDT-based system. Monoacetylation of StDT, i.e. StDTAc-1 does in fact affect the SAM stability and ordering in this case as well. Fig. 4.7b shows the corresponding current results as it averages to 2.5 nA. However, it was the highest detected so far when using the

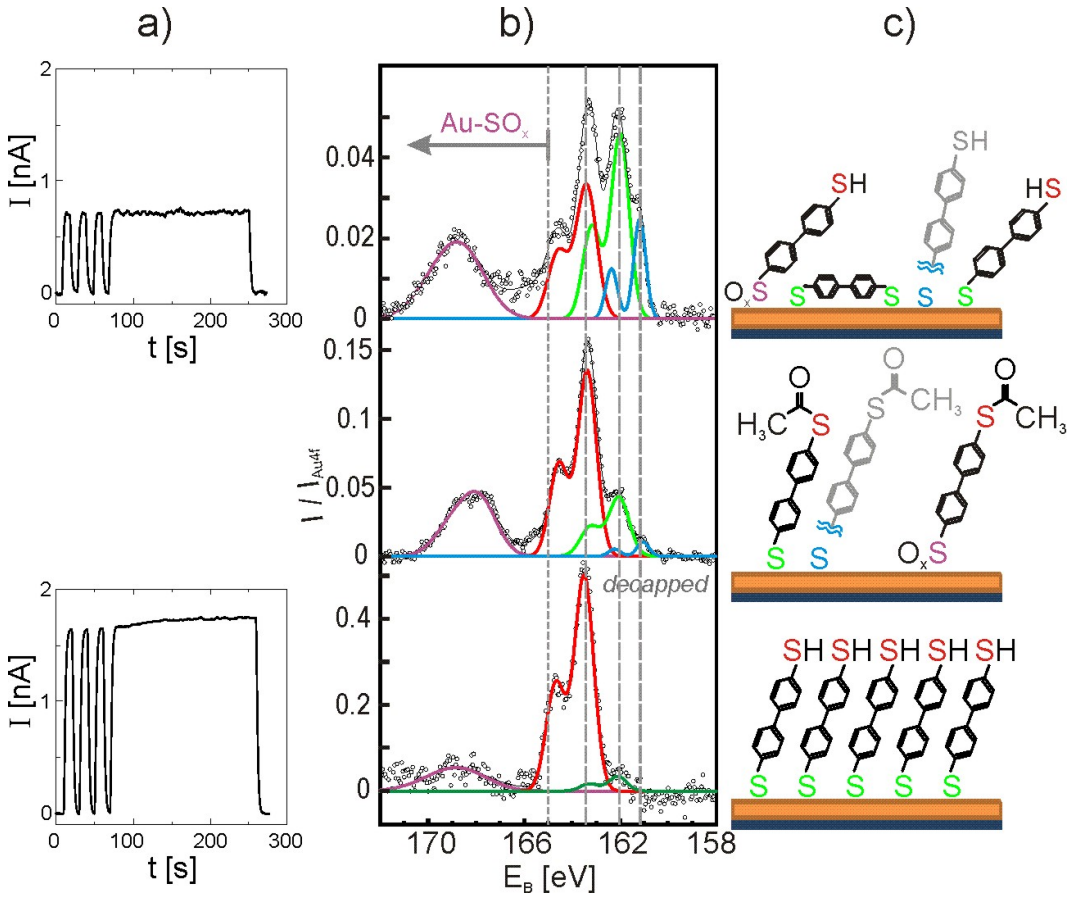

Figure 4.6: a) Photocurrent of BPDT (*upper panel*) with resulting currents of $I = 0.62 \pm 0.1\,\mathrm{nA}$ and decapped BPDT (*lower panel*) of $I = 1.76\,\mathrm{nA}$, b) XPS of BPDT, BPDTAc-1, decapped BPDT on Au/SiO_2, and c) scheme of corresponding structure. Binding energies of different sulfur species are marked in blue for sulfides, green for thiolates, red for thiols and purple for oxidized sulfur species (sulfonates).

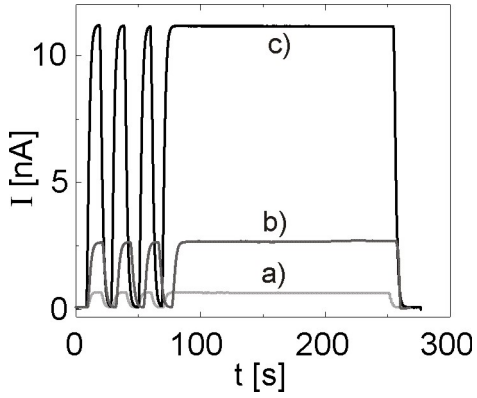

Figure 4.7: Photocurrents of CdS-linker-Au/SiO_2 system based on a) StDT, b) StDTAc-1, and c) decapped StDT as linkers.

capping procedure compared to BDT and BPDT without protecting groups but similar to BPDT using the capping procedure. Note that lab-synthesized StDTAc-1 underwent a photochemical reaction within hours. This disadvantage brought us to an alternative preparation of such conjugated dithiol SAMs. Earlier studies suggest a preparation method by incubation at elevated temperature instead at room temperature [52, 53]. Therefore, Au/SiO_2 was immersed in heated StDT solution at 350 K denoted as hot StDT. This resulted in outstanding current intensities of an order of magnitude higher than that of the commonly used BDT (Fig 4.7c) and excellent stability against drift and rinsing steps. Current loss remained negligible within experimental accuracy even after 2 rinsing cycles.

We look back at the structural and chemical analysis of this linker carried out by XPS. The data is presented in Fig. 4.8 and supports the conclusive picture of poor ordering of StDT prepared at room temperature. Intensity of S2p signal related to thiolate species (green) dominates the one of thiol group (red) and shows a high density of defects in the film (cf. Fig. 4.8a). The challenge of selective anchoring of one head group was solved by capping mechanism as represented for BPDT before and used for StDT for the first time. SAMs based on protective monoacetylation of StDT entail a significant enhancement as shown by XPS where the sulfonate signal has decreased substantially for StDT film after decapping and thiol to thiolate ratio has become larger (cf. Fig. 4.8b,c). Therefore, the protective group does affect the SAM stability and structure in the case of StDT as well. Fig. 4.8d shows the results for the sulfur region of StDT SAMs formed by incubation at elevated temperature (hot StDT). Intense thiol peak (red) and attenuated thiolate signal (green) reveal an upright oriented molecular layer with plenty of exposed thiol species as free anchoring sites for immobilizing CdS NPs. Absence of sulfide groups as well as the alleviated sulfonate signal underline the superior SAM quality. The high packing density of the linker is indeed of great importance, since hot StDT had the best film structure among the electrodes based on StDT (Fig. 4.8c).

The remarkable film quality and long range ordering of hot StDT can be supported by

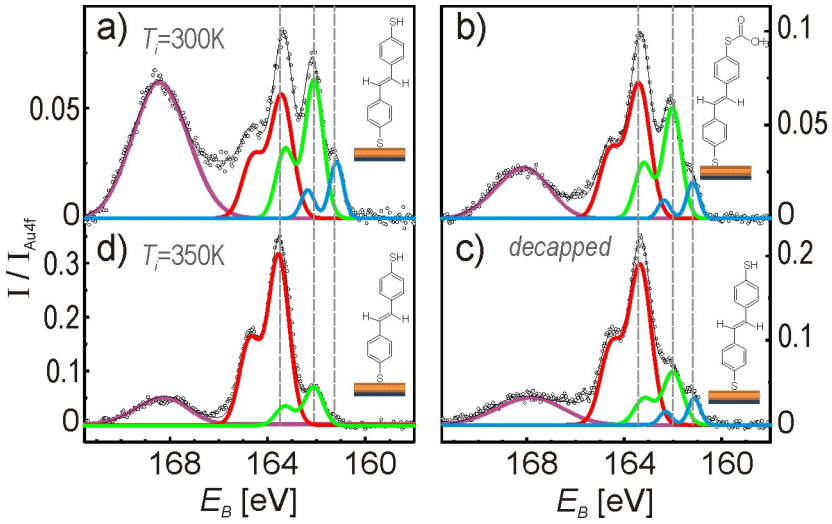

Figure 4.8: XPS data of the S2p region of a) StDT, b) StDTAc-1, c) decapped StDT, and d) hot StDT (incubation at 350 K) on Au/SiO_2.

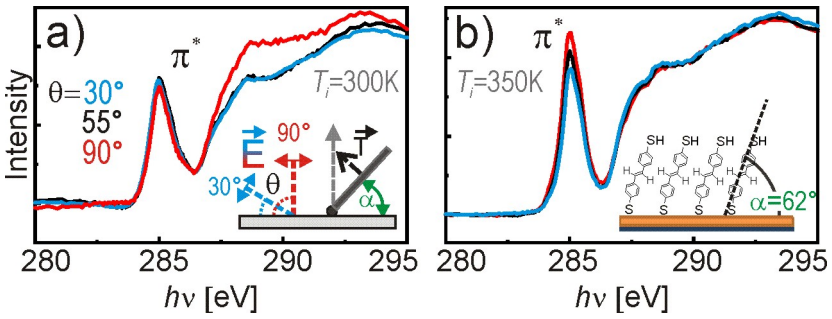

Figure 4.9: NEXAFS at C1s edge of the system a) StDT and b) hot StDT on Au/SiO_2 recorded at different angle of incidence θ of the field vector $\vec{E}$. The angle α denotes the resulting orientation of the molecule with respect to surface plane.

near-edge X-ray absorption fine structure (NEXAFS). Measurements are summarized in Fig. 4.9 and could purvey the orientation of SAMs of hot StDT on gold since a noticeable dichroism is found. The molecules are packed with an average tilt of 28 ° from surface normal (s. Fig. 4.9b (inset)) whereas no preferred tilting angle could be gained for room temperature preparation (s. Fig. 4.9a) because no dichroism occurs. Keeping in mind that highly-ordered BPDT with low conductivity attained insufficient photocurrents shown in Fig. 4.6a (*lower panel*), hot StDT realized both highly-defined structure, long range ordering and adequate charge transfer. Hence, the low band gap of this material class has a crucial impact on device performance as well as their well-packed structure. From undefined and unstable BDT to highly-ordered conductive StDT, a milestone has been achieved regarding the function and efficiency of light-addressable sensors based on CdS NPs.

The optimized system with hot StDT as linker could even prove its outstanding characteristics in acquiring higher detection yield for immobilizing hybrid NPs based on CdS@FePt. The resulting light-controlled sensor can be used for applications in the field of physiology, like the catalysis of hydrogen peroxide also implemented in this study. Such complementary measurements furnish a comprehensive image of this paper for parameter control and high yield and, therefore, serve as an important groundwork for biosensors with peroxide as a product.

Personal contribution:

My contribution covers preparation of Au/mica and Au/SiO_2 substrates of high quality and purity including the morphological characterization as well as SAM modification with all dithiols used in this study. I was also responsible for preparation procedures of the dithiols. The XPS and NEXAFS measurements were carried out by Tobias Murböck at BESSY in Berlin. With his assistance fitting procedure of XPS and NEXAFS data regarding peak assignment and correlation to present systems peak fitting and data calibration of these spectroscopy methods were executed. Synthesis of BPDTAc-1 and StDTAc-1, as well as the NP synthesis, characterization and photocurrent measurements have been carried by the group of Prof. Wolfgang Parak, mostly by Waqas Khalid. The peroxide experiment was encouraged by the cooperation group of Prof. Fred Lisdat in Berlin and executed by Prof. Wolfgang Parak's group (AG Biophotonik). I had the complete contribution for the writings and figures related to organic self-assembly and spectroscopic methods. My work has been carried out under the supervision of Prof. Gregor Witte. The manuscript was kindly revised by Prof. Gregor Witte, Prof. Wolfgang Parak, and Prof. Fred Lisdat.

Outlook

The presented surface characterization in the field of organic-inorganic hybrid materials shows that microscopic understanding is important for predicting and controlling the systems on the nanometer scale using organic compounds. The structural and morphological study of the pentacene with a rigid aromatic backbone on zinc oxide can be subjected, for instance, to other inorganic semiconductors such as MgO or sapphire. These may influence this high membered acene as to induce a tuning in the molecular wetting layer reported for example for *p*-sexiphenyl on ZnO [40]. Moreover, the angular-resolved absorption dependence of the intensity of the Davydov components using linear polarized light can be extended to the other crystalline phases of pentacene on ZnO single crystals, such as the Campbell phase. This crystal structure was selectively prepared. This organic layer formed crystallites of lateral dimensions which are compatible with the aperture used for such measurements. A correlation between molecular arrangement and angle-dependence of the Davydov components can be established using pentacene as model system.

Using an AFM to acquire local conductivity showed that the resulting CSAFM data correlated to temperature and contact resistance as expected for conductivity of semiconducting materials. However, this method is still in its infancy. A number of improvements can be proposed in order to conduct intrinsic properties of organic crystalline materials. To avoid contact with air while transporting freshly prepared samples to the environmental chamber of the AFM, a setup may be taken into consideration to bridge both target points. The clamping technique can be motorized to enable positioning on the micrometer scale instead of the rough manual positioning. This positioning bonus would allow to investigate the organic crystals processed in our group and study the resistivity of semiconductors as a function of distance between tip and wire, while mapping the area of interest. The latter can provide for example the requisite information on grain boundaries discussed previously for p-sexiphenyl on SiO_2 [54]. Tip wearing can also be recovered by sputter-coating the tips with Pd or Au and complementary tip radius characterization can be carried out by scanning electron microscopy to ensure good lateral resolution with the AFM for topographical information.

Acknowledgment

This thesis arouse out of about three years and nine months of research (almost as old as the work group) that for sure weren't enough to reach this level without the contribution of several people whom I would like to thank.

At first, I want to thank my supervisor Prof. Dr. Gregor Witte for offering me a PhD position in his group – molecular solid state physics – or as the members of the group call it: molfk! His ideas were pretty inspiring and he leaves enough room for independent and own initiatives. I also want to thank him for looking over my written work and giving me his feedbacks in no time.

My published work has been realized by collaborations and at this point I want to thank my cooperative partners which include the group of Prof. Dr. Heimbrodt and of Prof. Dr. Parak.

Most of my work have been carried out at the Agilent SPM 5500 and the vacuum chamber "Molly" and I would like to express my thanks to Dr. Matthias Fenner who offered his professional support in any matter concerning the AFM (software and hardware) and Tobias Breuer and his team for keeping "Molly" and siblings well maintained and continuously upgraded which facilitated my experiments, these being in most cases strictly/tightly planned and yet I could manage to get done on time. Thanks are also due to the BESSY crew. Thumbs up!

This acknowledgment is dedicated to our own electronics laboratory and workshop. I could always find a helping hand especially for problems in the electrical measurements with CSAFM and other concerns. I want to thank them for their flexibility and how they are always ready to provide their help: Dr. Matthias Born, Carsten Schindler, and the rest of the team.

I'm grateful to all of the molfk members who contributed to a friendly atmosphere, working enthusiastically and above all baking yummy cakes. Being in a bigger group has its benefits!

I would like to thank Dr. Malek Zerikly (Berlin), Dr. Xia Stammer (Karlsruhe), and Antonia Morherr (good old Marburg) sincerely for revising parts of my thesis in high speed and keeping me motivated.

Thank you, dear girls from my Hockey team in VfL Marburg for keeping me in shape and providing me the necessary balance. Running behind a ball with a stick is fun! The small town Marburg became suddenly interesting (to a certain extend).

Last but not least, I wanna thank my lovely family (Dina + Samer + Georges + Diana) and all my friends for providing me mental support even if it were only by phone and freshen me up with funny stories.

Curriculum Vitae

Personal data Mira El Helou
Afföllerstrasse 21
35039 Marburg

Email: mira.el-helou@gmx.de

Date of birth: May 14^{th} 1983 in Tripoli, Lebanon
single, lebanese

School education

1988–2000	Tripoli Evangelical School for Girls & Boys (T.E.S.)
2000	Lebanese Baccalaureate in experimental sciences

Academic education

2002–2003	Studienkolleg, focus course **T** (branch of technical and mathematical sciences), Studienkolleg des Ökumenischen Studienwerks e.V., Bochum
10/2003–09/2006	Bachelor of Science in Chemistry. Bachelor thesis at Dep. of Phyiscal Chemistry I, Ruhr-University Bochum
10/2006–09/2008	Master of Sceince in Chemistry (specialization in Physical Chemistry). Master thesis at Dep. of Phyiscal Chemistry I, Ruhr-University Bochum
10/2008–04/2012	PhD research at Molecular Solid State Physics, Philipps-University Marburg
08/2012	PhD thesis

Marburg, July 20^{th} 2012

Bibliography

[1] D. M. Alloway, M. Hofmann, D. L. Smith, N. E. Gruhn, A. L. Graham, R. Colorado, V. H. Wysocki, T. R. Lee, P. A. Lee, and N. R. Armstrong, The Journal of Physical Chemistry B **107**, 11690 (2003).

[2] B. N. Pal, J. Sun, B. J. Jung, E. Choi, A. G. Andreou, and H. E. Katz, Advanced Materials **20**, 1023 (2008).

[3] C. Stoll, S. Kudera, W. J. Parak, and F. Lisdat, Small **2**, 741 (2006).

[4] C. Wöll, Progress in Surface Science **82**, 55 (2007).

[5] R. Ruiz, D. Choudhary, T. Nickel, B.and Toccoli, K.-C. Chang, A. C. Mayer, P. Clancy, J. M. Blakely, R. L. Headrick, S. Iannotta, and G. G. Malliaras, Chemistry of Materials **16**, 4497 (2004).

[6] J. Love, L. Estroff, J. Kriebel, R. Nuzzo, and G. Whitesides, Chemical Reviews **105**, 1103 (2005).

[7] H. Yan, S. H. Park, G. Finkelstein, J. H. Reif, and T. H. LaBean, Science **301**, 1882 (2003).

[8] K. Gries, M. E. Helou, G. Witte, S. Agarwal, and A. Greiner, Polymer **53**, 1632 (2012).

[9] D. Käfer, L. Ruppel, and G. Witte, Physical Review B **75**, 085309 (2007).

[10] T. Siegrist, C. Kloc, J. H. Schön, B. Batlogg, R. C. Haddon, S. Berg, and G. A. Thomas, Angewandte Chemie International Edition **40**, 1732 (2001).

[11] R. B. Campbell and J. M. Robertson, Acta Crystallographica **15**, 289 (1962).

[12] S. Schiefer, M. Huth, A. Dobrinevski, and B. Nickel, Journal of the American Chemical Society **129**, 10316 (2007).

[13] I. P. M. Bouchoms, W. A. Schoonveld, J. Vrijmoeth, and T. M. Klapwijk, Synthetic Metals **104**, 175 (1999).

[14] K. Itaka, N. Myojin, M. Yamashiro, J. Yamaguchi, and H. Koinuma, Japanese Journal of Applied Physics **44**, 6249 (2005).

[15] J. Götzen, D. Käfer, C. Wöll, and G. Witte, Physical Review B **81**, 085440 (2010).

[16] H. Dai, E. W. Wong, and C. M. Lieber, Science **272**, 523 (1996).

[17] K. J. Ziegler, B. Polyakov, J. S. Kulkarni, T. A. Crowley, K. M. Ryan, M. A. Morris, D. Erts, and J. D. Holmes, Journal of Materials Chemistry **14**, 585 (2004).

[18] G. Witte, K. Hänel, S. Söhnchen, and C. Wöll, Applied Physics A: Materials Science & Processing **82**, 447 (2006), 10.1007/s00339-005-3367-1.

[19] V. C. Sundar, J. Zaumseil, V. Podzorov, E. Menard, R. L. Willett, T. Someya, M. E. Gershenson, and J. A. Rogers, Science **303**, 1644 (2004).

[20] M. J. Loiacono, E. L. Granstrom, and C. D. Frisbie, The Journal of Physical Chemistry B **102**, 1679 (1998).

[21] M. El Helou, O. Medenbach, and G. Witte, Crystal Growth and Design **10**, 3496 (2010).

[22] J. Götzen and G. Witte, Applied Surface Science (2012), in press (doi:10.1016/j.apsusc.2012.06.094).

[23] S. A. Chevtchenko, J. C. Moore, U. Özgür, X. Gu, A. A. Baski, H. Morkoc, B. Nemeth, and J. E. Nause, Applied Physics Letters **89**, 182111 (2006).

[24] J. C. Moore, S. M. Kenny, C. Baird, H. Morkoc, and A. A. Baski, Journal of Applied Physics **105**, 116102 (2009).

[25] http://www.spmtips.com/.

[26] *Agilent Technologies 5500 Scanning Probe Microscope Users Guide.*

[27] W. Y. Wang, T. Lee, and M. A. Reed, PHYSICAL REVIEW B **68**, 035416 (2003).

[28] M. Porti, M. Avidano, M. Nafria, X. Aymerich, J. Carreras, and B. Garrido, Journal of Applied Physics **98**, 056101 (2005).

[29] P. A. Tipler and R. A. Llewellyn, *Modern Physics* (W. H. Freeman, 3rd edition, 1999).

[30] D. Faltermeier, B. Gompf, M. Dressel, A. K. Tripathi, and J. Pflaum, Physical Review B **74**, 125416 (2006).

[31] D. Käfer, G. Witte, and C. Wöll, Applied Physics A **95**, 273 (2009).

[32] C. Dimitrakopoulos, A. Brown, and A. Pomp, Journal of Applied Physics **80**, 2501 (1996).

[33] U. Heinemeyer, K. Broch, A. Hinderhofer, M. Kytka, R. Scholz, A. Gerlach, and F. Schreiber, Physical Review Letters **104**, 257401 (2010).

[34] A. Hinderhofer, U. Heinemeyer, A. Gerlach, S. Kowarik, R. M. J. Jacobs, Y. Sakamoto, T. Suzuki, and F. Schreiber, Journal of Chemical Physics **127**, 194705 (2007).

[35] O. Ostroverkhova, S. Shcherbyna, D. Cooke, R. Egerton, F. Hegmann, R. Tykwinski, S. Parkin, and J. Anthony, Journal of Applied Physics **98**, 033701 (2005).

[36] R. Hesse, W. Hofberger, and H. Bässler, Chemical Physics **49**, 201 (1980).

[37] M. L. Tiago, J. E. Northrup, and S. G. Louie, Phys. Rev. B **67**, 115212 (2003).

[38] A. S. Davydov, Soviet Physics Uspekhi **7**, 145 (1964).

[39] M. Kasha, H. R. Rawls, and A. M. El-Bayoumi, Pure and Applied Chemistry **11**, 371 (1965).

[40] S. Blumenstengel, H. Glowatzki, S. Sadofev, N. Koch, S. Kowarik, J. Rabe, and F. Henneberger, Physical Chemistry Chemical Physics **12**, 11642 (2010).

[41] M. Li, W. Hebenstreit, U. Diebold, A. M. Tyryshkin, M. K. Bowman, G. G. Dunham, and M. A. Henderson, Journal of Physical Chemistry B **104**, 4944 (2000).

[42] H. Ibach, Physica Status Solidi **33**, 257 (1969).

[43] J. Helzel, S. Jankowski, M. El Helou, G. Witte, and W. Heimbrodt, Applied Physics Letters **99**, 211102 (2011).

[44] K. Hannewald, V. M. Stojanovic, J. M. T. Schellekens, P. Bobbert, G. Kresse, and J. Hafner, Physical Review B **69**, 075211 (2004).

[45] Z. Rang, A. Haraldsson, D. M. Kim, P. P. Ruden, M. I. Nathan, R. J. Chesterfield, and D. Frisbie, Applied Physics Letters **79**, 2731 (2001).

[46] R. G. Nuzzo and D. L. Allara, Journal of the American Chemical Society **105**, 4481 (1983).

[47] A. Ulman, Chemical Reviews **96**, 1533 (1996).

[48] S. W. Joo, S. W. Han, and K. Kim, Journal of Colloid and Interface Science **240**, 391 (2001).

[49] D. Käfer, A. Bashir, and G. Witte, The Journal of Physical Chemistry C **111**, 10546 (2007).

[50] W. Azzam, B. I. Wehner, R. A. Fischer, A. Terfort, and C. Wöll, Langmuir **18**, 7766 (2002).

[51] A. Bashir, D. Käfer, J. Müller, C. Wöll, A. Terfort, and G. Witte, Angewandte Chemie International Edition **47**, 5250 (2008).

[52] P. Cyganik, M. Buck, T. Strunskus, A. Shaporenko, J. D. E. T. Wilton-Ely, M. Zharnikov, and C. Wöll, Journal of the American Chemical Society **128**, 13868 (2006).

[53] Y. Qi, X. S. Liu, B. L. M. Hendriksen, V. Navarro, J. Y. Park, I. Ratera, J. M. Klopp, C. Edder, F. J. Himpsel, J. M. J. Frechet, E. E. Haller, and M. Salmeron, Langmuir **26**, 16522 (2010).

[54] T. W. Kelley, E. Granstrom, and C. D. Frisbie, Advanced Materials **11**, 261 (1999).

Scientific Articles

Temperature dependent optical properties of pentacene films on zinc oxide

J. Helzel,[a] S. Jankowski, M. El Helou, G. Witte, and W. Heimbrodt
Department of Physics and Material Sciences Center, Philipps-University Marburg, Renthof 5, D-35032 Marburg, Germany

(Received 22 August 2011; accepted 3 November 2011; published online 22 November 2011)

The optical transitions of pentacene films deposited on ZnO have been studied by absorption spectroscopy as a function of temperature in the range of room temperature down to 10 K. The pentacene films were prepared with thicknesses of 10 nm, 20 nm, and 100 nm on the ZnO-O(000-1) surface by molecular beam deposition. A unique temperature dependence has been observed for the two Davydov components of the excitons for different film thicknesses. At room temperature, the energetic positions of the respective absorption bands are the same for all films, whereas the positions differ more than 20 meV at 10 K caused by the very different expansion coefficients of pentacene and ZnO. Although the pentacene is just bonded via van der Waals interaction to the ZnO substrate, the very first pentacene monolayer (adlayer) is forced to keep the initial position on the ZnO surface and suffering, therefore, a substantial tensile strain. For all the subsequent pentacene monolayers, the strain is reduced step by step resulting electronically in a strong potential gradient at the interface. © *2011 American Institute of Physics*. [doi:10.1063/1.3663863]

Organic semiconductors have attracted considerable attention because of their versatile electronic properties, low temperature processing, and high mechanical flexibility. These are particularly beneficial for low cost fabrication of electronic and optoelectronic devices as demonstrated by the fabrication of organic light emitting diodes (OLEDs),[1] organic field effect transistors (OFETs),[2] or organic solar cells (OSCs).[3] Recently, also an extension towards organic-inorganic semiconductor hybrid systems has been discussed.[4] The feasibility of this concept has been demonstrated for the case of a $p-n$ junction diode[5] comprising layers of the p-type organic semiconductor pentacene ($C_{22}H_{14}$) deposited onto n-type ZnO substrates. Although device characteristics of this pentacene/ZnO hybrid have been studied in detail, only little is known about the interaction of the two materials and the energy level alignment at the interface. Moreover, previous works reported thickness dependent shifts of the lowest optical transition in pentacene thin films on SiO_2,[6,7] hence reflecting the influence of the molecular environment and ordering near the interface on the resulting optoelectronic properties of the film.

Here, we demonstrate that thickness dependent shifts of the excitonic transitions in crystalline pentacene films on ZnO are mainly caused by strain effects. This is due to different thermal expansion coefficients of the substrate and film although the molecular adlayer is only weakly bonded at the ZnO surface (essentially physisorbed). Using optical absorption spectroscopy to determine the electronic transitions in pentacene films, we observed almost no thickness dependence at room temperature (RT). On the other hand, distinct variations were found at low temperatures that also depend on film thickness. Our explanation of the strain related exciton shifts is corroborated by additional results obtained for pentacene films prepared on various substrates with different expansion coefficients.

[a]Author to whom correspondence should be addressed. Electronic mail: Jonatan.Helzel@physik.uni-marburg.de.

Pentacene (Aldrich, purity >99%) films were grown under ultra-high vacuum conditions by molecular beam deposition at RT with a growth rate of 0.5 nm/min as monitored by a quartz microbalance. Before each film deposition, the oxygen terminated ZnO$(000\bar{1})$ single crystal surfaces (CrysTec) had been cleaned by Ar^+ sputtering and subsequent annealing in oxygen atmosphere. This preparation yields well-ordered surfaces that exhibit a distinct (1×1) low energy electron diffraction pattern and atomically flat terraces of more than 400 nm obtained by atomic force microscopy (AFM, Agilent SPM 5500). X-ray diffraction measurements (Cu-K_α radiation, $\lambda = 1.5406$ Å) showed that the used growth conditions yield (001)-oriented pentacene films adopting exclusively the thin-film crystal phase (cf. Fig. 1(e)).[8] Tapping mode AFM micrographs (see Figs. 1(a) and 1(b)) reveal the presence of characteristic dendritic islands with diameters of few μm which exhibit smooth terraces separated by well-defined steps of about h = 1.5 nm (cf. Fig. 1(d)). This height is in close agreement with the separation of the (001)-planes reflecting the upright orientation of molecules. The molecule-substrate interaction was characterized by thermal desorption spectroscopy measurements. While a characteristic multilayer desorption signal was detected of which peak intensity increases with the film thickness, no further signal due to an interface stabilized monolayer was found. These data, thus, resemble the situation of pentacene on SiO_2 (Ref. 9) and suggest that pentacene is bonded to the ZnO surface essentially via van der Waals interaction.

Optical absorption measurements were carried out in the visible range by using a halogen lamp as light source and an Ocean Optics HR 4000 CG UV-NIR high-resolution grating spectrometer. Fig. 2(a) compares typical absorption spectra that were recorded for pentacene films of different thickness at 10 K and 290 K, respectively. The first absorption bands appearing at 1.86 eV and 1.97 eV at 290 K are assigned to the Davydov-splitted exciton states. Similar spectra have been reported for pentacene layers on SiO_2 also exhibiting

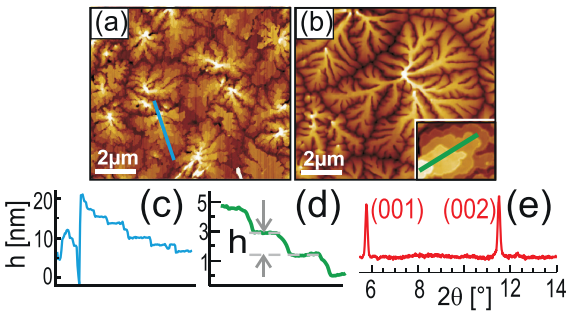

FIG. 1. (Color online) AFM micrographs of pentacene films of various thicknesses on ZnO(000$\bar{1}$): (a) 10 nm (height: 0–15 nm) and (b) 100 nm (height: 0–120 nm) together with corresponding line scans (c) and (d), respectively, and (e) a XRD diffractogram of the thicker film.

the thin-film phase.[10] The following peak at 2.12 eV is related to the HOMO-LUMO bandgap, while the higher energetic maxima have been ascribed earlier to vibronic replica of the bandgap.[11]

The transition dipole moment of the lowest energy excitation of pentacene is oriented along the short axis of the aromatic plane (M-direction).[12] In the crystalline phase, this direction is almost aligned within the (001)-plane, thus yielding a linear polarization for the two Davydov components, E_+ and E_-, along the **a** and **b** directions (as shown schematically in the inset of Fig. 2(c)). In fact, a pronounced polarization dependence was observed in the absorption spectra (cf. Fig. 2(b)) that had been recorded for a single crystalline grain of a 100 nm film by using a 2 μm aperture. As depicted in Fig. 2(c), both Davydov components exhibit an inversely phased intensity variation when rotating the polarization plane.

At RT, all transition energies are almost equal for films of different thicknesses, while they differ considerably at low temperatures. Upon cooling, a red shift has been observed earlier for pentacene films on different substrates (SiO_2, KCl, glass).[10,13] The reduced mean intermolecular distance at low temperatures enhances the molecular transfer integrals and consequently the bandwidths,[14] yielding eventually a reduced bandgap.[15] Our present measurements which are summarized in Fig. 3(a) demonstrate that the direction of the temperature dependent shift also depends on the film thickness. It can be seen that the 100 nm film exhibits the known red shift for both Davydov components, E_+ and E_-, whereas the exciton states of the 10 nm and 20 nm films undergo a distinct blue shift upon cooling. We attribute the latter case to the strain caused by the large difference in the thermal expansion coefficients of the substrate and organic film. The mean thermal expansion coefficients of pentacene can be estimated on the basis of the measured bulk lattice parameters[16] at RT and 20 K to be $\alpha_a = 1.1 \times 10^{-4}$ K^{-1} along ***a***-direction and $\alpha_b = 2.9 \times 10^{-5}$ K^{-1} along ***b***-direction, whereas ZnO exhibits a much smaller value $\alpha_{ZnO} = 3 \times 10^{-6}$ K^{-1}.[17] As a result, the bottom pentacene layers directly attached to the substrate suffer a substantial biaxial tensile strain upon cooling resulting in the blue shift. It is worth noting that the transfer integrals become smaller although the mean molecular distance is slightly smaller than the RT values. This might be a hint for a reduced electron phonon coupling at lower temperatures. With increasing film thickness, however, this strain can relax because of the weak intermolecular interaction in pentacene.

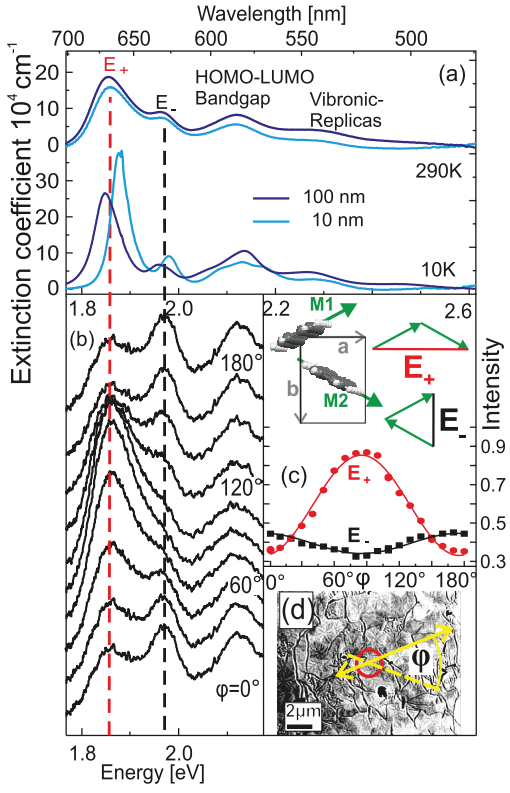

FIG. 2. (Color online) (a) Absorption spectra of 10 nm and 100 nm pentacene thin films on ZnO(000-1) at 290 K and at 10 K each. (b) Absorption spectra of the 100 nm pentacene film at room temperature for linearly polarized light rotated by 20° steps about the normal of the film. (c) Intensity of both Davydov components dependent on the angle of polarization. (d) Microscope picture of the measured region.

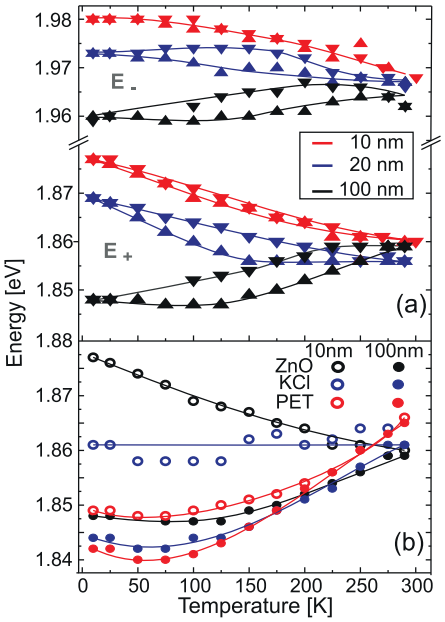

FIG. 3. (Color online) (a) Temperature dependence of the energy of the Davydov splitted exciton states E_+ and E_- obtained for pentacene films of various thickness on ZnO (▽: cooling down, Δ: warming up). (b) Energetic position of the E_+ exciton band as function of temperature (upon cooling) for 10 nm and 100 nm pentacene films on different substrates.

Therefore, most part of the 100 nm film is no longer affected by the interface strain, and the absorption is dominated by a bulk-like temperature dependence of pentacene. Besides the shift, also little changes of the Davydov splitting vs. temperature were found. In case of the 10 nm film, the Davydov splitting reduces upon cooling, while it increases for the 100 nm pentacene film. This might be an indication that the herringbone angle exhibits also a temperature dependence. The Davydov splitting is determined by the interaction energy of both molecules within the unit cell and depends on the herringbone angle as well as on the intermolecular distance.[18]

Moreover, a noticeable hysteresis was observed for the exciton shifts depending on the used temperature profile (cooling down or warming up). This hysteretic behavior is stronger, the thicker the pentacene film. The reason for the hysteresis is most likely the occurrence of little rifts in the films due to the large shrinking upon cooling. When increasing the temperature, the exciton shifts appear delayed and indicate the requirement of an activation energy for healing of rifts and other crystallographic defects. This interpretation is corroborated by a corresponding broadening and narrowing of the absorption band resembling the hysteresis. Such a broadening of the absorption lines (at identical temperature) is a clear indication for a reduced crystallographic perfection.

To prove our explanation of the strain-related exciton shift, analogous measurements were carried out for pentacene films grown on other inert and transparent substrates of different thermal expansion coefficients. These comprise KCl(100), prepared by cleavage of single crystals rods (Korth), and polyethylenterephthalate (PET), cut from an overhead transparency and cleaned by rinsing with ethanol. On both substrates, pentacene forms crystalline films which exhibit the same crystalline phase and orientation as on ZnO. The resulting temperature dependence of the energetic positions of the E_+ exciton state is summarized for films of 100 nm and 10 nm in Fig. 3(b). It is obvious that the difference in the shift of the E_+ band occurring for 10 nm and 100 nm films is much smaller for KCl substrates than for ZnO and almost vanishing in case of PET. This behavior can be clearly related to the smaller difference between the thermal expansion coefficients of pentacene and the KCl (Ref. 19) and PET (Ref. 20) substrates ($\alpha_{KCl} = 4 \times 10^{-5}$ K^{-1}, $\alpha_{PET} = 5 - 6 \times 10^{-5}$ K^{-1}).

In summary, we have shown that the substrate of an organic-inorganic hybrid can have a strong influence on the energy states of the organic film even if the molecular adlayer is weakly bonded to the substrate. Temperature changes, as usually present in operating device structures, can affect the positions of the energetic levels in the molecular film. The resulting different strain states of the monolayers adjacent to the substrate compared to the more remote monolayers even in case of initially strain free organic layers on inorganic substrates may produce strong interface potentials acting either as Ohmic or Schottky potentials for a charge transfer across the interface. Since organic layers used in device applications are rather thin, those interface potentials have to be studied thoroughly and must be taken into account.

[1]J. Shinar and R. Shinar, J. Phys. D **41**, 133001 (2008).
[2]A. Facchetti, Mater. Today **10**, 28 (2007).
[3]B. Rand, J. Genoe, P. Heremans, and J. Poortmans, Prog. Photovoltaics **15**, 659 (2007).
[4]P. Ong and I. Levitsky, Energies **3**, 313 (2010).
[5]B. N. Pal, P. Trottman, J. Sun, and H. E. Katz, Adv. Mater. **20**, 1023 (2008).
[6]U. Heinemeyer, K. Broch, A. Hinderhofer, M. Kytka, R. Scholz, A. Gerlach, and F. Schreiber, Phys. Rev. Lett. **104**, 257401 (2010).
[7]R. He, N. G. Tassi, G. B. Blanchet, and A. Pinczuk, Appl. Phys. Lett. **96**, 263303 (2010).
[8]S. Schiefer, M. Huth, A. Dobrinevski, and B. Nickel, J. Am. Chem. Soc. **129**, 10316 (2007).
[9]D. Käfer, C. Wöll, and G. Witte, Appl. Phys. A **95**, 273 (2009).
[10]D. Faltermeier, B. Gompf, M. Dressel, A. K. Tripathi, and J. Pflaum, Phys. Rev. B **74**, 125416 (2006).
[11]A. Hinderhofer, U. Heinemeyer, A. Gerlach, S. Kowarik, R. M. J. Jacobs, Y. Sakamoto, T. Suzuki, and F. Schreiber, J. Chem. Phys. **127**, 194705 (2007).
[12]M. L. Tiago, J. E. Northrup, and S. G. Louie, Phys. Rev. B **67**, 115212 (2003).
[13]O. Ostroverkhova, S. Shcherbyna, D. G. Cooke, R. F. Egerton, F. A. Hegmann, R. R. Tykwinski, S. R. Parkin, and J. E. Anthony, J. Appl. Phys. **98**, 033701 (2005).
[14]K. Hannewald, V. M. Stojanovic, J. M. T. Schellekens, P. Bobbert, G. Kresse, and J. Hafner, Phys. Rev. B **69**, 075211 (2004).
[15]Z. Rang, A. Haraldsson, D. M. Kim, P. P. Ruden, M. I. Nathan, R. J. Chesterfield, and D. Frisbie, Appl. Phys. Lett. **79**, 2731 (2001).
[16]R. Eiermann, G. M. Parkinson, H. Baessler, and J. M. Thomas, J. Phys. Chem. **87**, 544 (1983).
[17]S. Adachi, Semicond. Sci. Technol. **19**, 276 (2004).
[18]M. Kasha, H. Rawls, and A. El-Bayoumi, Pure Appl. Chem. **11**, 371 (1965).
[19]R. E. Glover, Z. Phys. **138**, 222 (1954).
[20]D. N. Bikiaris and G. P. Karayannidis, J. Appl. Polym. Sci. **60**, 55 (1996).

submitted to J. Phys. Cond. Mat.

Structural and Optical Properties of Pentacene Films grown on differently oriented ZnO Surfaces

M. El Helou, E. Lietke, J. Helzel, W. Heimbrodt, and G. Witte[a)]
Philipps-University Marburg, Department of Physics and Material Sciences Center, Renthof 7, D-35032 Marburg, Germany

(Dated: 13 June 2012)

Pentacene films have been grown on the two polar zinc oxide surfaces, i.e., ZnO(0001) and ZnO(000$\bar{1}$), as well as on the mixed-terminated ZnO(10$\bar{1}$0) and are characterized by means of atomic force microscopy (AFM), X-ray diffraction (XRD), and thermal desorption spectroscopy (TDS). In all cases, pentacene aggregates in an upright orientation without any evidence for the formation of an interface stabilized wetting layer. Additional films deposited on a highly-defective, oxygen-depleted ZnO(000$\bar{1}$) reveal no altered growth mode. Nearly identical optical absorption spectra have been measured for all films, thus, corroborating a weak molecule-substrate interaction. Upon cooling, however, a slightly different relaxation behavior could be resolved for pentacene films on polar ZnO surfaces compared to pentacene on the mixed-terminated ZnO(10$\bar{1}$0) surface.

Keywords: organic/inorganic interface, TDS, AFM, pentacene, polar and non-polar zinc oxide

I. INTRODUCTION

Organic-inorganic semiconductor hybrid systems are receiving increasing attraction because they offer the notable advantage of combining a large structural and optoelectronic variability of molecular materials with high charge carrier mobility of inorganic semiconductors. Among inorganic materials, metal oxide substrates like ZnO or TiO_2 are of particular interest because their large optical band gap enables a usage as transparent substrates. Such hybrid systems are key components of dye-sensitized solar cells[1] and have also been utilized on the basis of ZnO in combination with the *p*-type organic semiconductor pentacene (PEN, $C_{22}H_{14}$) for the fabrication of $p-n$ junction diodes[2] or semi-transparent photo-detectors[3]. Despite a successful demonstration of first device applications, so far little is known about the interaction at the interface between conjugated aromatic molecules and ZnO. On the other hand, this oxide is widely used as support in heterogeneous catalysis[4] and quite different chemical reactivity is found for small molecules adsorbed on the different surfaces of ZnO nanoparticles[5].

Recently, a remarkable orientation dependence has been observed for the growth of *para*-sexiphenyl on the different surfaces of ZnO: while terraced islands with upright oriented molecules are formed on the polar ZnO(0001) surface, a needle-shaped aggregation with recumbent orientation occurs on the mixed-terminated ZnO(10$\bar{1}$0) surface[6]. Since optical excitations of molecules are rather anisotropic according to their shape anisotropy, the possibility to control molecular orientations in crystalline films by choosing appropriate substrate surfaces allows to adjust effectively the optical properties of molecular films. In order to address the question about the universality of this approach, we have systematically analyzed the formation and structure of PEN films on the various ZnO surfaces. In a previous study, we found that PEN is only weakly adsorbed on the oxygen-terminated polar ZnO(000$\bar{1}$) surface but reveal a distinct temperature-dependent shift of the excitonic excitations due to a thermally induced lattice strain caused by the different thermal expansions of molecular adlayer and inorganic substrate[7]. Here, we present a systematical extension of such investigations also to the Zn-terminated as well as the mixed-terminated surface of ZnO. By combining atomic force microscopy (AFM), X-ray diffraction (XRD) and thermal desorption spectroscopy (TDS), the structure and molecule-substrate interaction were examined. Optical absorption spectroscopy was employed as well in order to characterize the optical properties of the various films and their temperature dependence. Due to the fact that structural defects in substrate surface were found to severly affect the resulting molecular film structure[8,9] - bearing in mind that metal oxide surfaces might be easily modified by reduction during preparation under ultra-high vacuum (UHV) conditions[10]-, we have additionally studied PEN films deposited onto defective ZnO surfaces prepared by extensive vacuum heating.

II. EXPERIMENTAL

In the present experiments, hydrothermally grown ZnO single crystals (CrysTec GmbH) were used which had been oriented and epi-polished (roughness: rms $<0.5\,\mathrm{nm}$) to better than $0.3\,^\circ$ of the desired orientation. Different crystal orientations were examined comprising the polar ZnO(000$\bar{1}$) and ZnO(0001) surfaces as well as the mixed-terminated ZnO(10$\bar{1}$0) surface. Throughout this paper, we denote the oxygen-terminated ZnO(000$\bar{1}$) surface as ZnO-O and the zinc-terminated ZnO(0001)

a)corr. author:gregor.witte@physik.uni-marburg.de

surface as ZnO-Zn. All oxide crystals were prepared by Ar^+-ion sputtering (800 eV) followed by annealing at 1200 K (60 min) in a quartz tube of a furnace (Heraeus) in ambient atmosphere before passing the samples into the UHV apparatus for film deposition. This preparation avoids an oxygen depletion that occurs upon extensive heating in vacuum and yields highly ordered surfaces exhibiting sharp (1×1) low energy electron diffraction patterns and atomically flat terraces extending over more than 500 nm separated by monatomic steps as demonstrated in a previous study[11]. Supplementary measurements were carried on oxygen-depleted ZnO-O surface that was heated at 1350 K after nominal sample preparation in UHV and is denoted as ZnO-O(depl.). Sublimation-cleaned pentacene (PEN, Aldrich, purity >99%) was deposited under UHV conditions from a resistively heated Knudsen cell onto freshly prepared ZnO crystals held at room temperature (RT). All films were grown with a constant deposition rate of 3 Å/min which was monitored by a quartz crystal microbalance. Adsorption energy and thermal stability of PEN films were characterized on the various substrate surfaces by thermal desorption spectroscopy (TDS). TDS measurements were carried out employing a quadrupole mass spectrometer (QMS, Balzer QMA 200) with a Feulner cup positioned close to the sample surfce. TD spectra were acquired by recording the mass signal of the single-charged molecule ion (m/z=278 amu) during a computer-controlled linear increase (β =0.5 K/s) of the sample temperature measured by a K-type thermocouple attached onto the sample surface. The substrate and PEN film morphology were characterized by atomic force microscopy (AFM, Agilent SPM 5500) operated in tapping mode under ambient conditions. $\theta/2\theta$ measurements were used to determine the crystallographic phases and orientations of the molecular films. These data were obtained from an X-ray diffractometer (PANalytical, X'Pert-PRO) operated in Bragg-Brentano geometry using Co K_α radiation (λ=1.7903 Å). Optical absorption measurements were executed in the visible range by using a halogen lamp as light source and an Ocean Optics HR 4000 CG UV-NIR high-resolution grating spectrometer. Using a helium cryostat, these measurements were performed at variable temperatures down to 10 K.

III. RESULTS AND DISCUSSION

Figure 1 shows a compilation of AFM data comparing the morphology of PEN films grown with a nominal thickness of 10 nm at RT onto differently oriented ZnO crystals. PEN films exhibit dendritic islands on the Zn-terminated basal plane (ZnO-Zn) as well as on the mixed-terminated ZnO($10\bar{1}0$) surface. These data resemble the growth of PEN on ZnO-O as reported by Helzel *et al.*[7]. Only the diameter of the molecular islands is different ranging from of 2-3 μm on ZnO-O to less than 0.5 μm on ZnO-Zn. The line profiles that are taken from the magnified micrographs (cf. Fig. 1) yield a distinct step height of 1.6 nm for all corresponding substrates. This height is in line with an upright orientation of the molecules. For the growth of *para*-sexiphenyl on various ZnO surfaces, a distinct variation regarding the height and, thus, the orientation was found. This oligophenylene exhibits upright standing molecules on the polar surfaces while a recumbent orientation is adopted on the ZnO($10\bar{1}0$) surface[6]. This is not the case for PEN, hence indicating a different behavior of acenes and oligophenylenes on ZnO single crystals.

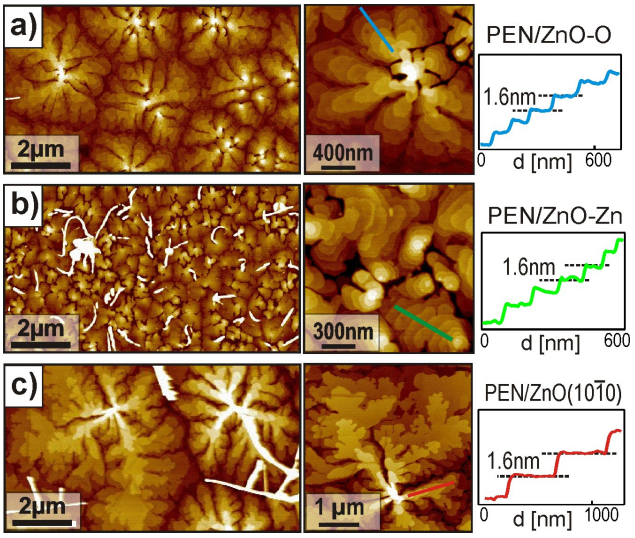

FIG. 1. Comparison of AFM data showing the morphology of 10 nm PEN films grown onto a) ZnO-O, b) ZnO-Zn, and c) ZnO($10\bar{1}0$). The line profiles taken from the magnified micrographs yield a step height which indicates an upright orientation of the molecules on all ZnO surfaces.

Pentacene thin films are known to crystallize on inert substrates either in the *thin-film* (TF) phase[12] or the *Campbell* (C) phase[13]. The polymorphs are characterized by slightly different (001)-interlayer spacings of 15.4 Å (TF-phase) and 14.4 Å (C-phase), respectively. Though the present AFM data clearly indicate an upright molecular orientation as reported earlier for PEN films on SiO_2[14], they do not allow to distinguish which crystalline phase is adopted. Therefore, XRD measurements were performed for PEN films grown on the three different ZnO surfaces. To attain sufficient scattering intensity, these measurements were carried out on PEN films with a nominal thickness of 35 nm. The simultaneously measured substrate reflexes [(002) peak at $2\theta = 40.78°$ for the basal plane and (100) peak at $2\theta = 36.70°$ for ZnO($10\bar{1}0$)] were used to verify the sample alignment and compensate a possible angular offset of the diffractometer. As shown in Fig. 2, the corresponding $\theta/2\theta$-scans reveal two distinct peaks at 6.7° and 13.4° for all samples. These patterns are compared to the expected peak positions calculated from the powder spectra of the TF- and C-phase of PEN (black and grey dashed lines in Fig.

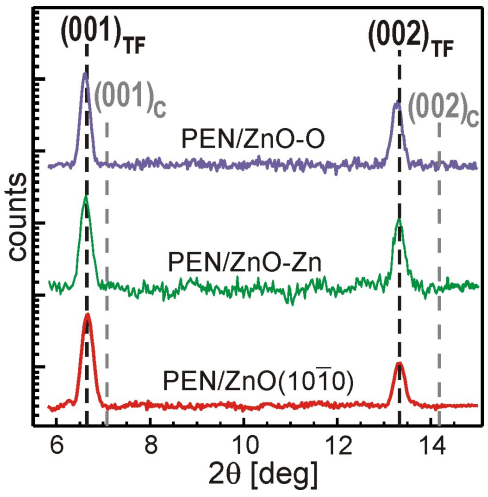

FIG. 2. $\theta/2\theta$-scans of 35 nm PEN films grown on the differently oriented ZnO surfaces. The given scattering intensity after background subtraction is plotted in a logarithmic scale. The dashed lines indicate the expected peak positions calculated from the powder spectra of the *thin-film* phase (denoted as TF) and Campbell phase (C) of PEN.

2). The observed peaks are clearly assigned to (001) and (002) reflexes of the *thin-film* phase. We note that no further pentacene diffraction reflexes were observed at larger scattering angles. Therefore, we exclude any coexisting phases with smaller interlayer spacing i.e. recumbent molecular orientation.

Note that formation of (001)-oriented PEN films have been observed for many substrates where molecules at the interface, i.e. the wetting layer, may adopt a different orientation. For example, PEN molecules chemisorb flat lying in the very first layer on Cu(110) and Cu(221) surfaces. However, this motif is not preserved upon further growth where instead an upright molecular orientation is adopted in thicker films[15,16]. Therefore, complementary AFM measurements were carried for a submonolayer with a nominal film thickness 0.3 nm in order to characterize the initial stage of film growth. We have chosen the non-polar ZnO(10$\bar{1}$0) surface since the uniaxial surface structure may introduce an alignment of molecules as it was observed for the case of sexiphenyl[6] or PEN monolayer on rutile TiO_2(110)[17]. The AFM micrograph shown in Fig. 3 reveals the presence of distinct islands with a height of about 1.6 nm as well as 3.2 nm corresponding to mono- and bi-molecular layer, respectively. It clearly demonstrates that molecules grow in an upright orientation already in the very first layer on this surface as on SiO_2[18]. In contrast, quite different molecular orientations were found for sexiphenyl on the different surfaces of ZnO (upright standing on ZnO(0001) vs. flat-lying on ZnO(10$\bar{1}$0)[6]). Recently, this situation has been explained by a theoretical analysis. It was found that the alignment of the molecules with their long molecular axis perpendicular to the polar [0001] azimuth direction of the mixed-

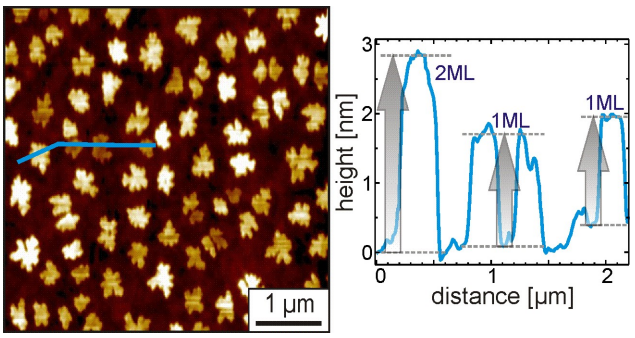

FIG. 3. AFM micrograph of PEN submonolayer (nominal thickness 0.3 nm) deposited on ZnO(10$\bar{1}$0) showing the initial stage of film growth. It demonstrates the upright molecular orientation from the first layer on. The majority of islands have a height of about 1.6 nm and a few possess two molecular layers in height (h=3.2 nm).

terminated ZnO surface is electrostatically stabilized[19] despite the overall weak interaction of sexiphenyl with the ZnO substrate (essentially physisorption). Moreover, the corresponding calculations for the adsorption of PEN on the ZnO(10$\bar{1}$0) did not reveal such an azimuthal dependent stabilization. This finding suggests that the film growth is rather dominated by the intermolecular interaction in the absence of any preferential pre-alignment favoring an upright adsorption geometry as the case on SiO_2.

Complementary information on the strength of the molecule-substrate interaction are derived from thermal desorption data that were collected for PEN films grown on the various ZnO surfaces. TD spectra were recorded for submonolayer PEN films with a nominal thickness of 0.3 nm in order to enhance the interface sensitivity of these measurements and to suppress intense signals arising from multilayer desorption. As displayed in Fig. 4, each TD spectrum exhibits only one distinct desorption peak around 380 K while no further signal could be detected at higher temperatures, neither at the mass of the molecule ion nor for any fragment. We note that an appearance of desorption signals at similar temperatures were observed before for PEN multilayer films on quite different substrates such as copper[15], gold[20], silver[21], SiO_2[20], or graphite[22]. Further analysis by TDS was carried out for PEN films of different thicknesses ranging from 0.2 to 1.8 nm (cf. inset in Fig. 4). Thickness dependence allows to conclude the nature of the desorption signal. The intensity of desorption peaks increases with film thickness while their onset stays constant for all cases. Moreover, the ascending peak flank remains nearly unchanged for the different coverages, hence, indicating multilayer desorption which can be well described by zero-order kinetics[20]. Note that this desorption kinetics is marked by the fact that the apparent peak maximum increases slightly with the film thickness, i.e., higher temperatures are expected for desorption of thicker layers. At higher temperature, a more firmly bound monolayer

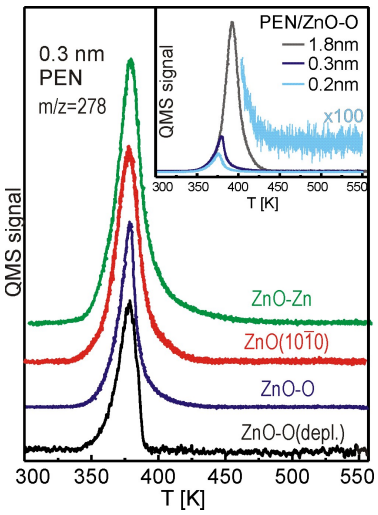

FIG. 4. Series of thermal desorption spectra obtained for 0.3 nm PEN films grown on various ZnO crystal surfaces. The spectra were recorded at the mass of the molecule ion (m/z=278 amu) by applying a heating ramp of β=0.5 K/s. The inset shows an increasing desorption signal with the actual film thickness which can be identified as multilayer desorption following a zero-order desorption kinetics. As demonstrated by the magnified spectrum, no evidence for any firmly bound monolayer is found.

was recorded for PEN on metals[15,20,21] or for smaller acenes adsorbed on TiO_2[23]. In the present case, the absence of any additional desorption peak as well as an appearance of multilayer desorption even at submonolayer coverages demonstrate that PEN-ZnO interaction is actually weaker than the mutual interaction which stabilizes the van der Waals bound organic multilayers. A similar situation was observed before for PEN films on SiO_2[20] or graphite[22] and indicates that the initially formed submonolayer islands actually pile up during the heating process and finally desorp as small multilayer islands. This is also corroborated by the appearance of bilayer islands observed in the AFM data of submonolayer films (cf. Fig. 3).

Previous studies have shown that electronic and chemical properties of differently oriented ZnO surfaces can be quite diverse[4,24,25]. For example, small molecules such as CO or pyridine experience rather unequal adsorption energies on various ZnO surfaces[4]. By contrast, the present TDS data reveal no evidence for any dependency of pentacene-ZnO interaction on the substrate orientation. This is consistent with a weak, essentially van der Waals type interaction, which is expected to be independent from specific electronic properties (e.g. band structure) of the actual surface. Beyond that, it has been shown that surface chemistry and reactivity of ZnO substrates are considerably affected by pre-adsorption of hydrogen[4]. Similar effects have been observed also for metals (e.g. ruthenium) and silicon surfaces where hydrogen adlayers cause an effective passivation which in turn reduces the damping of molecular vibrations[26] and modifies the subsequent growth of pentacene films[27]. In case of ZnO, it was found that heating samples to 650 K results in a hydrogen free surface[28,29]. To address the issue, whether the observed pentacene-ZnO interaction is actually governed by hydrogen adlayers, additional TDS measurements were carried out. A potential hydrogen uptake could be avoided or at least largely suppressed by flash heating the samples to 650 K in the UHV chamber and quickly cooling down to RT (within less than 10 min) before depositing the pentacene films. Subsequently recorded TD spectra were identical to those obtained without flash heating and revealed no evidence for any more firmly bound monolayer, hence, indicating that pentacene is in fact weakly adsorbed on bare ZnO surfaces.

A specific characteristic of metal oxides is the critical dependency of their surface morphology and stoichiometry on the actual sample preparation. Especially, extensive heating under UHV conditions may cause a partial oxygen depletion leading to gradual metallization of the surfaces as for rutile TiO_2(110) single crystal[10]. Using scanning tuneling microscopy (STM), it was shown that low-indexed ZnO surfaces exhibit an increasing roughness upon annealing the crystals beyond 1023 K in vacuum[30]. Therefore, we have also examined an oxygen depletion and its influence on related surface roughness. The latter may play a major role in the subsequent pentacene film growth and in molecule-substrate interaction. For this purpose, additional PEN films were grown onto ZnO-O substrates which had been heated at 1350 K in UHV for 30 min before film deposition (denoted as ZnO-O(depl.)). Corresponding AFM data of ZnO(depl.) indeed reveal an increased surface roughness and formation of characteristic pores (cf. Fig. 5). As shown for comparison in Fig. 5a and 5c, the ideal surface prepared by heating in air exhibits atomically smooth terraces extending over several hundred nanometers and are separated by steps with a height of d=2.6 Å which equals the $d_{(0001)}$-interlayer spacing (c/2). By contrast, the surface of the vacuum annealed sample exhibits a high density of depressions with diameters of about 20-30 nm and a depth corresponding to multiple interlayer distances (cf. line scan II in Fig. 5b and 5c). Interestingly, the AFM data of a 10 nm PEN film deposited onto such a vacuum heated ZnO-O surface (without exposing it to air) again reveal dendritic islands consisting of upright standing molecular layers as depicted in Fig. 5d. Compared to PEN films grown on the ideal surface, the diameters of the dendritic islands are, however, largely reduced and amount to less than 0.5 μm. Also the corresponding TDS data (lowermost spectrum in Fig. 4) reveal no noticeable influence on the molecule-substrate interaction for such defective surface and, in particular, no evidence for a stabilized monolayer. These findings indicate that the upright oriented growth of PEN appears to be largely unaffected by surface point defects. A similar behavior was found upon growth of pentacene on rough gold or graphite substrates

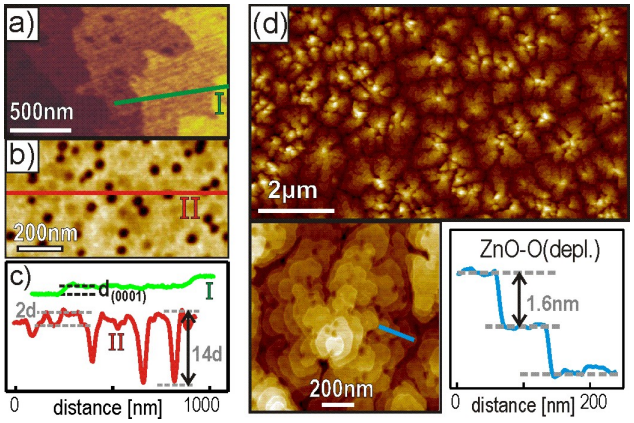

FIG. 5. Summary of AFM data showing the PEN film growth onto vacuum heated ZnO-O, i.e., ZnO-O(depl.) surface. Comparison of a) an ideally prepared ZnO-O surface with b) an extensive vacuum heated surface and c) coresponding line profiles showing the formation of characteristic depressions. d) Deposition of PEN films (thickness 10 nm) on ZnO-O(depl.) again yields dendritic islands consisting of upright oriented molecule layers.

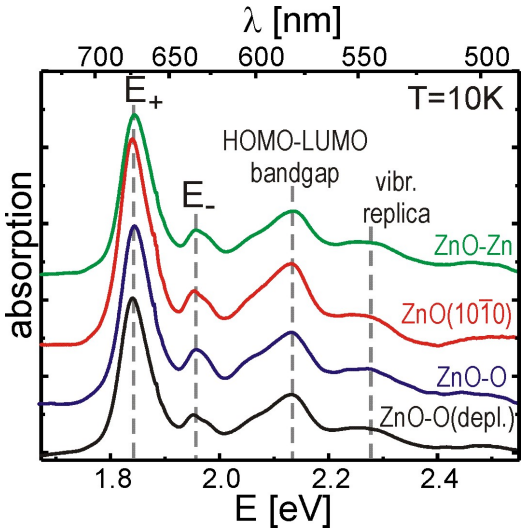

FIG. 6. Comparison of optical absorption spectra of 35 nm PEN films grown on differently terminated ZnO surfaces at 10 K.

with high defect density. In the latter case, molecules grow in an upright fashion while they adopt a recumbent orientation on the respective smooth surfaces[22,31].

Finally, optical absorption spectroscopy was employed to examine whether the various ZnO surfaces (i.e. different orientation and roughness) have any influence on the optoelectronic excitations within the PEN films. These experiments extend our previous work carried out for PEN films grown on the ZnO-O surface[7]. There, we have shown on the basis of temperature measurements that the ZnO substrate can have a notable influence on the energy states of the organic film even if the molecular

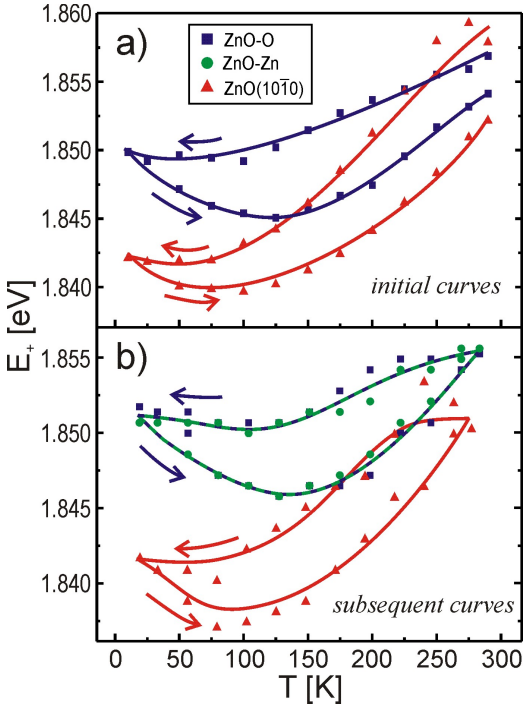

FIG. 7. Temperature dependence of the peak position of the excitonic E_+ Davydov component for pentacene films on different ZnO surfaces upon cooling down and warming up between RT and 10K. (a) Initial curves revealing a relaxation of the films. (b) Closed hysteresis loops, typical for subsequent measurements to the initial curves.

adlayer is only weakly bonded to the substrate.

In order to obtain distinct spectral signatures, films with a thickness of 35 nm were used and the measurements were carried out at variable temperatures ranging from RT down to 10 K. As depicted in Fig. 6, all absorption spectra acquired for the various ZnO surfaces at 10 K are almost identical and reveal distinct peaks at about 1.85 eV, 1.97 eV, and 2.12 eV as well as a broader feature at 2.28 eV in each case. Based on azimuthal resolved polarization measurements with normal incidence of the light[7], the first two absorption peaks have been clearly identified as the two Davydov components of the exciton state in crystalline pentacene films (denoted as E_+ and E_-) while the peaks at higher energies correspond to HOMO-LUMO bandgap transition and vibronic replica of this excitation. The optical excitations in molecular films depend essentially on the orientation of the transition dipole moments which is given by the molecular orientation. Thus the almost identical spectral signature of the various pentacene layers clearly corroborates the afore mentioned result that the molecules adopt a uniform molecular orientation on the various ZnO surfaces. Though the E_+ peak exhibits a FWHM of about 60 meV, its maximum position could be determined with an accuracy of about ±2 meV by careful peak analysis which enabled a detailed investigation of temperature effects.

Fig. 7a depicts the peak positions of the E_+ component as a function of temperature for PEN films grown on the ZnO-O and ZnO($10\bar{1}0$) surfaces during the first cooling-down cycle (denoted as "initial curve"). At RT, at which the PEN films have been grown, the E_+ peak positions are initially equal within the experimental error for both substrates and reveal a small but distinct red shift upon cooling. The reduced exciton energy at lower temperatures can be related to the reduced intermolecular distances caused by the large thermal expansion coefficient of PEN (estimated to be $\alpha_a = 1.1 \times 10^{-4}\,\mathrm{K}^{-1}$ along ***a***-direction and $\alpha_b = 2.9 \times 10^{-5}\,\mathrm{K}^{-1}$ along ***b***-direction from measured bulk lattice parameters at RT and 20 K[32]). This enhances the molecular transfer integrals and consequently the bandwidths, eventually resulting in a reduced bandgap[33,34]. Though a subsequent warming up yields a blue shift of the E_+ transition as can be seen in Fig. 7a, two results are noteworthy: (i) the remaining peak positions are red shifted after reaching the RT again for both layers compared to the as-grown transition and (ii) the red shift upon cooling down and the remaining, irreversible red shift at RT is stronger in case of the mixed-terminated ZnO surface. By contrast to the initial curve, closed hysteresis loops were observed for the E_+ peak position upon subsequent cooling-down and warming-up cycles as depicted in Fig. 7b for PEN films grown on the Zn- (green dots) and O- (blue squares) terminated ZnO surfaces (so called c-plane) as well as for a mixed-terminated ZnO surface (a-plane, red triangles). For all following mesurements, the results are found to be reproducible to the subsequent curves. Like for the initial curve, the largest temperature effect was found for PEN films on ZnO($10\bar{1}0$) surface and the temperature curves for the two polar surfaces (Zn- and O-terminated) are identical. In our prvious study, we discussed already possible reasons for the observed shifts for a given surface as a function of temperature[7]. Due to the fact that the thermal expansion coefficient of pentacene is more than one order of magnitude larger than that of ZnO, the molecular layers suffer strain upon cooling resulting from a large tensile strain at the interface. Approaching a critical value, a relaxation of the PEN layers by slightly gliding at the interface should get possible. This hypothesis is confirmed by our previous finding that the hysteretic behavior is stronger, the thicker the pentacene film[7], which was attributed to the occurrence of little rifts in the films due to the large shrinking upon cooling on the one hand. On the other hand, when increasing the temperature, the exciton shifts appears delayed and indicate the requirement of an activation energy for healing of rifts and other crystallographic defects. This interpretation was further corroborated by a corresponding broadening and narrowing of the absorption band resembling the hysteresis[7]. A broader absorption band at a given temperature is a clear indication for a reduced crystallographic perfection.

In our previous study, we have further demonstrated that the magnitude of the thermal induced exciton peak shift strongly depends on the thermal expansion coefficients of the used substrate[7] which suggests thermomechanical differences for the various ZnO surfaces. In fact, ZnO has rather anisotropic thermal expansion coefficients with $\alpha_\perp$ (perpendicular to c-axis) being almost twice as large as $\alpha_\parallel$ (parallel to c-axis)[35]. Therefore, the difference in thermal expansion between PEN and ZnO is expected to be largest for the mixed terminated ZnO surface (i.e. a-plane). Finally, we note that the temperature dependent exciton energy curves of PEN films on all ZnO substrates (cf. Fig. 7) exhibit a shallow but visible minimum around 80-120 K. Interestingly, the thermal expansion coefficients of ZnO at this temperature reveal a change in sign yielding the largest density around 100 K which is likely to cause the minimum in the temperature dependent exciton curves.

IV. SUMMARY

The present study shows that growth of pentacene on crystalline ZnO substrates proceeds in the formation of (001)-oriented films consisting of dendritic islands adopting the crystalline *thin-film* phase. An upright molecular orientation occurs irrespective of the actual surface orientation being either polar or mixed-terminated ZnO. In contrast to an induced orientational control of sexiphenyl films[6], no additional stabilization could be observed for PEN on any ZnO surface. Moreover, it was found that defective surface created by extensive heating in vacuum do not affect the resulting organic film structure and only slightly reduce the crystallite size while optical absorption spectra of the molecular films are essentially unaffected. Only a slightly different relaxation behavior upon cooling was observed for pentacene films on polar ZnO surfaces compared to pentacene on the mixed-terminated ZnO($10\bar{1}0$). The growth mode of pentacene which results from a weak substrate interaction appears to be rather robust which is advantageously for the fabrication of organic-inorganic semiconductor hybrid systems based on polycrystalline ZnO substrates[2].

[1] A. Hagfeldt and M. Grätzel, Accounts of Chemical Research **33**, 269 (2000).
[2] B. N. Pal, J. Sun, B. J. Jung, E. Choi, A. G. Andreou, and H. E. Katz, Advanced Materials **20**, 1023 (2008).
[3] K. H. Lee, H. S. Lee, K. Lee, T. Ha, J. H. Kim, and S. Im, Advanced Materials **23**, 1231 (2011).
[4] C. Wöll, Progress in Surface Science **82**, 55 (2007).
[5] J. Strunk, K. Kähler, X. Xia, and M. Muhler, Surface Science **603**, 1776 (2009).
[6] S. Blumenstengel, H. Glowatzki, S. Sadofev, N. Koch, S. Kowarik, J. Rabe, and F. Henneberger, Physical Chemistry Chemical Physics **12**, 11642 (2010).
[7] J. Helzel, S. Jankowski, M. El Helou, G. Witte, and W. Heimbrodt, Applied Physics Letters **99**, 211102 (2011).
[8] J. Ivanco, T. Haber, J. Krenn, F. Netzer, R. Resel, and M. Ramsey, Surface Science **601**, 178 (2007).
[9] T. Breuer, I. Salzmann, J. Götzen, M. Oehzelt, A. Morherr, N. Koch, and G. Witte, Crystal Growth & Design **11**, 4996 (2011).

[10]M. Li, W. Hebenstreit, U. Diebold, A. M. Tyryshkin, M. K. Bowman, G. G. Dunham, and M. A. Henderson, Journal of Physical Chemistry B **104**, 4944 (2000).
[11]J. Götzen and G. Witte, Applied Surface Science (2012), submitted.
[12]S. Schiefer, M. Huth, A. Dobrinevski, and B. Nickel, Journal of the American Chemical Society **129**, 10316 (2007).
[13]R. B. Campbell and J. M. Robertson, Acta Crystallographica **15**, 289 (1962).
[14]C. Dimitrakopoulos, A. Brown, and A. Pomp, Journal of Applied Physics **80**, 2501 (1996).
[15]S. Söhnchen, S. Lukas, and G. Witte, Journal of Chemical Physics **121**, 525 (2004).
[16]J. Götzen, S. Lukas, A. Birkner, and G. Witte, Surface Science **605**, 577 (2011).
[17]V. Lanzilotto, C. Sanchez-Sanchez, G. Bavdek, D. Cvetko, M. F. Lopez, J. A. Martin-Gago, and L. Floreano, Journal of Physical Chemistry C **115**, 4664 (2011).
[18]R. Ruiz, D. Choudhary, T. Nickel, B.and Toccoli, K.-C. Chang, A. C. Mayer, P. Clancy, J. M. Blakely, R. L. Headrick, S. Iannotta, and G. G. Malliaras, Chemistry of Materials **16**, 4497 (2004).
[19]F. Della Sala, S. Blumenstengel, and F. Henneberger, Physical Review Letters **107**, 146401 (2011).
[20]D. Käfer, G. Witte, and C. Wöll, Applied Physics A **95**, 273 (2009).
[21]D. Käfer and G. Witte, Chemical Physics Letters **442**, 376 (2007).
[22]J. Götzen, D. Käfer, C. Wöll, and G. Witte, Physical Review B **81**, 085440 (2010).
[23]S. Reiss, H. Krumm, A. Niklewski, V. Staemmler, and C. Wöll, Journal of Chemical Physics **116**, 7704 (2002).
[24]J. C. Moore, S. M. Kenny, C. Baird, H. Morkoc, and A. A. Baski, Journal of Applied Physics **105**, 116102 (2009).
[25]S. A. Chevtchenko, J. C. Moore, U. Özgür, X. Gu, A. A. Baski, H. Morkoc, B. Nemeth, and J. E. Nause, Applied Physics Letters **89**, 182111 (2006).
[26]G. Witte, K. Weiss, P. Jakob, J. Braun, K. L. Kostov, and C. Wöll, Physical Review Letters **80**, 121 (1998).
[27]T. Shimada, H. Nogawa, T. Hasegawa, R. Okada, H. Ichikawa, K. Ueno, and K. Saiki, Applied Physics Letters **87**, 061917 (2005).
[28]Y. Wang, B. Meyer, X. Yin, M. Kunat, D. Langenberg, F. Traeger, A. Birkner, and C. Wöll, Physical Review Letters **95**, 266104 (2005).
[29]J. Lahiri, S. Senanayake, and M. Batzill, Physical Review B **78**, 155414 (2008).
[30]U. Diebold, L. V. Koplitz, and O. Dulub, Applied Surface Science **237**, 336 (2004).
[31]D. Käfer, L. Ruppel, and G. Witte, Physical Review B **75**, 085309 (2007).
[32]R. Eiermann, G. M. Parkinson, H. Baessler, and J. M. Thomas, The Journal of Physical Chemistry **87**, 544 (1983).
[33]K. Hannewald, V. M. Stojanovic, J. M. T. Schellekens, P. Bobbert, G. Kresse, and J. Hafner, Physical Review B **69**, 075211 (2004).
[34]Z. Rang, A. Haraldsson, D. M. Kim, P. P. Ruden, M. I. Nathan, R. J. Chesterfield, and D. Frisbie, Applied Physics Letters **79**, 2731 (2001).
[35]H. Ibach, Physica Status Solidi **33**, 257 (1969).

Immobilization of Quantum Dots *via* Conjugated Self-Assembled Monolayers and Their Application as a Light-Controlled Sensor for the Detection of Hydrogen Peroxide

Waqas Khalid,[†,§] Mira El Helou,[†,§] Tobias Murböck,[†] Zhao Yue,[†,∥] Jose-Maria Montenegro,[†] Kirsten Schubert,[‡] Gero Göbel,[‡] Fred Lisdat,[‡] Gregor Witte,[†,*] and Wolfgang J. Parak[†,*]

[†]Fachbereich Physik and WZMW, Philipps-Universität Marburg, Marburg, Germany and, [‡]Biosystems Technology, Technical University of Applied Sciences, Wildau, Germany. [§]These authors contributed equally to this study. [∥]Present address: Department of Electronics, Nankai University, Tianjin, China.

ABSTRACT

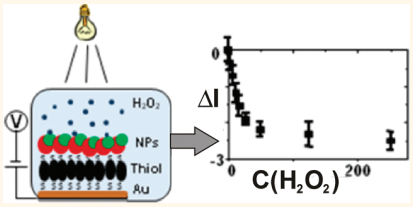

A light-addressable gold electrode modified with CdS and FePt or with CdS@FePt nanoparticles *via* an interfacial dithiol linker layer is presented. XPS measurements reveal that *trans*-stilbenedithiol provides high-quality self-assembled monolayers compared to benzenedithiol and biphenyldithiol, in case they are formed at elevated temperatures. The CdS nanoparticles in good electrical contact with the electrode allow for current generation under illumination and appropriate polarization. FePt nanoparticles serve as catalytic sites for the reduction of hydrogen peroxide to water. Advantageously, both properties can be combined by the use of hybrid nanoparticles fixed on the electrode by means of the optimized stilbenedithiol layer. This allows a light-controlled analysis of different hydrogen peroxide concentrations.

KEYWORDS: quantum dots · hydrogen peroxide · sensor · self-assembled monolayers · light-controlled detection

Most commonly, spatial resolution in electrochemical sensors is achieved by structured surfaces, such as arrays of electrodes. One alternative is addressing individual points on an unstructured electrode by light. The concept of such light-addressable electrodes has been introduced already decades ago.[1−3] Hereby, illumination of selected spots on the electrode surface generates a local photocurrent, and thus by scanning a light pointer across the sensor surface, different positions can be addressed; that is, spatially resolved measurements are possible[4] (*cf.* Figure 1a). Traditionally, such light-addressable sensors have been designed as microfabricated silicon chips, typically in doped silicon−silicon oxide/silicon nitride geometry. The essential element is a semiconductor layer, in which light-generated electron−hole pairs can be generated as local charge carriers with the light pointer.

In recent years, attempts have been reported to create similar setups, however, by placing a layer of semiconductor nanoparticles (quantum dots, QDs) on the surface of gold electrodes *via* conductive dithiols as a linker.[5,6] This approach has potentially several advantages. First, QD layers can be deposited on gold surfaces without the requirement of any microfabrication facilities. Second, due to the small size of the QDs and prevention of lateral current in the QD layer, in principle, better spatial resolution could be obtained. Third, besides semiconductor nanoparticles (QDs), other types of nanoparticles (NPs) can be added on top of the gold electrode, which could, for example, specifically trigger catalytic reactions. QDs have been characterized electrochemically.[7−11] Functionality of QD-modified gold electrodes as electrochemical sensors has been demonstrated before and also applied to the detection of enzymatic reactions.[12,13] Though attempts have been made to quantitatively optimize the QD layer on the gold surface and thus to improve sensor performance,[14] still a conclusive picture of the nanostructure of this interfacial layer is missing. In spite of the fact that in most images such NP layers are

* Address correspondence to gregor.witte@physik.uni-marburg.de, wolfgang.parak@physik.uni-marburg.de.

Received for review September 15, 2011 and accepted November 9, 2011.

Published online November 09, 2011
10.1021/nn2035582

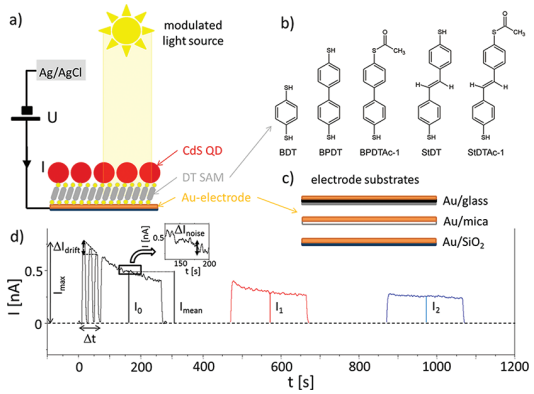

Figure 1. Experimental setup. (a) Setup of the light-controlled electrode comprising a QD layer on top of a gold electrode with an interfacial dithiol layer, an applied bias voltage, and a modulated light source. (b) Schematic illustration of the different dithiols. (c) Schematic illustration of the geometry of the different used gold substrates. (d) Photocurrent I recorded over time at fixed bias potential $U = +200$ mV.

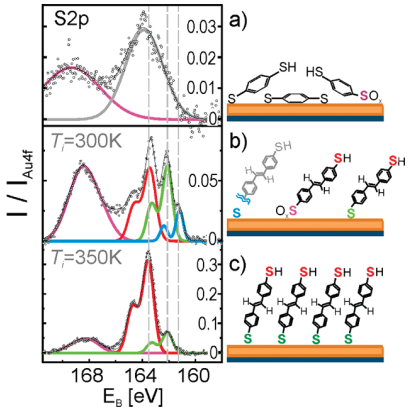

Figure 2. XPS of the different SAMs. (a–c) S2p XP spectra of the following SAMs on Au/SiO_2: (a) BDT, (b) StDT prepared by immersion at room temperature, and (c) at 350 K. The different sulfur species have been identified according to their binding energies as sulfides (AuS, blue), thiolates (AuS-R, green), thiols (R-SH, R-SAc, red), and sulfonates ($AuSO_x$, purple).

depicted as homogeneous self-assembled monolayers (SAMs), so far no detailed data exist, which would support such statement about the geometry.

In the present work, the QD–SAM–Au junction was systematically studied for the case of various dithiol SAMs adsorbed onto differently prepared gold electrodes in order to emphasize the importance of defined structures on device performance and to understand and optimize such sensors. Best device performance was obtained for a conjugated stilbenedithiol linker, which can be assembled as a structurally well-ordered monolayer by means of immersion at elevated temperature without the necessity of protection groups, while this was required for preparation at room temperature. This analysis has also to be seen in a more general context of investigating the structure of NP layers on top of plane surfaces as we demonstrate also the ability of making such layers of different materials. Besides semiconducting CdS QDs, which serve as a switch for light-controlled detection, also other NPs can be used, which for example locally catalyze reactions at the electrode surface. In the present case, we demonstrate the detection of H_2O_2 *via* catalytic degradation at the surface of FePt NPs and charge transfer from the electrode *via* the CdS QDs.

RESULTS AND DISCUSSION

Self-Assembled Dithiol Monolayers on Gold Surfaces. As the first step, electrodes were prepared by generating self-assembled layers of different dithiols (1,4-benzenedithiol (BDT), 4-4′-biphenyldithiol (BPDT), biphenyldithiol monoacetylated (BPDTAc-1), *trans*-4,4′-stilbenedithiol (StDT), and *trans*-4,4′-stilbenedithiol monoacetylated (StDTAc-1),[15] *cf.* Figure 1b) on three different Au substrates (Au/glass (with a thin Ti intermediate layer), Au/mica, Au/SiO_2, *cf.* Figure 1c). For this purpose, dithiols were dissolved at a concentration of 100 nM in dichloromethane or toluene and the Au substrates were immersed in these solutions. The amount of dithiols has been calculated to be enough to completely cover the Au surface. For characterization, XPS (X-ray photoelectron spectroscopy) was carried out at the HE-SGM synchrotron beamline of BESSY II in Berlin. All experimental protocols and several characterization measurements are described in detail in the Supporting Information.

In previous works, commonly, BDT has been used to immobilize QDs on Au electrodes,[5] although they form rather poorly ordered SAMs. Like in the case of benzenethiol,[16] their short backbone offers only a weak intermolecular stabilization, which leads to a reclined molecular orientation after adsorption on gold substrates.[17] As a consequence, the molecular film is lacking its function for anchoring the QDs provided by densely packed SAMs of upright oriented molecules with thiol groups exposed to the solution, and a noticeable oxidation of the thiolate anchoring groups takes place.

Indeed, the poor ordering of BDT SAMs is clearly evidenced by high-resolution XPS measurements (details of this analysis and about the experimental setup are given in the Supporting Information). As depicted in Figure 2a, corresponding XPS data of the sulfur region reveal an intense sulfonate signal at a binding energy of 168.5 eV, while the sulfur signals of the thiol and thiolate species are not separated, thus reflecting an inhomogeneous broadening due to disorder of the film. Largely improved ordering of SAMs has been achieved for thiols with larger but more rigid backbones such as oligophenylenes. Since dithiols potentially might bind with both thiol groups to the gold surface, protective monoacetylation was performed, permitting in turn selective anchoring; that is, only the free thiol can react with the gold surface.[15,18,19]

TABLE 1. Electrical Characterization of CdS QDs Immobilized on Top of SAMs of Different Dithiol Molecules That Were Adsorbed on Different Electrode Substrates[a]

dithiols	substrate	I_{mean} [nA]	$\tau_{drift} = (\Delta I/I_{mean})/\Delta t$ [s^{-1}]	I_{mean}/I_{noise}	$(I_0 - I_2)/I_0$ [%]
	Au/mica	0.27 ± 0.04	$(5.1 \pm 1.8) \times 10^{-2}$	5.7 ± 1.0	68.1 ± 2
BDT	Au/glass	0.67 ± 0.15	$(2.5 \pm 0.4) \times 10^{-2}$	17.3 ± 2.5	52.3 ± 2.4
	Au/SiO_2	1.56 ± 0.30	$(4.8 \pm 2.2) \times 10^{-4}$	55 ± 8	30.5 ± 4.4
BPDT	Au/mica	0.07 ± 0.02	$(4.8 \pm 1.2) \times 10^{-2}$	3.5 ± 1.1	100
	Au/glass	0.00[c]			
	Au/SiO_2	0.62 ± 0.10	$(3.8 \pm 2.4) \times 10^{-4}$	10.4 ± 1.7	32.1 ± 0.7
	Au/mica	0.11 ± 0.02	$(6.8 \pm 0.6) \times 10^{-2}$	15.5 ± 1.6	47.3 ± 1.8
BPDTAc-1[b]	Au/glass	0.3 ± 0.07	$(3.4 \pm 0.6) \times 10^{-2}$	26.7 ± 6.9	26.5 ± 4.9
	Au/SiO_2	1.76	1.3×10^{-4}	47.62	22.2
StDT	Au/mica	0.37 ± 0.07	$(2.5 \pm 0.7) \times 10^{-2}$	20.3 ± 5.6	35.6 ± 5.3
	Au/glass	1.08 ± 0.11	$(4.1 \pm 0.8) \times 10^{-2}$	40.0 ± 6.2	21.7 ± 5.2
	Au/SiO_2	1.57 ± 0.14	$(2.9 \pm 1.3) \times 10^{-4}$	48.9 ± 6.2	12.4 ± 1.1
StDTAc-1[b]	Au/mica	0.51 ± 0.12	$(1.9 \pm 0.8) \times 10^{-2}$	13.8 ± 3.1	46.6 ± 4.1
	Au/glass	1.45 ± 0.45	$(1.3 \pm 0.4) \times 10^{-2}$	38.5 ± 12.6	30.3 ± 2.3
	Au/SiO_2	2.51 ± 0.14	$(1.7 \pm 0.1) \times 10^{-4}$	137 ± 5.0	4.4 ± 0.6
StDT (heated)	Au/SiO_2	8.84 ± 0.50	$(8.4 \pm 0.5) \times 10^{-5}$	262.8 ± 15.2	1.0 ± 0.1

[a] The definition of the parameters is given in Figure 1d. All measurements have been replicated with at least two different electrodes (with the exception of BPDTAc-1 on Au/SiO_2 because the gold electrode turned out to be very fragile upon decapping), and data represent mean values with the corresponding standard deviation.. [b] The capping group had been removed after assembly of the dithiol SAM, before attachment of the QDs. [c] The photocurrent was below the detection limit.

In the present study, this strategy has been utilized for the case of BPDT by first preparing a SAM of BPDTAc-1 and, subsequently, decapping the acetate group by immersion in NaOH solution (*cf.* Supporting Information) before immobilization of the NPs. Despite a distinctly improved ordering of such dithiol SAMs (*cf.* Figure S5 of Supporting Information), the corresponding sensor characteristics have improved only little as compared to those using BDT SAMs (*cf.* Table 1). This result can be attributed to the modest conductivity of biphenyl-based SAMs (HOMO−LUMO band gap >4 eV), which in turn hampers an efficient electron transfer of the electron−hole pair from the illuminated QDs to the gold substrate. Note that this energy gap is almost independent of the number of phenyl rings because they are separated by C−C single bonds,[20] hence demonstrating that oligophenylene-based thiols are only partly conjugated.

Therefore, dithiols with fully conjugated backbones such as *trans*-stilbenes have been used instead because they exhibit a distinctly smaller HOMO−LUMO gap of only 2.14 eV.[21] In order to avoid simultaneous anchoring of both thiols of StDT, which again results in a partial oxidation and a poor film ordering (as indicated by corresponding XPS data shown in Figure 2b), also StDTAc-1 was used (for synthesis and film characterization, see the Supporting Information). After decapping, highly ordered StDT SAMs were obtained, which enable the fabrication of QD-based sensors with largely improved device performance (see detailed discussion in the next section and data in Table 1). In contrast to the partly conjugated SAMs, acetylated stilbenedithiol was found to be rather metastable and exhibits a rapid photo-oxidation within of several hours and, therefore, requires a quick processing after its synthesis.

In order to provide a more robust method to prepare highly ordered StDT SAMs, another approach has been tested. Guided by previous studies that reported a largely improved ordering of organothiol SAMs by immersion at elevated temperature or annealing in nitrogen atmosphere,[22,23] StDT SAMs were alternatively prepared by immersing Au/SiO_2 samples in thiol solution at about 350 K. Surprisingly, this procedure yielded excellent films even for nonprotected stilbenedithiols. Comparing the corresponding XPS data (see Figure 2c) with those obtained for SAMs of acetylated stilbenedithiols after decapping (*cf.* Figure S6c of Supporting Information), even further improved film quality has been assessed. This is evidenced by distinctly enhanced intensity ratios of the thiol-to-gold and the thiol-to-thiolate signals, which reflect a denser molecular packing and a more upright orientation. The latter finding has also been confirmed directly by near-edge X-ray absorption fine structure (NEXAFS) measurements (see Supporting Information, Figure S7), which yield a molecular tilt angle of 62° with respect to the surface plane.

Electrical Characterization of Quantum Dots Layers on Top of Self-Assembled Monolayers of Conductive Dithiols. In the next step, the influence of the various SAMs on the electrical properties of the light-addressable sensor has been investigated. For this purpose, CdS QDs were immobilized on top of the SAM-covered gold electrodes by immersion. CdS,[24] FePt,[25,26] and CdS@FePt[26,27] NPs have been synthesized according to previously published protocols. CdS@FePt NPs are hybrid NPs in which a bleb of CdS has been grown on spherical FePt

NPs.[26,27] Electrical characterization of the NP-covered electrodes was performed as previously described elsewhere.[14] Optical and structural data are shown in the Supporting Information (Figures S1−S3).

The experimental setup is depicted in Figure 1a. All experimental protocols and several characterization measurements are described in detail in the Supporting Information. The modulated light source was periodically switched on and off, and the photocurrent I was recorded during on-periods at fixed bias potential $U = +200$ mV in 0.1 M phosphate buffer solution (pH = 7.5) *versus* time. Four parameters were extracted from each photocurrent trace $I(t)$ as previously described[14] and depicted in Figure 1d: the average photocurrent I_{mean} (while turning on and off the light source in the first part of cylce), the current decay rate $\tau_{drift} = (\Delta I_{drift}/I_{mean})/\Delta t$, which is a measure for drifts in photocurrent ΔI_{drift}, the signal-to-noise ratio $I_{mean}/\Delta I_{noise}$, and the loss in photocurrent amplitude $(I_0 - I_2)/I_0$ after rinsing of the sensor surface with water. Here I_0 denotes the mean current (at the "on" interval at the end of each cycle) before any rinsing step and I_2 the mean current after the second rinsing step. Experimental details are described in the Supporting Information. It can be seen in Figure 1d that the loss of photocurrent during the second rinsing step is considerably lower than after the first rinsing step. This suggests that after several rinsing steps a stable equilibrium can be reached. The results obtained for sensors made from the various dithiols and different gold electrodes are summarized in Table 1. In all cases, electrical performance of the sensor was found to be best for Au/SiO_2 substrates. Note that there was no photocurrent for SAM-modified substrates without QDs (*cf.* Supporting Information Figure S15d). With one exception, Au/glass substrates lead to slightly better performance than Au/mica. We speculate that the Au/SiO_2 substrates were cleaner than the Au/glass substrates. The former electrodes were used for immersion shortly after their preparation, whereas the latter ones had been stored for months before usage. The Au/mica substrates were certainly the locally smoothest samples but have only a limited mechanical stability and tended to peel off during operation of the electrochemical cell; that is, adhesion of the gold was found to be rather poor.

Electrical performance depends directly on the quality of the SAMs, as this is also crucial for the attachment of the QD layers. XPS data have demonstrated to be rather defective SAMs in the case of BDT and BPDT. This goes hand in hand with poor sensor performance, that is, low signal-to-noise ratio and high reduction of the photocurrent after rinsing. SAM creation with capped dithiols (after decapping) resulted in clearly improved electrical characteristics (BPDTAc-1 *versus* BPDT and StDTAc-1 *versus* StDT). StDTAc-1 gave improved photocurrent measurements compared to BPDTAc-1, which can be attributed to its smaller

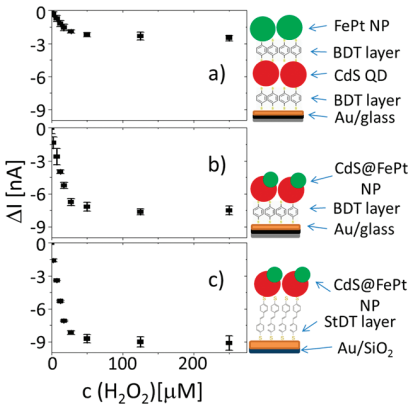

Figure 3. H_2O_2 detection in the different assemblies. (a) Alternating layers of CdS and FePt NPs and (b,c) CdS@FePt NPs were immobilized *via* dithiol SAMs (BDT (a,b), heated StDT (c)) on top of Au electrodes. Electrodes were constantly illuminated with a modulated light source, and the amplitude I of the photocurrent was detected at fixed applied bias voltage $U = -200$ mV. Different concentrations of H_2O_2 were added to the buffer solution (pH = 7.5) on top of the electrode. Changes in photocurrent due to addition of H_2O_2 are plotted *versus* the H_2O_2 concentration for the three depicted geometries.

HOMO−LUMO energy gap. Generally, the acetylation improves the ordering of dithiol SAMs, as it suppresses a reclined molecular orientation accompanied by partial oxidation of thiolate anchoring units. This is decisive, as oxo-functions have been demonstrated to act as electron traps which distinctly reduce the charge transport through SAMs[28] and therefore have to be avoided. Best electrical performance was achieved with SAMs of StDT created at elevated temperatures (on Au/SiO_2 substrates). This corresponds to a SAM with the highest coverage and upright packing yielding the fewest defects as indicated by XPS data. It also has the lowest loss of photocurrent upon rinsing, which presumably is due to loss of QDs for the SAMs. We thus conclude that the highly ordered structure of the StDT layer with fully reactive thiol groups exposed to the solution provides obviously good conditions for a defined immobilization of CdS QDs. The QDs have to bind to the thiol group by exchanging the ligand from their preparation on their surface with the surface group on the Au electrode. Thus, surface disorder and oxidized species on the surface would diminish the stable anchoring on the electrode, which is the reason for the best performance of StDT SAMs generated at high temperatures.

Sensing of H_2O_2. In a final step, we wanted to transfer the better understanding of the QD layer−SAM−Au electrode interface to improve sensing characteristics. Hereby, we also wanted to make use of the possibility of attaching different types of colloidal NPs. In the present study, we have chosen FePt NPs as the catalytic element since platinum is known for its electrocatalytic activity for hydrogen peroxide conversion, particularly reduction ($H_2O_2 + 2H^+ + 2e^- \rightarrow 2\ H_2O$), and as a

synthesis protocol for CdS@FePt has been readily available.[26,27] Hydrogen peroxide detection is an important analytical task both for physiological and non-physiological applications.[29−31]

Addition of FePt NPs to the CdS NPs on the Au surface should thus facilitate sensing of H_2O_2. Dose−response curves of the dependence of the photocurrent from hydrogen peroxide were recorded. Experimental details and characterization measurements are shown in the Supporting Information. In fact, no response of the photocurrent to H_2O_2 was found for either only CdS NPs or only FePt NPs (no photocurrent at all) immobilized at the Au electrode surface (*cf.* Supporting Information). This corresponds to previous findings with CdSe/ZnS NPs on electrodes, which also did not provide a surface for efficient hydrogen peroxide conversion.[13] However, the combination of CdS and FePt NPs on the Au electrode surface leads to a photocurrent, which amplitude depends on the H_2O_2 concentration in the buffer above the electrode (*cf.* Figure 3). Data about dependence on bias voltage and pH are shown in the Supporting Information. As mentioned above, reduction of H_2O_2 involves H^+ and e^-, which account for dependence on pH and bias potential, respectively. Thus, it is found that reduction is preferred in the acidic pH region (pH 5) and can be facilitated by decreasing the electrode potential from −0.2 to −0.6 V *vs* Ag/AgCl.

For combining CdS and FePt NPs, we have actually employed three different geometries. In the first case (Figure 3a), CdS NPs were attached on top of BDT SAMs on Au/glass substrates, which is compatible to conditions in our previous reports.[14] FePt NPs were added on top *via* an additional BDT layer. Please note that images are not drawn to scale and that, according to the XPS data, the structure is depicted only schematically. Clearly, a dependence of the photocurrent on H_2O_2 concentration (up to *ca.* 100 μM) could be observed.

Modern synthesis protocols also allow for the production of hybrid NPs, such as CdS NPs grown on top of FePt NPs.[26,27] In this way, a combination of two materials with different functionalities in one particle is possible. Figure 3b shows the resulting sensor response of CdS@FePt NPs immobilized *via* BDT on top of Au/glass electrodes. In comparison to the mixed assembly of CdS and FePt NPs (Figure 3a), a 2−3 times higher response to H_2O_2 could be observed. This can be easily understood. Upon reduction of H_2O_2, electrons need to be transferred from the FePt NPs (the location where the reduction takes place) to H_2O_2. Source of the electrons is the CdS QDs, which in turn receive electrons from the Au electrode *via* the conductive dithiol SAM. Effectively, electrons are injected from the Au electrode for reduction of H_2O_2, which results in a photocurrent with negative sign (*cf.* Figure 1a and Figure 3). In the case of CdS@FePt NPs, electrons can flow directly from the CdS to the FePt domain without having to cross an external interface. In the case of coassembly of CdS and FePt NPs, electrons need to be transferred from the CdS NPs to the FePt NPs *via* BDT molecules, which reduces the intensity of the photocurrent.

As indicated by the XPS characterization of the various dithiol SAMs and the electrical device characterization, best performance would be expected using StDT as linker and Au/SiO_2 as substrate. Dose−response curves of the photocurrent *versus* H_2O_2 concentration were similar to that recorded with BDT on top of Au/glass but had ∼20% improvement in photocurrent response (*cf.* Figure 3b,c). The error bars of the photocurrent measurements from typically three electrodes at low H_2O_2 concentrations also reveal that better signal-to-noise ratio for StDT is achieved (*cf.* Figure 3b,c). Consequently, StDT monolayers on top of Au/SiO_2 substrates result in a higher sensitivity for hydrogen peroxide detection and would allow for a lower H_2O_2 concentration as detection limit. Thus, this configuration offers the best geometry used in the present study, which goes far beyond the previously used setups.

CONCLUSIONS

It is demonstrated that the quality of interfacial dithiol films used to immobilize a QDs layer on gold electrodes has a severe influence on the electrical properties of a light-controlled sensor. The use of dithiol linkers with high conductivity and their assembly to a highly ordered, densely packed film with upright molecular orientation is of key importance in order to avoid partial oxidation of thiolate anchoring units. While an improved structural ordering of dithiol SAMs is achieved by first capping one of the thiol groups (*e.g.*, monoacetylation) followed by decapping after SAM formation, this strategy is complicated by a rapid photo-oxidation of the acetylated group in the case of low band gap materials such as the presently studied stilbenedithiols.

However, well-ordered StDT films have been achieved by immersion at elevated temperature, without the use of capping groups. Corresponding sensors reveal an enhancement of the photocurrent by more than an order of magnitude as well as a largely improved rinsing stability compared to devices based on the commonly used BDT. In this way, the ordered structure with fully reactive thiol groups exposed to the solution side improves the anchoring of the QDs.

Furthermore, we have demonstrated that inclusion of other types of NPs facilitates new detection modalities. In the present case, FePt NPs have been used as catalytic sites for the conversion of H_2O_2. These particles can be co-immobilized with the QDs, or more advantageously hybrid CdS@FePt NPs have been used

to combine the properties of photoexcitation with the catalytic activity. Thus, a photoelectrochemical analysis of H_2O_2 becomes feasible. This can be the basis of a set of biosensors involving enzymes with H_2O_2 as product.

MATERIALS AND METHODS

Preparation of Gold Electrodes. For the realization of the light-addressable sensor, three different kinds of gold substrates were prepared that have been utilized as electrodes. Initially, commercially available Au-coated glass slides (Au/glass) had been used, which were compared with self-made gold electrodes consisting either of Au layers evaporated onto mica sheets (Au/mica) or Au films sputtered onto oxidized Si wafers (Au/SiO_2).

Au/Glass. First, 100 nm of gold was evaporated on glass slides with the assistance of a 20 nm Ti adhesion layer. The Au/glass substrates were obtained from Institut für Mikrotechnik Mainz GmbH (iMM). These Au/glass slides were initially protected with a photoresist to avoid oxidation. The removal of the photoresist was done by sonication of the Au/glass substrates in toluene, ethanol, and acetone sequentially for 5 min each. To further remove impurities and leftover oxides, the Au surface was cleaned by cyclic voltammetry (CV) in 1 M NaOH (−0.8 V to +0.2 V) and 0.5 M H_2SO_4 (−0.2 V to +1.6 V). CV was done only with Au/glass. The other two electrode systems (Au/mica, Au/SiO_2) were used as received, as they were freshly prepared.

Au/Mica. Substrates were prepared by evaporating about 150 nm gold (99.995%, Chempur) at 540 K under high vacuum conditions ($\sim 10^{-8}$ mbar) onto freshly cleaved mica sheets, which had been heated to 525 K for 24 h before deposition to remove contaminations and residual crystal water. After deposition, the Au/mica substrates were flame-annealed in a protective nitrogen atmosphere for about 1 min at temperatures of 950 K to enhance crystallinity and reduce the roughness. This procedure yields high-quality Au films with atomically flat terraces of several hundred nanometers, exhibiting a (111) surface orientation that is well-suited for STM measurements.[32] Unfortunately, these substrates appear to be unstable during operation in the electrochemical cell since the gold films were found to peel off from the mica support.

Au/SiO_2. Substrates consist of gold films that were sputtered onto polished Si(100) wafers (Silchem). Before sputter-deposition of gold (99.98%) under argon atmosphere (POLARON sputter coater), the wafers which are covered with a native oxide layer were rinsed thoroughly with acetone and 2-propanol and subsequently dried in a nitrogen stream. To avoid electrochemical side reaction in the electrochemical cell, no adhesion layers (like Ti or Cr) were used. As a result, thick gold films (≥30 nm) were found to peel off from the wafers during the decapping procedure by immersion in NaOH solution (see below). This problem could be avoided by preparing ultrathin gold films with a thickness of only 14 nm.

Using atomic force microscopy (Agilent SPM5500), the surface morphology and roughness of the various gold substrates was characterized. In fact, Au/mica reveals atomically flat regions extending laterally over several hundred nanometers together with distinct steps of more than 10 nm between individual crystalline grains, hence yielding an overall mesoscopic waved surface. The other gold surfaces exhibit a nanogranular morphology with rms roughness values of about 3.5 nm for Au/glass and less than 2 nm for Au/SiO_2, which reflects the outstanding quality of the latter gold substrate.

Photoelectron Spectroscopy. The adsorption and chemical properties of the various self-assembled monolayers (SAMs) were characterized by means of high-resolution synchrotron-based X-ray photoelectron spectroscopy (XPS). Additional near-edge X-ray absorption fine structure (NEXAFS) measurements were carried out for StDT SAMs to obtain complementary information about the molecular orientation. All of these measurements were performed at the HE-SGM dipole beamline of the synchrotron storage ring BESSY II in Berlin (Germany). The used UHV end-station is equipped with a load-lock system that enables quick sample transfer. The XP spectra were recorded at a base pressure $p \leq 1 \times 10^{-9}$ mbar with a hemispherical energy analyzer (Scienta R3000) at an incident photon energy of 350 eV and monochromator settings (slit width) that enable an energy resolution of about 0.3 eV. All measured photoelectron binding energies have been referenced to the simultaneously recorded Au $4f_{7/2}$ peak (84.0 eV) of the substrate. Linear polarized synchrotron light (polarization factor 92%) was employed to measure the carbon edge NEXAFS spectra, which were acquired in partial electron yield mode using a channel plate detector operated with a retarding field. The NEXAFS raw data have been normalized in a multistep procedure by considering the incident photon flux and the background signal of the clean substrate.[33]

Signal-to-Noise and Drift Analysis of Photocurrent. To check the stability and resolution of the system, characterization measurements were performed. All of the measurements were recorded in 0.1 M phosphate buffer solution at pH 7.5. A constant bias potential of $U = +200$ mV was applied in all measurements. A bias potential of +200 mV was selected, as this potential had been used for the stability characterization of these kinds of electrodes in our previous work.[14] Note that this is a different potential than that used for H_2O_2 detection. Concerning the Au electrode preparation, all of the Au substrates had been immersed in 10 μM solutions of CdS QDs. For each system, at least two electrodes were tested. The Au/SiO_2 substrates were very fragile in the decapping solution of NaOH and ethanol. For characterization, a 10 s pulse of modulated light with a power $P_{illum} = 23$ mW was focused (light on) on the CdS QDs immobilized on top of the Au substrate (CdS/Au) to a spot size of approximately 2.5 mm^2. In a next period, light was switched off (light off) for 10 s. This process was repeated three times. After that, the CdS/Au substrate was illuminated with modulated light for about 200 s. The light on and light off cycles were controlled by a mechanical shutter. The current decay rate due to drift current τ_{drift} is defined, as depicted in Figure 1d, as the reduction of photocurrent under illumination within a time frame $\Delta t = 60$ s as $(\Delta I_{drift}/I_{max})/\Delta t$. I_{max} is the maximum amplitude of the photocurrent observed for each system. Signal-to-noise ratio ($I_{mean}/\Delta I_{noise}$): The light source was turned on for about 200 s continuously, and from the resulting photocurrent response, the mean current I_{mean} and the fluctuations in the current ΔI_{noise} were determined. The signal-to-noise ratio is defined as $I_{mean}/\Delta I_{noise}$. Rinsing degradation in photocurrent: Rinsing degradation in photocurrent was defined as the loss of photocurrent while rinsing the electrochemical cell two times with water (*cf.* Figure 1d). The cycle in Figure 1d was repeated three times. After each cycle, the electrochemical cell was rinsed: the phosphate buffer solution was taken out of the Teflon tank, water was poured inside the Teflon tank, water was taken out, and phosphate buffer solution was poured in again. I_0 is the mean current without any rinsing step, I_1 the mean current after the first rinsing step, and I_2 the mean current after the second rinsing step. The loss in photocurrent during the two rinsing steps was then calculated as $(I_0 - I_2)/I_0 \times 100\%$. All raw data are shown in the Supporting Information (Figure S10), and results are summarized in Table 1.

Acknowledgment. This work was supported in part by the German Research Foundation (DFG, Grant PA 794/3-1 to W.J.P. and LI706/2-1 to F.L.) and by the European Commission (EC, grant Nandiatream to W.J.P.). This work was partly funded by National Natural Science Foundation of China (Grant No.61001056) and Natural Science Foundation of Tianjin, China (Grant No.10JCZDJC15300) (to Z.Y.). W.K. acknowledges financial support by the HEC Pakistan/DAAD Germany. The authors are grateful to Dr. Abbasi Azhar for help in the nanoparticle synthesis and for recording the TEM images. We acknowledge the Helmholtz-Zentrum Berlin - Electron

storage ring BESSY II for provision of synchrotron radiation at beamline HE-SGM and travel support.

Supporting Information Available: Additional characterization of the various SAMs, synthesis of nanoparticles and dithiols, electrode preparation, and electrochemical characterization. This material is available free of charge *via* the Internet at http://pubs.acs.org.

REFERENCES AND NOTES

1. Engström, O.; Carlsson, A. Scanned Light Pulse Technique for the Investigation of Insulator-Semiconductor Interfaces. *J. Appl. Phys.* **1983**, *54*, 5245–5251.
2. Hafeman, D. G.; Parce, J. W.; McConnell, H. M. Light-Addressable Potentiometric Sensor for Biochemical Systems. *Science* **1988**, *240*, 1182–1185.
3. Licht, S.; Myung, N.; Sun, Y.; Light Addressable, A Photoelectrochemical Cyanide Sensor. *Anal. Chem.* **1996**, *68*, 954–959.
4. Parak, W. J.; Hofmann, U. G.; Gaub, H. E.; Owicki, J. C. Lateral Resolution of Light Addressable Potentiometric Sensors: An Experimental and Theoretical Investigation. *Sens. Actuators, A* **1997**, *63*, 47–57.
5. Stoll, C.; Kudera, S.; Parak, W. J.; Lisdat, F. Quantum Dots on Gold:Electrodes for Photoswitchable Cytochrome *c* Electrochemistry. *Small* **2006**, *2*, 741–743.
6. Katz, E.; Zayats, M.; Willner, I.; Lisdat, F. Controlling the Direction of Photocurrents by Means of CdS Nanoparticles and Cytochrome *c*-Mediated Biocatalytic Cascades. *Chem. Commun.* **2006**, 1395–1397.
7. Gaponik, N.; Poznyak, S. K.; Osipovich, N. P.; Shavel, A.; Eychmüller, A. Electrochemical Probing of Thiol-Capped Nanocrystals. *Microchim. Acta* **2008**, *160*, 327–334.
8. Poznyak, S. K.; Osipovich, N. P.; Shavel, A.; Talapin, D. V.; Gao, M.; Eychmüller, A.; Gaponik, N. Size-Dependent Electrochemical Behavior of Thiol-Capped CdTe Nanocrystals in Aqueous Solution. *J. Phys. Chem. B* **2005**, *109*, 1094–1100.
9. Kucur, E.; Riegler, J.; Urban, G. A.; Nann, T. Determination of Quantum Confinement in CdSe Nanocrystals by Cyclic Voltammetry. *J. Chem. Phys.* **2003**, *119*, 2333–2337.
10. Kucur, E.; Bücking, W.; Arenz, S.; Giernoth, R.; Nann, T. Heterogeneous Charge Transfer of Colloidal Nanocrystals in Ionic Liquids. *ChemPhysChem* **2006**, *7*, 77–81.
11. Gill, R.; Zayats, M.; Willner, I. Semiconductor Quantum Dots for Bioanalysis. *Angew. Chem., Int. Ed.* **2008**, *47*, 7602–7625.
12. Stoll, C.; Gehring, C.; Schubert, K.; Zanella, M.; Parak, W. J.; Lisdat, F. Photoelectrochemical Signal Chain Based on Quantum Dots on Gold-Sensitive to Superoxide Radicals in Solution. *Biosens. Bioelectron.* **2008**, *24*, 260–265.
13. Schubert, K.; Khalid, W.; Yue, Z.; Parak, W. J.; Lisdat, F. Quantum-Dot-Modified Electrode in Combination with NADH-Dependent Dehydrogenase Reactions for Substrate Analysis. *Langmuir* **2010**, *26*, 1395–1400.
14. Yue, Z.; Khalid, W.; Zanella, M.; Abbasi, A. Z.; Pfreundt, A.; Rivera-Gil, P.; Schubert, K.; Lisdat, F.; Parak, W. J. Evaluation of Quantum Dots Applied as Switchable Layer in a Light-Controlled Electrochemical Sensor. *Anal. Bioanal. Chem.* **2010**, *396*, 1095–1103.
15. Niklewski, A.; Azzam, W.; Strunskus, T.; Fischer, R. A.; Wöll, C. Fabrication of Self-Assembled Monolayers Exhibiting a Thiol-Terminated Surface. *Langmuir* **2004**, *20*, 8620–8624.
16. Käfer, D.; Bashir, A.; Witte, G. Interplay of Anchoring and Ordering in Aromatic Self-Assembled Monolayers. *J. Phys. Chem. C* **2007**, *111*, 10546–10551.
17. Joo, S. W.; Han, S. W.; Kim, K. Adsorption of 1,4-Benzenedithiol on Gold and Silver Surfaces: Surface-Enhanced Raman Scattering Study. *J. Colloid Interface Sci.* **2001**, *240*, 391–399.
18. Tour, J. M.; Jones, L.; Pearson, D. L.; Lamba, J. J. S.; Burgin, T. P.; Whitesides, G. M.; Allara, D. L.; Parikh, A. N.; Atre, S. V. Self-Assembled Monolayers and Multilayers of Conjugated Thiols, α,ω-Dithiols, and Thioacetyl-Containing Adsorbates: Understanding Attachments between Potential Molecular Wires and Gold Surfaces. *J. Am. Chem. Soc.* **1995**, *117*, 9529–9534.
19. Shaporenko, A.; Elbing, M.; Baszczyk, A.; von Hänisch, C.; Mayor, M.; Zharnikov, M. Self-Assembled Monolayers from Biphenyldithiol Derivatives: Optimization of the Deprotection Procedure and Effect of the Molecular Conformation. *J. Phys. Chem. B* **2006**, *110*, 4307–4317.
20. Bashir, A.; Käfer, D.; Müller, J.; Wöll, C.; Terfort, A.; Witte, G. Selenium as a Key Element for Highly Ordered Aromatic Self-Assembled Monolayers. *Angew. Chem., Int. Ed.* **2008**, *47*, 5250–5252.
21. Saltiel, J.; Khalil, G. E.; Schanze, K. *trans*-Stilbene Phosphorescence. *Chem. Phys. Lett.* **1980**, *70*, 233–235.
22. Cyganik, P.; Buck, M.; Strunskus, T.; Shaporenko, A.; Wilton-Ely, J.; Zharnikov, M.; Wöll, C. Competition as a Design Concept: Polymorphism in Self-Assembled Monolayers of Biphenyl-Based Thiols. *J. Am. Chem. Soc.* **2006**, *128*, 13868–13878.
23. Qi, Y.; Liu, X.; Hendriksen, B. L. M.; Navarro, V.; Park, J. Y.; Ratera, I.; Klopp, J. M.; Edder, C.; Himpsel, F. J.; Frechet, J. M. J.; *et al.* Influence of Molecular Ordering on Electrical and Friction Properties of ω-(*trans*-4-Stilbene)Alkylthiol Self-Assembled Monolayers on Au(111). *Langmuir* **2010**, *26*, 16522–16528.
24. Kudera, S.; Carbone, L.; Casula, M. F.; Cingolani, R.; Falqui, A.; Snoeck, E.; Parak, W. J.; Manna, L. Selective Growth of PbSe on One or Both Tips of Colloidal Semiconductor Nanorods. *Nano Lett.* **2005**, *5*, 445–449.
25. Sun, S.; Murray, C. B.; Weller, D.; Folks, L.; Moser, A. Monodisperse FePt Nanoparticles and Ferromagnetic FePt Nanocrystal Superlattices. *Science* **2000**, *287*, 1989–1992.
26. Zanella, M.; Falqui, A.; Kudera, S.; Manna, L.; Casula, M. F.; Parak, W. J. Growth of Colloidal Nanoparticles of Group II–VI and IV–VI Semiconductors on Top of Magnetic Iron-Platinum Nanocrystals. *J. Mater. Chem.* **2008**, *18*, 4311–4317.
27. Gu, H.; Zheng, R.; Zhang, X. X.; Xu, B. Facile One-Pot Synthesis of Bifunctional Heterodimers of Nanoparticles: A Conjugate of Quantum Dot and Magnetic Nanoparticles. *J. Am. Chem. Soc.* **2004**, *126*, 5664–5665.
28. Wang, Z. H.; Käfer, D.; Bashir, A.; Götzen, J.; Birkner, A.; Witte, G.; Wöll, C. Influence of OH groups on Charge Transport Across Organic–Organic Interfaces: A Systematic Approach Employing an "Ideal" Device. *Phys. Chem. Chem. Phys.* **2010**, *12*, 4317–4323.
29. Krylov, A. V.; Adamzig, H.; Walter, A. D.; Löchel, B.; Kurth, E.; Pulz, O.; Szeponik, J.; Wegerich, F.; Lisdat, F. Parallel Generation and Detection of Superoxide and Hydrogen Peroxide in a Fluidic Chip. *Sens. Actuators, B* **2006**, *119*, 118–126.
30. Guo, S. J.; Dong, S. J. Biomolecule–Nanoparticle Hybrids for Electrochemical Biosensors. *TrAC, Trends Anal. Chem.* **2009**, *28*, 96–109.
31. Karyakin, A. A. Prussian Blue and Its Analogues: Electrochemistry and Analytical Applications. *Electroanalysis* **2001**, *13*, 813–819.
32. Merzlikin, S. V.; Tolkachev, N. N.; Strunskus, T.; Witte, G.; Glogowski, T.; Wöll, C.; Grünert, W. Resolving the Depth Coordinate in Photoelectron Spectroscopy - Comparison of Excitation Energy Variation *vs.* Angular-Resolved XPS for the Analysis of a Self-Assembled Monolayer Model System. *Surf. Sci.* **2008**, *602*, 755–767.
33. Reiss, S.; Krumm, H.; Niklewski, A.; Staemmler, V.; Wöll, C. The Adsorption of Acenes on Rutile TiO_2(110): A Multi-Technique Investigation. *J. Chem. Phys.* **2002**, *116*, 7704–7713.

Immobilization of Quantum Dots *via* Conjugated Self-Assembled Monolayers and their Application as a Light-Controlled Sensor for the Detection of Hydrogen Peroxide

W. Khalid,[1$] M. El Helou, [1$] T. Murböck, [1] Z. Yue,[1] J.-M. Montenegro,[1] K. Schubert,[2] G. Göbel,[2] F. Lisdat,[2] G. Witte,[1*] and W. J. Parak[1*]

[1] Fachbereich Physik and WZMW, Philipps Universität Marburg, Marburg, Germany

[2] Biosystems Technology, Technical University of Applied Sciences Wildau, Germany

[$] both authors contributed equally to this study

[*]corresponding authors: gregor.witte@physik.uni-marburg.de

wolfgang.parak@physik.uni-marburg.de

SUPPORTING INFORMATION

I) Nanoparticle synthesis and electrode preparation

I.1) Synthesis of CdS nanoparticles

Chemicals: cadmium oxide (99.999%), nonanoic acid (97%), decylamine (98%), sulfur powder (99.9%, 100 mesh), iron pentacarbonyl (99.99%), octyl ether (99%), oleic acid (Tech 90%), oleyl amine (Tech 70%) were purchased from Sigma. Trioctylphosphine (TOP, 97%) and tri-n-octylphosphine oxide (TOPO, 99%) was purchased from Strem. 1,2-hexadecanethiol (>98%) was purchased from TCI Europe. Platinum acetylacetonate (98%) and cadmium acetylacetonate (98%) were purchased from ABCR chemicals. All solvents used for precipitation and re-dispersion of the particles (methanol, ethyl acetate, and chloroform) were purchased as anhydrous solvents from Sigma.

CdS nanoparticles (quantum dots, QDs) were synthesized using a previously published protocol.[1] Synthesis was performed in a three necked flask at low temperature by reacting the cadmium and sulfur:trioctylphosphine (S:TOP) in the presence of nonanoic acid and decylamine. Briefly, 514 mg of cadmium oxide (4 mmol), 2 g of nonanoic acid (12.6 mmol), and 2 g of decylamine (12.7 mmol) were mixed in a 50 mL three necked flask and the temperature of the complex was raised to 120°C under nitrogen flow. When the temperature had reached 120 °C, vacuum was applied for 15 minutes in order to remove volatile impurities. After 15 minutes, the temperature of the solution was increased up to 200 °C under nitrogen atmosphere. Cadmium oxide started to decompose at this temperature and the initial brownish solution started to become transparent. When the solution had become totally transparent, the temperature was lowered to 60 °C. At this temperature, 10 g of the solution of sulfur in trioctylphosphine (10% in weight, 31.2 mmol of S) was quickly injected. After the injection the temperature of the synthesis dropped to around 10 °C and was allowed to recover and increased to 80 °C. Once the temperature was at 80 °C the solution started to change the color from transparent to light yellow after 2 to 3 minutes. Aliquots were taken from the growth solution after each 3-4 minutes to observe the growth of the QDs.

When the desired size was reached the synthesis was stopped by removing the heating mantle and the QDs were precipitated at room temperature. For the precipitation of the QDs, 5-10 mL of chloroform was added followed by 20-30 mL of methanol. After addition of methanol, cloudiness in the solution was observed. This resulting solution was then centrifuged at 1800 rpm for 5 minutes and the precipitate was re-dispersed in chloroform. One more washing step was performed by adding 20-30 mL of methanol. After this second washing the precipitate was re-dispersed in 15-20 mL of chloroform and used for further characterization and experiments. The UV/Vis absorption and emission spectra of the CdS QDs used in this study are displayed in Figure S1.

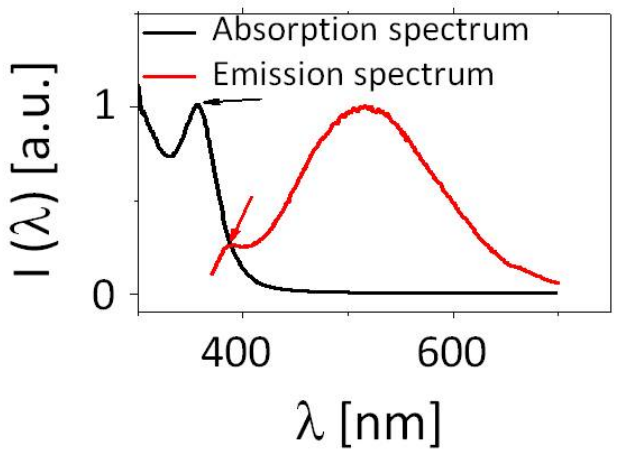

***Figure S1**: Normalized absorbance (black curve) and fluorescence spectra (red curve) of CdS QDs.*

The UV/Vis absorption spectrum shows the exciton peak of the CdS QDs at about 355 nm. The fluorescence emission peak due to exciton recombination is located at 386 nm. However, there is also a broad peak due to trap states emission located around 500 nm.[1] The concentration of the CdS QDs was determined from their absorption spectra using Beer-Lambert's law:

$$c = [A / (\varepsilon \cdot l)] D,$$

where A denotes the value of absorbance observed at the exciton peak, l is the path length of the cuvette, ε is the extinction coefficient and D is the factor by which stock solution was diluted before recording the UV/Vis spectrum. For CdS QDs the extinction coefficient was taken from Peng et al.[2] and a value of $\varepsilon = 12875\ M^{-1}cm^{-1}$ was used for the exciton peak at 355 nm. Throughout this study, CdS QDs solutions with a typical concentration of 10 μM were used. A corresponding transmission electron micrograph (TEM image) of the QDs is shown in Figure S3.

I.2) Synthesis of FePt nanoparticles.

Synthesis of the iron platinum (FePt) NPs was performed using the protocol previously reported by Sun.[3] In this synthetic method, FePt NPs were obtained by reacting $Pt(acac)_2$ and $Fe(CO)_5$ at high temperature. 1,2-hexadecanediol was used to reduce $Pt(acac)_2$ to Pt, whereas the high temperature of the synthesis caused the decomposition of $Fe(CO)_5$. A combination of oleic acid and oleyl amine was used for the stabilization of the NPs in solution. Briefly, in a 50 mL three necked flask 10 mL of octyl ether, 95 mg of $Pt(acac)_2$ (0.2 mmol), and 195 mg of 1,2-hexadecanediol (0.8 mmol) were mixed under nitrogen atmosphere. Once the solution was clear, 0.08 mL of oleic acid (0.3 mmol) was quickly injected into the solution, followed by two more injections, first one containing 0.08 mL of oleyl amine (0.3 mmol) and a second injection of 0.06 mL of $Fe(CO)_5$ (0.5 mmol). After the injections, the solution was heated to 280 °C at a heating rate of 12 °C/min. The solution was kept at this temperature for 15 minutes. Finally the heating mantle was removed to stop the reaction. After the solution had cooled down the NPs were precipitated from the solution at room temperature. The precipitation of FePt NPs was done by adding 15 mL of methanol to the growth solution, followed by a small quantity of ethyl acetate (2-3 mL) in order to prevent phase separation of the solvents. The final solution was precipitated by centrifugation at 800 rpm for 5 minutes and the precipitate was re-dispersed in 15-20 mL of chloroform.

The concentration of FePt NPs was determined from absorption spectra by using an extinction coefficient, which had been determined previously by recording the absorption of a NP solution and later determining the weight of the dried NPs by employing the empirical formula:[4]

$$c\ (\mu M) = 0.27000 \cdot A - 0.0045\ .$$

Here c represents the NP concentration (in units of μM) and A is the absorbance at λ=450 nm, recorded in a cuvette with an optical path length of 1 cm. Clearly, this method had to be seen just as a rough estimation for the NP concentration. This is in particular due to the fact that for the determination of the extinction coefficient only the molecular weight of FePt cores is considered, but the mass contribution of surfactant molecules on top of the FePt is neglected.[4] In this study, typical FePt NP concentrations of around 10 μM were used. Corresponding UV/Vis data and a TEM micrograph of FePt NPs are shown in Figures S2 and S3, respectively.

I.3) Synthesis of CdS@FePt nanoparticles.

Synthesis of CdS@FePt NPs was performed using a previously published protocol.[5, 6] For the synthesis of these hybrid NPs first FePt NPs were synthesized using the protocol described in the previous section. After formation of FePt NPs at 280 °C the solution was cooled down to 100 °C and 50 mg of sulfur powder (1.6 mmol) was added. After the addition of sulfur, the solution was allowed to react for 5 minutes. After this time, 1 g of TOPO (2.6 mmol), 105 mg of 1,2-hexadecanethiol (0.4 mmol), and 50 mg of cadmium acetylacetonate (0.2 mmol) were added.

These chemicals were added to the solution by just removing the septa of the reaction flask and dropping the chemicals inside. After the addition of these chemicals, the solution was left reacting for another 10 minutes. During these 10 minutes, CdS@FePt NPs were formed. The temperature of solution was increased to 260-270 °C at a heating rate of 5 °C/minute to anneal the crystalline structure of the formed NPs. Once the temperature had reached 260-270 °C, the reaction was stopped by removing the heating mantle. Precipitation was performed to get rid of unreacted molecules at room temperature. For the precipitation of CdS@FePt, 5 mL of chloroform was added to the growth solution, followed by 20-30 mL of methanol. The resulting solution was precipitated by centrifugation at 1200 rpm for 5 minutes and the precipitate was re-dispersed in chloroform.

The concentration of the CdS@FePt NPs was also estimated by using UV/Viis absorption spectra (*cf.* Figure S2). FePt NPs absorb at all wavelengths up to 900 nm, however, CdS NPs absorb only until around 500 nm. At wavelengths higher than 500 nm, matching of the absorbance spectra of FePt and CdS@FePt suggests that both species have the same concentration, as for these high wavelengths there should be no contribution from the CdS NPs. Again concentrations of around 10 μM of CdS@FePt NPs were used in this study. A corresponding TEM micrograph of the NPs is displayed in Figure S3.

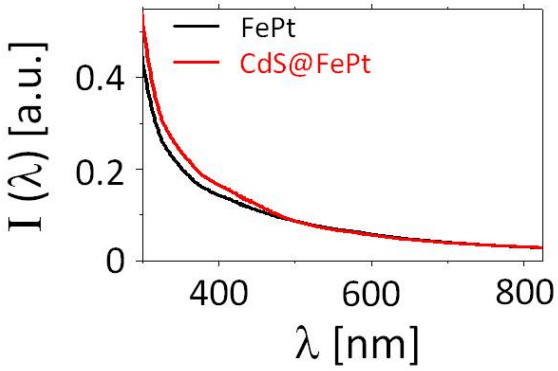

***Figure S2**: UV/Vis absorbance spectra of FePt (black curve) and CdS@FePt (red curve) NPs.*

TEM analysis was carried out in order to characterize the morphology for all the synthesized NPs. TEM images were recorded on a JEM 3010 high-resolution electron microscope (Jeol Ltd., Tokyo, Japan) operated at 300 kV. Samples for TEM analysis were prepared by depositing a drop of the NP solution on 300 mesh copper TEM-grids covered with a thin carbon supporting film.

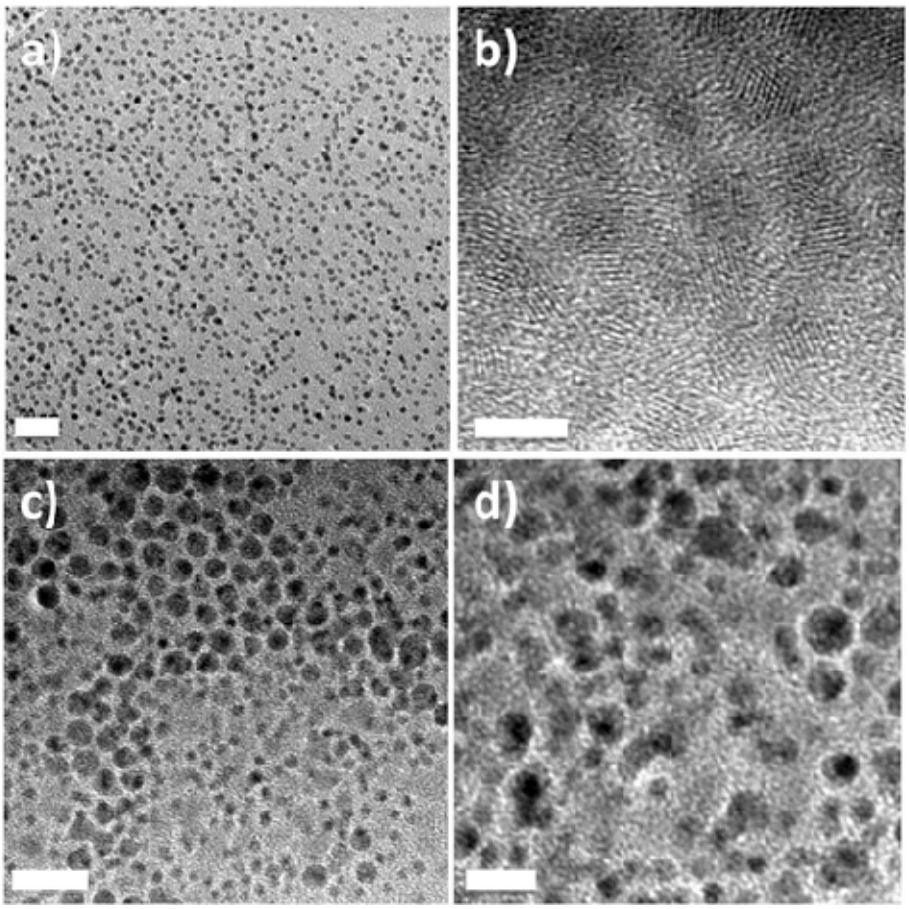

***Figure S3**: TEM images of (a) FePt NPs (scale bar corresponds to 20 nm), (b) CdS NPs (scale bar corresponds to 5 nm), and (c, d) of CdS@FePt NPs (scale bars correspond to 20 nm and 10 nm for (c) and (d), respectively).*

I.5) Synthesis of thiol linkers

Benzenedithiol (Alfa Aesar, 97%), Biphenyl-4,4'-dithiol (Sigma-Aldrich, 95%) and *trans*-4,4'-Stilbenedithiol (Sigma-Aldrich, >96%) and acetyl chloride (Fluka, puriss. ≥99.0%) were used as received without further purification.

- Synthesis of Biphenyl-4,4'-dithiol monoacetylated.

The synthesis of biphenyl-4,4'-dithiol monoacetylated is a slight modification of the already published protocol by de Boer et al.[7] In a 10 mL round bottom flask, biphenyl-4,4-dithiol (109 mg, 0.5 mmol) and acetyl chloride (39 mg, 0.5 mmol) were dissolved in 4 mL of anhydrous diethyl ether. Then, triethylamine (64 mg, 0.6 mmol) was added and the mixture was refluxed for 3 h. The solvent was evaporated and the mixture of starting dithiol, dithiol diacetylated and the desired monoacetylated dithiol was purified by preparative Thin Layer chromatography (CH_2Cl_2) to give the desired product as a slightly yellow solid. ^{1}H-NMR ($CDCl_3$) δ 2.43 (s, 3H), 3.49 (s,

1H), 7.33 (d, *J*= 6.8Hz, 2H), 7.45 (d, *J*= 6.8Hz, 2H), 7.57 (d, *J*= 6.8Hz, 2H). m/z (EI): 260 (M^+, 100%).

- Synthesis of *trans*-4,4'-Stilbenedithiol monoacetylated.

In a 10 mL round bottomed flask, *trans*-4,4'-stilbenedithiol (StDT, 4,4'-dimercaptostilbene) (20 mg, $8.2 \cdot 10^{-5}$ mol) was dissolved in 4 mL of CH_2Cl_2. To this solution acetyl chloride (6.42 mg, $8.2 \cdot 10^{-5}$ mol) and triethylamine (8.28 mg, $8.2 \cdot 10^{-5}$ mol) were added and the mixture was heated under reflux for three hours. Then the mixture was washed with water, dried over anhydrous $MgSO_4$, filtered, and the solvent was evaporated to give a residue that was further purified by preparative silica gel Thin Layer Chromatography (TLC) with CH_2Cl_2. As control, the starting StDT (R_f = 0.8) and the bifunctionalized *trans*-4,4'-*bis*(S-Acetyl)stilbenedithiol (R_f = 0.2), obtained as byproduct in the same reaction of which analytical data are identical to the literature were used.[8] Then, the product with retention factor (R_f = 0.5), placed between *trans*-4,4'-stilbenedithiol and *trans*-4,4'-*bis*(S-Acetyl)stilbenedithiol was taken. The monoacetylated product is highly labile and rapidly degrades being necessary to use it immediately after TLC.

I.6) Preparation of self-assembled dithiol monolayers on electrodes

SAMs of the various dithiols were prepared by immersing the gold substrates in 100 nM thiol solution dissolved in dichloromethane or toluene for 24 h. Afterwards, the samples were thoroughly rinsed with dichloromethane and subsequently dried in a nitrogen stream. If not specified otherwise, the substrates were immersed at room temperature. Benzenedithiol (BDT) *(TCI Europe nv, 95%),* 4-4'-biphenyldithiol (BPDT) *(Aldrich, 96%)*, and StDT *(Aldrich, 95%)* were used as received. For decapping of BPDTAc-1 or StDTAc-1 SAMs, the samples have been additionally immersed in a solution of EtOH + H_2O (1:1) + NaOH ($[OH^-]=10^{-4}$) for two days, then rinsed with ethanol (EtOH) and dichloromethane before drying them in nitrogen stream.[9]

I.7) Linkage of nanoparticles on top of dithiol self-assembled monolayers

The dithiol modified Au electrodes were immersed in a 10 μM solution of NPs dissolved in toluene for 48 h at room temperature. Afterwards, the substrates were rinsed with toluene to remove the NP excess and dried in air.[10] The immobilization of CdS QDs and other NPs is shown schematically in Figure S4(a-b), while the subsequent immobilization of FePt NPs was achieved in similar fashion as depicted in Figure S4(c-d).

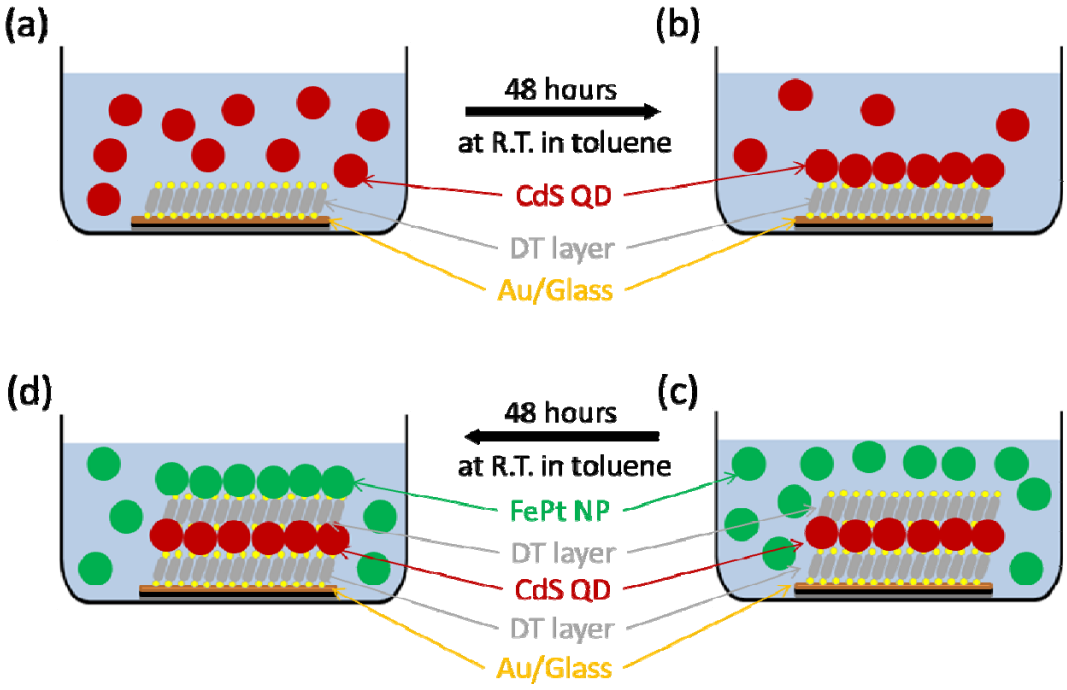

***Figure S4**: (a) Dithiol immobilized Au electrodes were immersed in NP solution dissolved in toluene for 48 h. (b) Hereby, the NPs were anchored to the Au substrate via the dithiol molecules. (c) Dithiol molecules were immobilized on CdS QDs by immersing the electrodes prepared in (b) in dithiol solution in toluene for 24 h. Then the electrodes were placed in FePt NP solution in toluene. (d) Hereby, the FePt NPs were also anchored via the dithiols to the CdS QDs.*

II) Characterization of self-assembled monolayers

BDT SAMs on gold reveal a quite limited ordering, because the molecules adopt a rather recumbent orientation allowing the formation of two thiolate bonds with the metal substrate per molecule.[11] As a consequence, the SAMs lack the desired protective function obtained for upright oriented molecules. Therefore, a noticeable oxidation of the thiolate anchoring units takes place, as evidenced by the corresponding XPS data shown in Figure 2. A similar effect was also found for fully conjugated aromatic SAMs in their diluted stripe phase, where molecules adopt a recumbent orientation.[12] In the course of preparing structurally improved dithiols SAMs that are well suited for a specific immobilization of NPs, various dithiols have been examined in this study. Since the surface quality of substrates is essential for the formation of well-ordered SAMs, several types of gold substrates have been investigated. Though Au/mica substrates are of superior quality and have been used in the past for detailed micro-structural characterizations of SAMs, they appear instable during operation of the electrochemical cells and tend to peel off from the substrate. Previous studies have also reported the problem of dissolving ions from the mineral silicate-substrate, which may affect the electrochemical measurements.[13-15] Therefore, all chemical and structural characterizations have been carried out for dithiol SAMs prepared on Au/SiO_2 substrate that were fabricated by sputter deposition.

To avoid a simultaneous interaction of both thiol units with the substrate, various strategies have been pursued in the past. On the one hand, SAMs with extended rigid backbones such as biphenyls have been used, which facilitate an intermolecular stabilization within the monolayer. On the other hand, one of the thiol groups has been replaced by a protection group that slows down the adsorption kinetics, so that only one goldthiolate bond per molecule is formed. The latter concept has been successfully demonstrated before for various molecules by substituting thiols by a thioacetate protection group. [9,16,17]

Figure S5 shows a comparison of high resolution XP spectra of the sulfur region that were recorded for BDT SAMs as well as for BPDTAc-1 SAMs before and after decapping of the thioacetate group. By considering a fixed spin-orbit splitting of the two S$2p_{3/2}$ and $2p_{1/2}$ doublet components of 1.18 eV as well as their constant intensity ratio of I($2p_{3/2}$) : I($2p_{1/2}$) = 2:1, the measured S$2p$ regions can be well decomposed into several distinct doublets. hence reflecting the presence of various sulfur species that can be unambiguously identified based on their binding energies. The analysis of the sulfur region of BPDT SAMs (*cf.* Figure S5(a)) yields the presence of two distinct doublets with S$2p_{3/2}$ binding energies of 162.0 eV (green curve) and 163.4 eV (red curve), which are identified as thiolate and thiol species based on their characteristic binding energies.[18] An additional much weaker doublet appears at 161.3 eV (blue curve), which is attributed to sulfide species that are formed by partial dissociation of the SAMs potentially caused by radiation damages.[19] For dithiol SAMs with homogeneously upright oriented molecules, a larger thiol peak intensity compared to the thiolate signal is expected, because photoelectrons emitted from the anchoring group are attenuated by the SAM. As the thiolate signal actually dominates the thiol signal, this indicates that BPDT molecules are not upright

oriented but instead are rather lying on the gold surface and are partially forming dithiolates. Thus, like in case of BDT also BPDT SAMs are not well-ordered and thiolate species can be rapidly oxidized upon exposure to air to sulfonates, which is evidenced by the broad XPS signal around 168.5 eV (purple curve).[20]

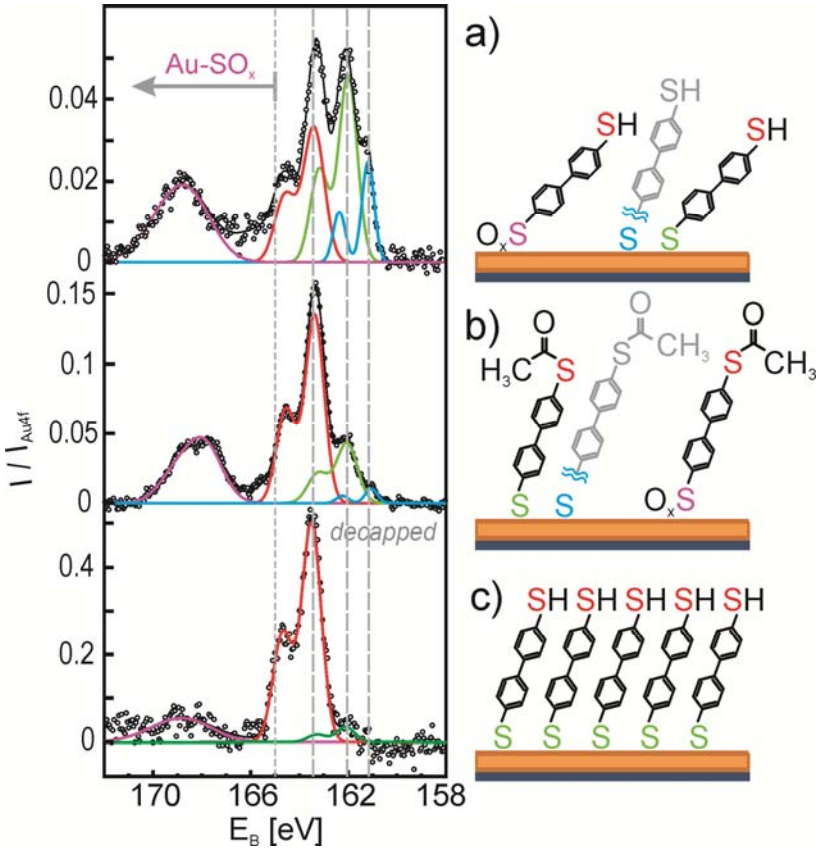

***Figure S5**: S2p XPS-spectra of different dithiol SAMs assembled on Au/SiO_2 substrates. (a) BPDT, (b) BPDTAc-1, and (c) after decapping of the thioacetate protection group. The spectra can be well decomposed into different sulfur doublets which can be identified according to their binding energies as sulfides (AuS, blue), thiolates (AuS-R, green), thiols (R-SH, R-SAc, red), and sulfonates ($AuSO_x$, purple).*

By capping one S–H group of BPDT with an acetate group, the anchoring of the remaining thiol is favored due to its higher affinity to gold compared to the acetate group and, hence, yields an improved quality of SAMs. This is clearly evidenced by the corresponding XP spectrum (*cf.* Figure S5(b)) revealing a largely enhanced thiol to thiolate intensity ratio, which indicates a more homogeneous upright orientation. At the same time, the intensity of the sulfonate and sulfide species is also reduced. After decapping of the acetate end group, the thiol to thiolate peak intensity has even further increased reflecting the formation of regions of more densely packed

and upright standing SAMs than the capped ones. This enhanced packing density can be attributed to steric effects of the respective end groups (–$SCOCH_3$ *vs.* –SH). Interestingly, also the sulfonate and sulfide signal almost completely disappeared upon decapping, which indicates that immersion in NaOH solution causes a removal of this species.

Next, we have used dithiols with a stilbene backbone, whose conjugation facilitates a high conductivity. In addition, these molecular entities reveal sufficient large solubility to enable SAM formation from immersion, while this becomes very critical or almost impossible for organothiols with extended acene backbones.[12] Figure S6(a) depicts the XPS data of the sulfur region of a StDT SAM prepared by immersion at room temperature. Similar to the case of BPDT, three sulfur doublets were identified reflecting the presence of thiol, thiolate, and sulfide species as well as a broad, even more intense sulfonate related peak around 168.5 eV. From the ratio of the thiol to thiolate peak intensities and the presence of an intense sulfonate signal, it is again concluded that the monolayer possesses many defects including molecules with a recumbent orientation on the gold electrode.

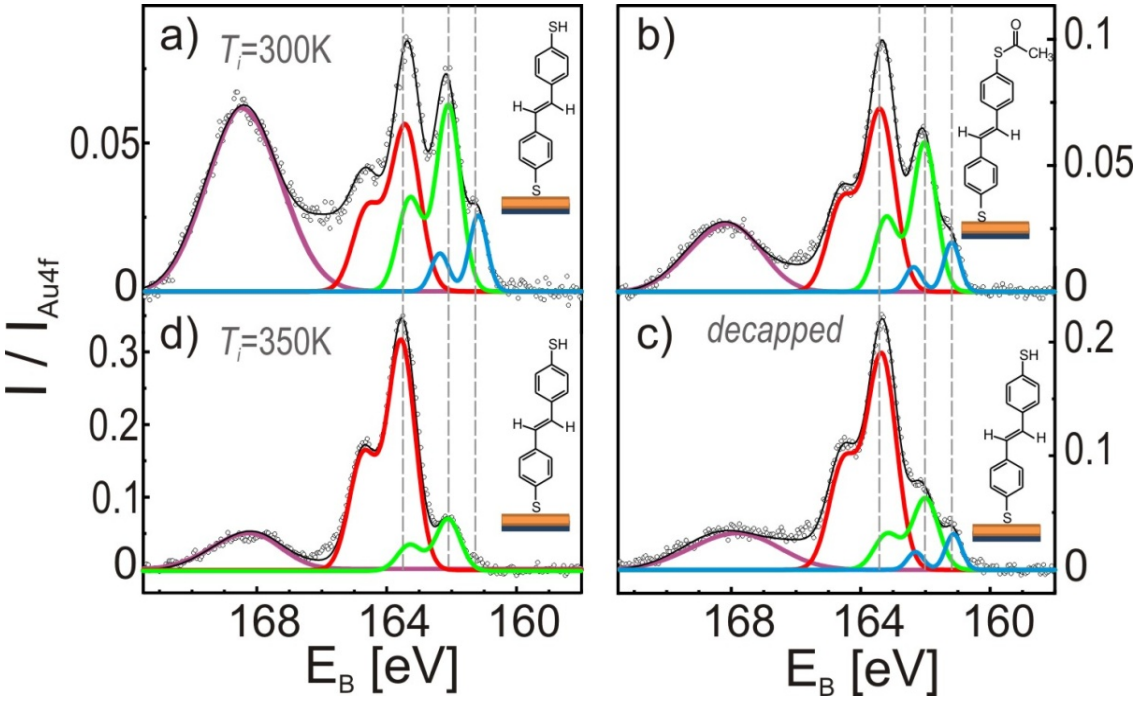

***Figure S6**: S2p XPS spectra of Au/SiO_2 electrodes modified with (a) StDT SAM immersed at RT, (b) protected StDTAc-1 SAM immersed at room temperature, (c) same as (b) but after decapping and d) StDT SAM prepared by immersion at 350 K. According to their binding energies various sulfur species marked by colored curves have been identified (cf. Fig. S5).*

Substituting one thiol group by an acetate group improves the film ordering as evidenced by the XPS data obtained for the StDTAc-1 SAM (*cf*. Figure S6(b)). Note that the sulfur species of the thioacetate group exhibits the same binding energy as the thiol unit.[19] In this case, the ratio of the thiol/thioacetate to thiolate peak intensities is reversed and at the same time the sulfonate signal is distinctly reduced. After decapping of the StDTAc-1 SAM, an even further reduction of the sulfonate signal and an increased ratio of the thiol to thiolate peak intensities was found (*cf*. Figure S6(c)), which reflects a larger attenuation of the thiolate photoemission signal and thus a more upright molecular orientation. Though this strategy yields an improved film ordering of StDTAc-1 SAM, the capped stilbenedithiols possess a rather limited stability and reveal a rapid aging and degradation. Already few hours after its synthesis the pale yellow StDTAc-1 solution darkened with time suggesting a photo-oxidation at ambient conditions. In previous works, it was found that the ordering of (partly aromatic) SAMs can be largely improved by immersion at elevated temperatures.[21,22] Therefore, we have also tested an alternative strategy to improve the ordering of stilbenedithiol SAMs by immersion at elevated temperatures (about 75 ^{o}C) without using any acetate protection group. As depicted in Figure S6(a,d), the corresponding thiol S*2p* XP intensities reveal an increase of almost one order of magnitude for immersion at elevated temperature compared to room temperature preparation. Moreover, this preparation yields no sulfide species and a distinctly reduced sulfonate signal, hence indicating a superior SAM quality of densely packed more upright oriented molecules. This improved ordering even exceeds the film quality achieved by first using an acetate-protected StDT and subsequently decapping it.

In order to further characterize the molecular ordering and to determine directly the molecular orientation, NEXAFS measurements of StDT SAMs prepared at different temperatures were carried out. The carbon edge NEXAFS data of StDT reveal a distinct π*-resonance at 285 eV followed by several rather broad σ*-resonances at higher photon energies. The polarization dependency of the π*-resonance intensity, I_π , can be used to characterize the molecular orientation within the films, since it depends on the orientation of the electrical field vector **E** of the incident synchrotron light relative to the molecular transition dipole moment **T** according to $I_\pi \propto |E \cdot T|^2$. For π* excitations, **T** is oriented normal to the ring plane of the aromatic moieties, hence enabling a determination of their orientation relative to the sample normal from angular dependent NEXAFS measurements taken at different angles of incidence, θ.[23] In case of the room temperature preparation, no dichroism occurs which indicates either a complete isotropic molecular orientation or an average molecular orientation that is close to the magic angle of $\alpha = 55^{o}$. Together with the XPS data, we conclude that the room temperature preparation yields rather disordered films. A quite different signature was observed for the StDT SAMs prepared by immersion at elevated temperature. In that case, a noticeable dichroism was found in the NEAXFS spectra recorded for different orientations of the incident X-ray light (*cf*. Figure S7(b)). The quantitative analysis of the molecular angle yields an average molecular tilt angle of $\alpha = 62^{o}$ which corroborates a more upright orientation concluded above already from the XPS data.[24,12,23]

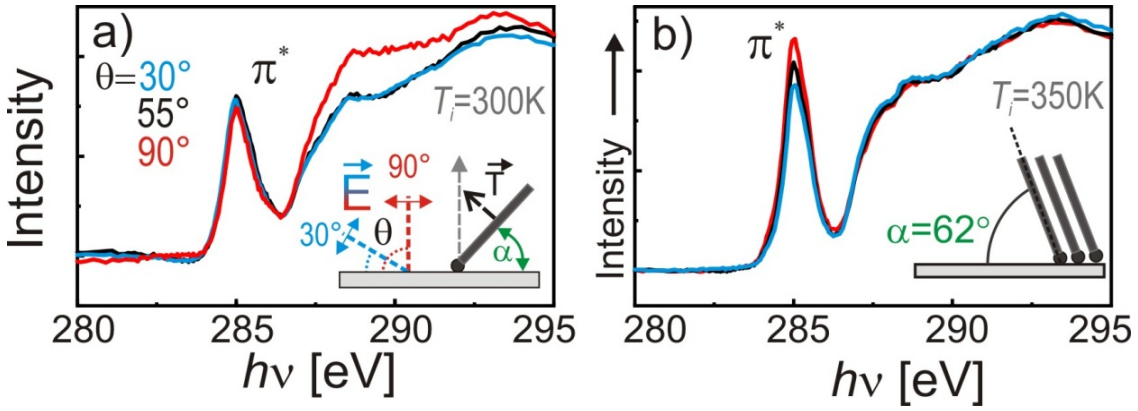

***Figure S7**: Carbon edge NEXAFS spectra of StDT SAMs prepared by immersion (a) at room temperature and (b) at 350 K, which were recorded for different angles of incidence of the field vector E relative to the surface plane, θ, according to the experimental geometry depicted in the inset in (a). From the angular dependency of the π* resonances, the orientation of the aromatic backbone relative to the surface, α, has been determined.*

III) Electrochemical characterization

III.1) Set-up for electrochemical measurements

III.2) Signal-to-noise and drift analysis of photocurrent

III.3) Detection of hydrogen peroxide

III.1) Set-up for electrochemical measurements

The electrochemical set-up consists of five major parts; a light source, a three-electrode system, an electrochemical cell, a chopper, and a lock-in amplifier, *cf*. Figure S8.

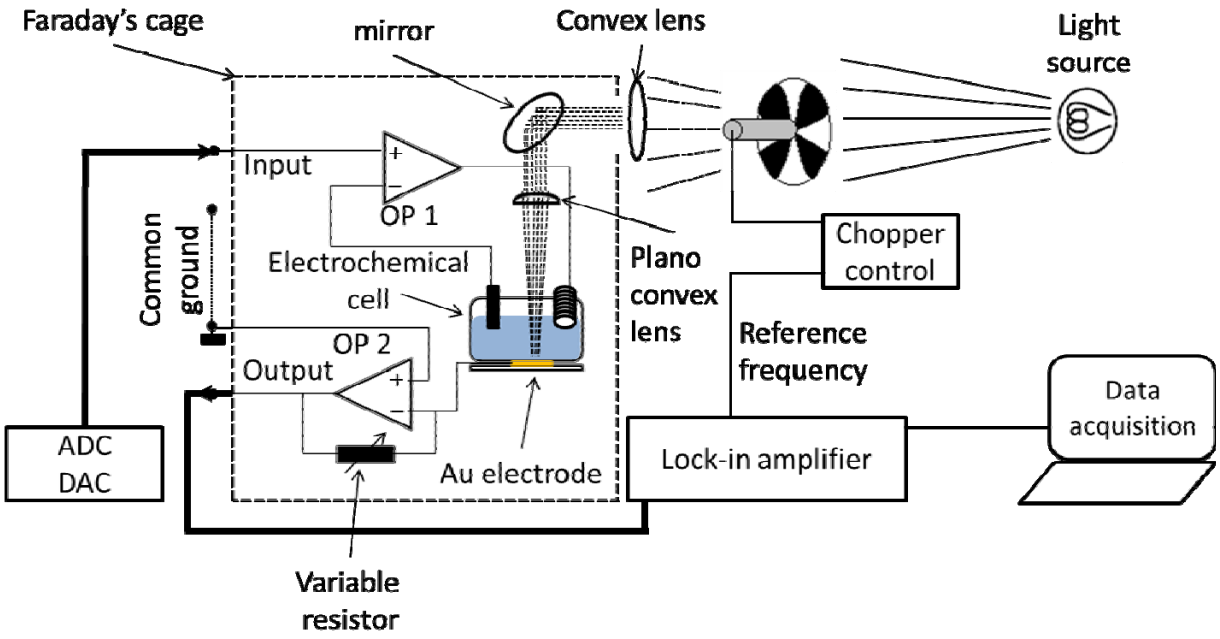

***Figure S8**: Block diagram of the electrochemical measurement set-up. Light is focused on the Au substrate with the help of a convex lens, a mirror, and a plano-convex lens. Light was modulated with a reference frequency with the help of a chopper. Two operation amplifiers are used in the three-electrode system. OP1 warrants that the potential between the Ag/AgCl reference and the Au working electrode remains constant. The bias potential to the working electrode is provided by an analog-to-digital converter (in the ADC/DAC setup). The output signal is read by a lock-in amplifier. The lock-in amplifier only amplifies the component of the signal at the reference frequency and filters out other frequencies. The output of the lock in amplifier was read with an analog-to-digital converter with a PC through the serial port.*

Light source: A Xenon arc lamp, which was controlled by a lamp power supply LPS 220 (Photon Technology International), was employed. It emits in the range of 300 nm to 700 nm. A 45°

inclined mirror and a couple of collecting lenses were used to direct the light from the arc lamp to the electrochemical cell as shown in the block diagram Figure S8. The local illumination power (P_{illum}) of the resultant light spot of around 3 mm diameter was measured with a photometer (Fieldmaster photometer, Coherent). For the electrochemical experiments reported in this study, a fixed illumination power of P_{illum} = 23 mW was used.

Electrochemical cell: A sketch of the homemade Teflon electrochemical measurement cell is shown in Figure S9. It comprised a hollow Teflon tank, which contains bath solution of up to 20 mL. The auxiliary and reference electrode supports can be seen from top view in Figure S9(a). Within the Teflon tank there is a 2.5 mm hole. The Au substrate is squeezed with the help of an O-ring between the Teflon tank and a Teflon sheet. In this way, the QDs-covered Au surface comes in contact with the bath solution through the 2.5 mm hole. The contact with the working electrode is made with a conducting screw and spiral combination as shown in Figure S9(b). Light is focused on the Au surface through the 2.5 mm hole from top with the help of a 45° inclined mirror, as indicated in the block diagram Figure S8. The cell is sealed with the help of screws as shown in Figure S9.

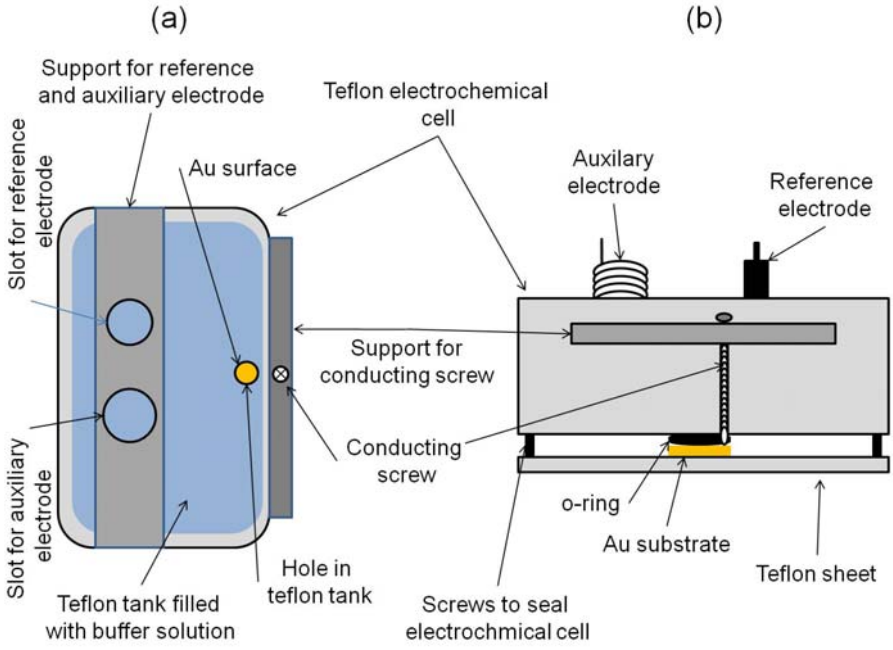

***Figure S9**: (a) Top view of the electrochemical cell. It shows the support for the reference and auxiliary electrodes. The Teflon tank is filled with 0.1 M phosphate buffer solution. A hole in the Teflon tank enables the contact between the buffer solution and the Au electrode surface. A conducting screw-spiral combination is mounted with a support and makes the electrical connection for the application of bias potential to the Au electrode. (b) Front view of the electrochemical cell. The spiral like auxiliary and rod shaped reference electrodes are shown. The Au substrate is squeezed between the Teflon tank and a Teflon sheet with the help of an O-ring. The seal is provided with the screws. The electrical connection to the Au substrate is established with the conducting screw-spiral combination.*

Three-electrode system: A three-electrode system was necessary because of the limitations of two-electrode systems. In two-electrode systems the current between the two electrodes as well as the applied potential can be measured. The problem is that there are three regions over which the potential drop occurs: two electrode-solution interfaces and the solution. Only the potential drop over the whole system can be estimated in two-electrode systems, but the potential drop at the working electrode cannot be estimated. In three-electrode system the functions of the counter electrode are divided between the reference and auxiliary electrodes. Here the potential between the working and reference electrodes is controlled and the current passes between the working and auxiliary electrodes. Figure S8 shows the block diagram of the home-made three-electrode geometry. The reference electrode is directly connected with the '–' input of the first operation amplifier (OP1). No current flew through the reference electrode (Ag/AgCl saturated). The purpose is to ensure that the voltage difference between the reference electrode and the working electrode (Au substrate) always remained constant. OP1 acts as voltage follower circuit, whose output went to the auxiliary electrode (in this case a spiral like Pt wire). The second operation amplifier (OP2) has a variable resistor mounted between the '–' input and the output of OP2 to increase the sensitivity of the instrument. OP2 serves as current-to-voltage converter. A computer with an interface card for a digital-to-analog (DAC) and analog-to-digital (ADC) converter was used to operate the three-electrode system. A ±2 V input and output range was set for the DAC and ADC lab board. Input and output resolution is 16 bit.

Optical chopper: An optical chopper was placed in the path of the incident light. The main purpose of the chopper was to modulate the light at a reference frequency. The optical chopper had a controller, which was used to tune the desired frequency. This chopper was purchased from Scitec instruments. For the electrochemical experiments, a reference frequency of 23.3 Hz was used.

Lock-in amplifier: The lock-in amplifier (EG&G Princeton Applied research, model number 5210) uses phase-sensitive detection to improve the signal-to-noise ratio in the electrochemical experiments. The phase-sensitive detection required that the analytical signal is modulated at a reference frequency (in our case 23.3 Hz as provided by the optical chopper). The lock-in-amplifier amplifies only the component of the input signal at the reference frequency and filters out all other frequencies. In this way, the signal-to-noise ratio could be enhanced significantly.[10] For all measurements, a time constant of 1 s was used. The output of the lock-in amplifier was directly read with the help of a serial port interface.

III.2) Signal-to-noise and drift analysis of photocurrent

The raw data concerning the characterization measurements are shown in Figure S10 and the corresponding results in Figure S11.

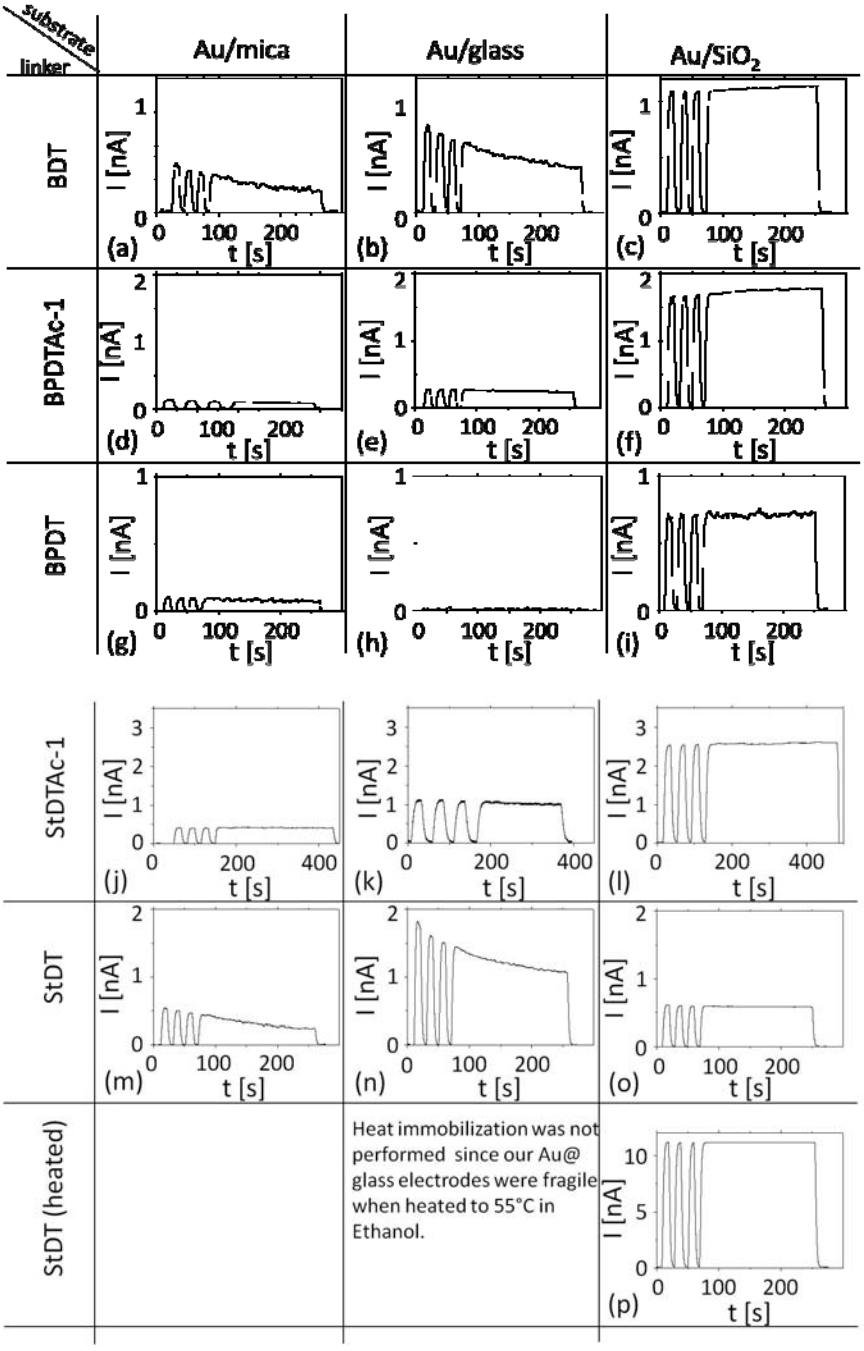

***Figure S10**: Overview of photocurrents at a constant bias potential U = +200 mV for CdS modified Au electrodes via different SAMs. A modulated light pointer with the power P_{illum} = 23 mW was focused on the Au electrodes while they were in contact with 0.1 M phosphate buffer of pH 7.5.The results are summarized in Table 1 and Figure 1d of the main manuscript.*

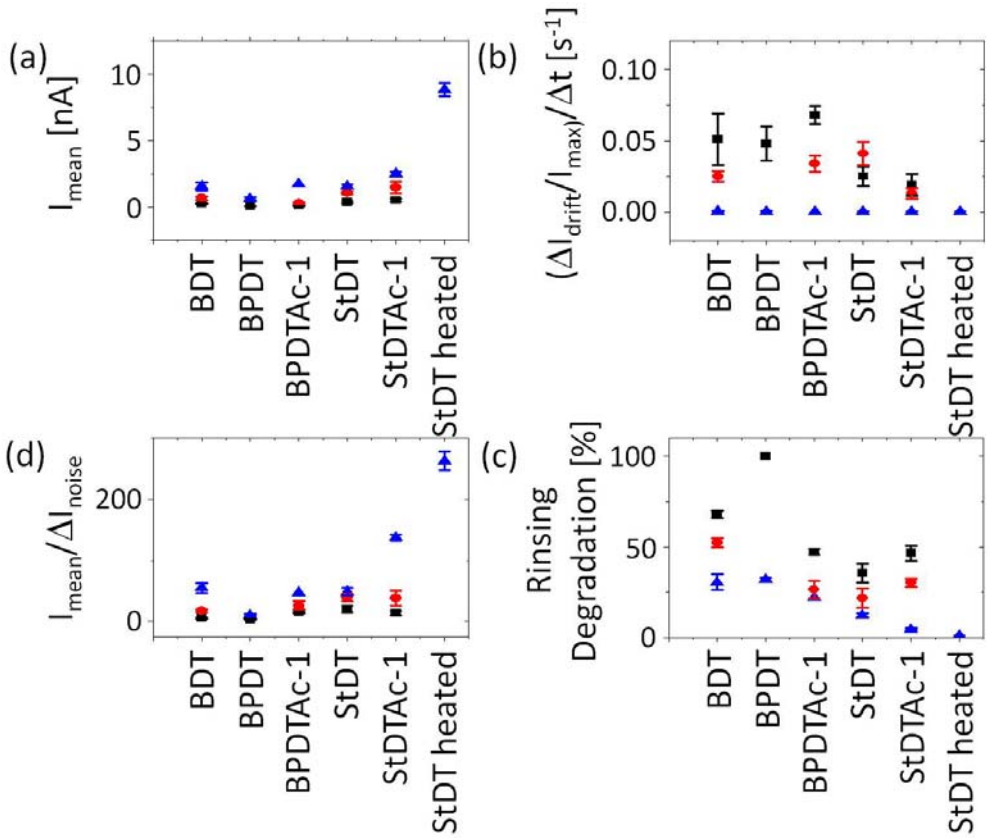

***Figure S11**: Summary of the results from Figure SI-III.3.* ■ ● ▲ *, represent Au/mica, Au/glass, and Au/SiO_2, respectively. (a) I_{mean} is the average photocurrent as measured for each electrode under illumination for a time interval of Δt = 200 s. (b) For each electrode the influence of drift on the photocurrent was derived as $(\Delta I_{drift}/I_{max})/\Delta t$. (c) The degradation of each electrode after two rinsing steps is defined as $[(I_0-I_2)/I_0] \times 100\%$. (d) The signal-to-noise ratio is derived by dividing the mean current attained in (a) by the fluctuations in photocurrent ΔI_{noise} as measured for each electrode under illumination during the time interval Δt = 200 s. The values are averages of measurements on two different electrodes and standard deviations as displayed as error bars.*

III.3) Detection of hydrogen peroxide

Hydrogen peroxide (H_2O_2) is one of the most important products or substrates of enzyme catalyzed redox reactions.[25,26] We were able to detect H_2O_2 electrochemically with slight modification of the NP/Au electrodes. Hereby, changes in H_2O_2 concentration in the buffer solution were measured as changes in the output photocurrent. In Figure S12, different geometries of NP/Au electrodes and their sensor characteristics are displayed. In all cases, H_2O_2 was detected in 0.1 M phosphate buffer with pH 7.5. For CdS QDs immobilized via BDT molecule on Au/glass substrates (*cf.* Figure S12(a)), no significant changes in photocurrent at an applied bias potential of -200 mV was observed. In a next geometry, FePt NPs were used, since

Pt can act as a catalyzer to reduce H_2O_2. As shown in Figure S12, however, no photocurrent was observed for this geometry. In a third geometry, FePt NPs were anchored by a SAM of BDT on top of CdS QDs (*cf*. S12(c)) resulting in two layers of NPs with independent functions. The CdS QDs provided the photocurrent signal and the FePt particles acted as an electrocatalyst for H_2O_2. With this hybrid system, we were able to detect H_2O_2 in 0.1 M phosphate buffer with pH 7.5 at an applied bias potential of -200 mV. For all geometries dose-response curves were recorded. First, the base current without H_2O_2 was detected I(c=0). Then, a known concentration of H_2O_2 was mixed with phosphate buffer and poured into the electrochemical cell and the respective photocurrent I(c) was measured. The H_2O_2 concentration was increased after each measurement / rinsing step. In the present study, the concentration of H_2O_2 was increased from 2.5 µM to 250 µM. In this way, the photocurrent response $\Delta I(c) = I(c) - I(c=0)$ was determined.

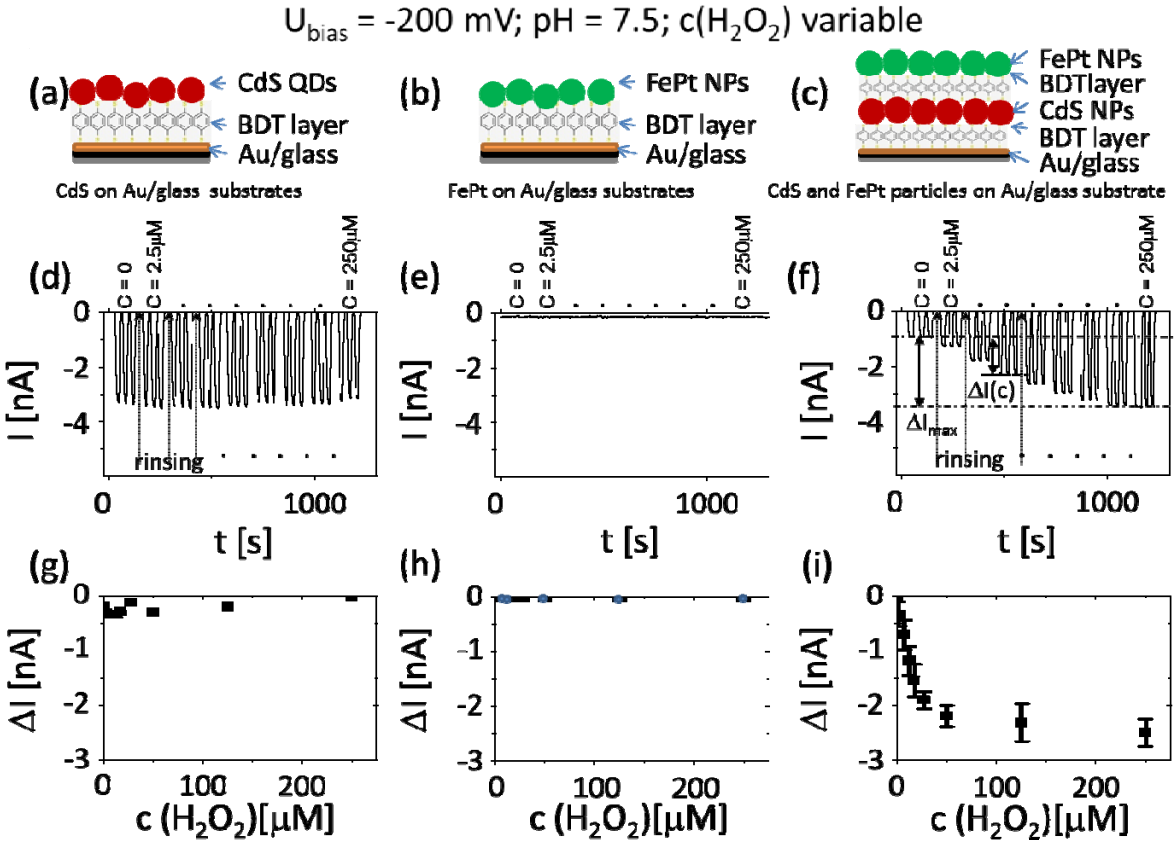

***Figure S12**: A constant bias potential U = -200 mV was applied to Au/glass electrodes with immobilized (a) CdS QDs, (b) FePt NPs and (c) CdS and FePt NPs. The photocurrent I was measured for each system (a-c) in 0.1 M phosphate buffer solution containing different concentrations of H_2O_2 (d-f). In (f), the way to measure dose-response curves is depicted. In (g-i), the dose-response curves as derived from the data shown in (d-f) with $\Delta I(c) = I(c) - I(c=0)$ are depicted.*

For the CdS and FePt hybrid structure, parameters as bias potential and pH of the buffer solution were varied and their effect on the detection of H_2O_2 was investigated. Data are displayed in Figure S13. Similar investigations were also performed for other electrode geometries that are summarized in Figures S14 and S15.

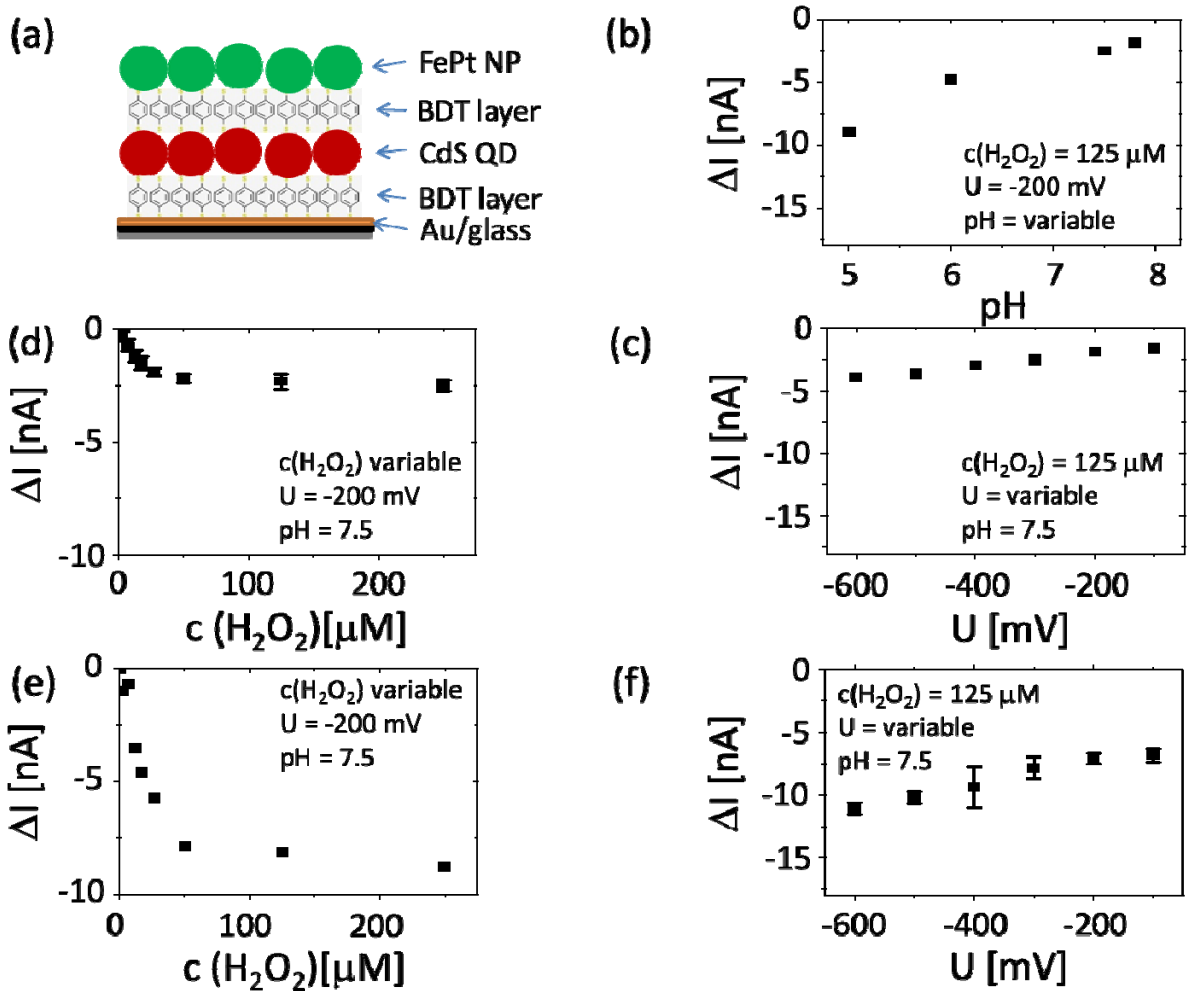

***Figure S13**: (a) Geometry of the hybrid NPs system (CdS and FePt) immobilized on Au/glass. (b) At an applied potential of -200 mV and a concentration of 125 µM of H_2O_2 mixed with 0.1 M phosphate buffer, changes in photocurrent at different pH are plotted. Also effects upon changing the bias potential U and H_2O_2 concentration are displayed.*

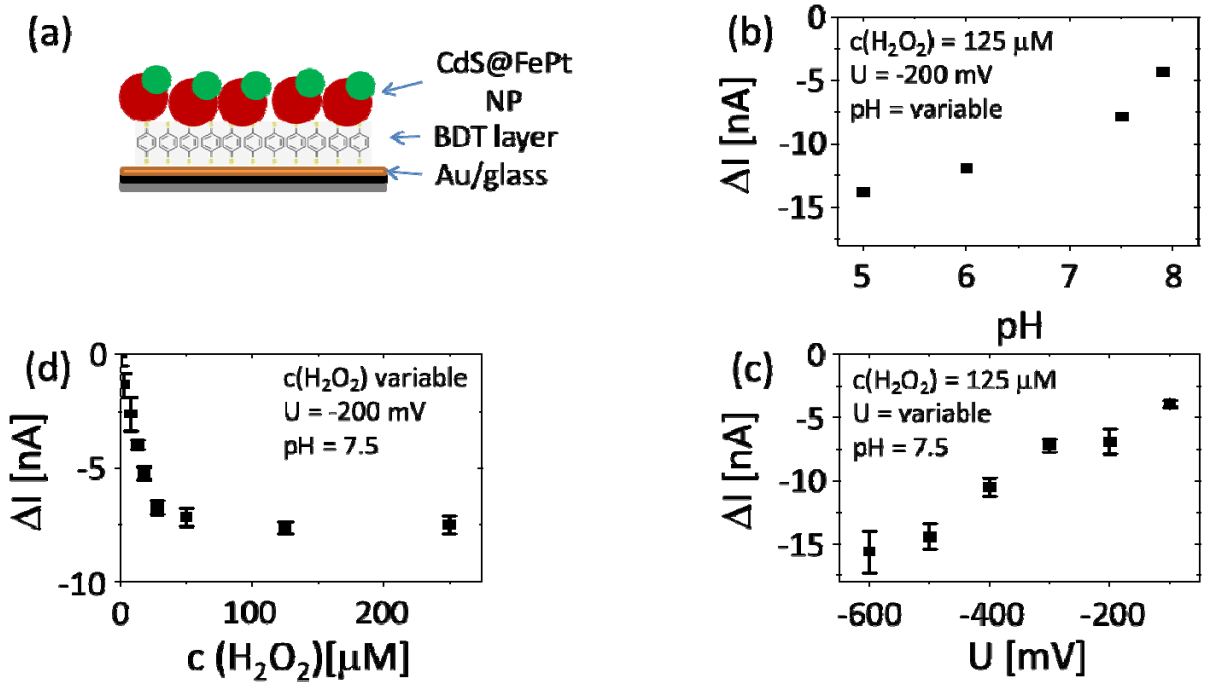

Figure S14: *(a) Geometry of CdS@FePt immobilized on Au/glass. Effects upon changing the bias potential U, pH, and H_2O_2 concentration are displayed.*

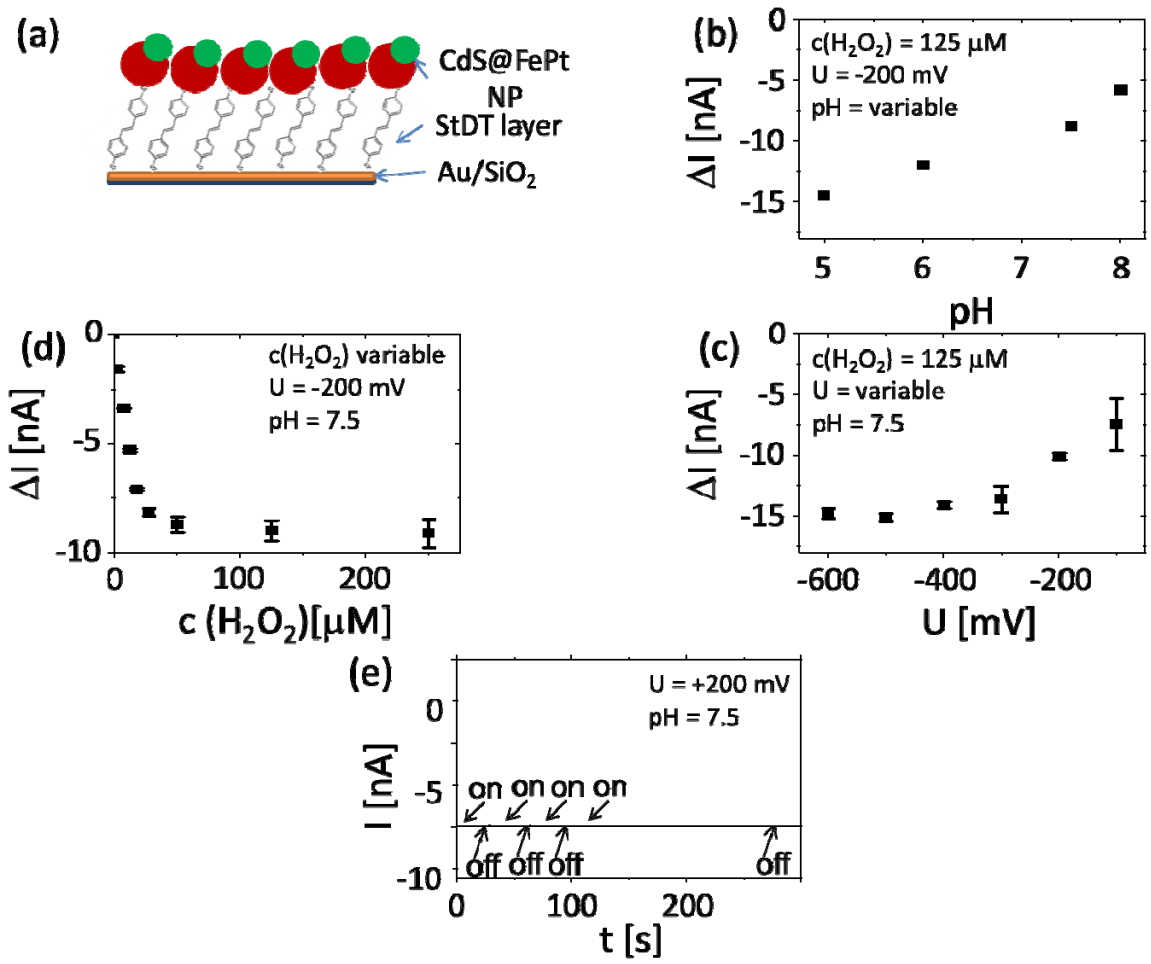

***Figure S15**: Geometry of CdS@FePt immobilized on Au/SiO_2. (b-d) Effects upon changing the bias potential U, pH, and H_2O_2 concentration are displayed. (e) Electrodes with StDT immobilized on Au/SiO2(without NPs) yielded no photocurrent.*

References

1. Zanella, M.; Abbasi, A. Z.; Schaper, A. K.; Parak, W. J. Discontinuous Growth of II-VI Semiconductor Nanocrystals from Different Materials. *Journal Of Physical Chemistry C* **2010**, *114*, 6205-6215.
2. Yu, W. W.; Qu, L.; Guo, W.; Peng, X. Experimental Determination of the Extinction Coefficient of CdTe, CdSe, and CdS Nanocrystals. *Chemistry of Materials* **2003**, *15*, 2854-2860.
3. Sun, S.; Murray, C. B.; Weller, D.; Folks, L.; Moser, A. Monodisperse FePt Nanoparticles and Ferromagnetic FePt Nanocrystal Superlattices. *Science* **2000**, *287*, 1989-1992.
4. Lehmann, A. D.; Parak, W. J.; Zhang, F.; Ali, Z.; Röcker, C.; Nienhaus, G. U.; Gehr, P.; Rothen-Rutishauser, B. Fluorescent-Magnetic Hybrid Nanoparticles Induce a Dose-Dependent Increase in Proinflammatory Response in Lung Cells in vitro Correlated with Intracellular Localization. *SMALL* **2010**, *6*, 753-762.
5. Zanella, M.; Falqui, A.; Kudera, S.; Manna, L.; Casula, M. F.; Parak, W. J. Growth of colloidal nanoparticles of group II-VI and IV-VI semiconductors on top of magnetic iron-platinum nanocrystals. *Journal of Materials Chemistry* **2008**, *18*, 4311-4317.
6. Gu, H.; Zheng, R.; Zhang, X. X.; Xu, B. Facile One-Pot Synthesis of Bifunctional Heterodimers of Nanoparticles: A Conjugate of Quantum Dot and Magnetic Nanoparticles. *Journal of the American Chemical Society* **2004**, *126*, 5664-5665.
7. de Boer, B.; Meng, H.; Perepichka, D.; Zheng, J.; Frank, M.; Chabal, Y.; Bao, Z. Synthesis and characterization of conjugated mono- and dithiol oligomers and characterization of their self-assembled monolayers. *Langmuir* **2003**, *19*, 4272-4284.
8. Stuhr-Hansen, N. The tert-butyl moiety - A base resistent thiol protecting group smoothly replaced by the labile acetyl moiety. *SYNTHETIC COMMUNICATIONS* **2003**, *33*, 641-646.
9. Niklewski, A.; Azzam, W.; Strunskus, T.; Fischer, R. A.; Woll, C. Fabrication of self-assembled monolayers exhibiting a thiol-terminated surface. *Langmuir* **2004**, *20*, 8620-8624.
10. Yue, Z.; Khalid, W.; Zanella, M.; Abbasi, A. Z.; Pfreundt, A.; Rivera_Gil, P.; Schubert, K.; Lisdat, F.; Parak, W. J. Evaluation of quantum dots applied as switchable layer in a light-controlled electrochemical sensor. *Analytical and Bioanalytical Chemistry* **2010**, *396*, 1095-1103.
11. Joo, S. W.; Han, S. W.; Kim, K. Adsorption of 1,4-benzenedithiol on gold and silver surfaces: Surface-enhanced Raman scattering study. *Journal Of Colloid And Interface Science* **2001**, *240*, 391-399.
12. Kafer, D.; Witte, G.; Cyganik, P.; Terfort, A.; Woll, C. A comprehensive study of self-assembled monolayers of anthracenethiol on gold: Solvent effects, structure, and stability. *Journal Of The American Chemical Society* **2006**, *128*, 1723-1732.
13. Gaines, G. L. The Ion-Exchange Properties Of Muscovite Mica. *Journal Of Physical Chemistry* **1957**, *61*, 1408-1413.
14. Gaines, G. L.; Rutkowski, C. P. The Extraction Of Aluminum And Silicon From Muscovite Mica By Aqueous Solutions. *Journal Of Physical Chemistry* **1957**, *61*, 1439-1441.
15. Newman, A. C. D. Cation Exchange Properties Of Micas.I. Relation Between Mica Composition And Potassium Exchange In Solutions Of Different Ph. *Journal Of Soil Science* **1969**, *20*, 357-&.
16. Tour, J. M.; Jones, L.; Pearson, D. L.; Lamba, J. J. S.; Burgin, T. P.; Whitesides, G. M.; Allara, D. L.; Parikh, A. N.; Atre, S. V. Self-Assembled Monolayers And Multilayers Of Conjugated Thiols, Alpha,Omega-Dithiols, And Thioacetyl-Containing Adsorbates -

Understanding Attachments Between Potential Molecular Wires And Gold Surfaces. *Journal Of The American Chemical Society* **1995**, *117*, 9529-9534.
17. Shaporenko, A.; Elbing, M.; Baszczyk, A.; von Hanisch, C.; Mayor, M.; Zharnikov, M. Self-assembled monolayers from biphenyldithiol derivatives: Optimization of the deprotection procedure and effect of the molecular conformation. *Journal Of Physical Chemistry B* **2006**, *110*, 4307-4317.
18. Rajalingam, K.; Strunskus, T.; Terfort, A.; Fischer, R. A.; Woll, C. Metallization of a thiol-terminated organic surface using chemical vapor deposition. *Langmuir* **2008**, *24*, 7986-7994.
19. Zhang, S.; Leem, G.; Lee, T. R. Monolayer-Protected Gold Nanoparticles Prepared Using Long-Chain Alkanethioacetates. *Langmuir* **2009**, *25*, 13855-13860.
20. Yang, Y. W.; Fan, L. J. High-Resolution XPS Study of Decanethiol on Au(111): Single Sulfur-Gold Bonding Interaction. *Langmuir* **2002**, *18*, 1157-1164.
21. Cyganik, P.; Buck, M.; Strunskus, T.; Shaporenko, A.; Wilton-Ely, J.; Zharnikov, M.; Woll, C. Competition as a design concept: Polymorphism in self-assembled monolayers of biphenyl-based thiols. *Journal Of The American Chemical Society* **2006**, *128*, 13868-13878.
22. Qi, Y. B.; Liu, X. S.; Hendriksen, B. L. M.; Navarro, V.; Park, J. Y.; Ratera, I.; Klopp, J. M.; Edder, C.; Himpsel, F. J.; Frechet, J. M. J.*, et al.* Influence of Molecular Ordering on Electrical and Friction Properties of omega-(trans-4-Stilbene)Alkylthiol Self-Assembled Monolayers on Au (111). *Langmuir* **2010**, *26*, 16522-16528.
23. Stöhr, J., *NEXAFS Spectroscopy*. First Edition ed.; Springer-Verlag, Berlin: 1992; p 407.
24. Reiss, S.; Krumm, H.; Niklewski, A.; Staemmler, V.; Woll, C. The adsorption of acenes on rutile TiO2(110): A multi-technique investigation. *Journal Of Chemical Physics* **2002**, *116*, 7704-7713.
25. Tang, J. L.; Wang, B. Q.; Wu, Z. Y.; Han, X. J.; Dong, S. J.; Wang, E. K. Lipid membrane immobilized horseradish peroxidase biosensor for amperometric determination of hydrogen peroxide. *Biosensors & Bioelectronics* **2003**, *18*, 867-872.
26. Davis, G. Electrochemical Techniques For The Development Of Amperometric Biosensors. *Biosensors* **1985**, *1*, 161-178.